Modeling of frictional forces during bare-finger interactions with solid surfaces

A Doctoral Dissertation Submitted to the Faculty

of

Drexel University

by

Marco A. Janko

in partial fulfillment of the

requirements for the degree

of

Doctor of Philosophy

September 2017

Dedications

Para mi abuelo Roman Janko, quien me enseñó con su historia de vida los valores del esfuerzo, la perseverancia, y la integridad.

Para mis padres Marcelo y Adelaida Janko por el sacrificio puesto en sacarme a mi y a mis hermanas adelante, además de su cariño y apoyo incondicional.

Para mis hermanas Monica y Carmiña Janko por su cariño constante y por haberme guiado en la vida desde niño.

Acknowledgments

This thesis was made possible because of the opportunity given to me by my advisors Moshe Kam and Yon Visell. Moshe opened the door of graduate school to me, and provided tireless guidance and encouragement from the first day of my PhD studies. Yon provided valuable advice which was fundamental for the confection and presentation of this research. All my gratitude and admiration goes to both of them.

The support, encouragement, and patience of my committee members, Leonid Hrebien, Matthew Stamm, Timothy Kurzweg, and Katherine Kuchenbecker, was also fundamental for the successful completion of this thesis.

The lessons learned through my PhD studies came not only from my advisors, but also from my colleagues and collaborators, Michael Wiertlewski, Richard Primerano, Jocelyn Monnoyer, Behnam Khojasteh, Yitian Shao, Zhengqiao Zhao who assisted me in diverse tasks, provided stimulating discussions, and taught me countless lessons.

My colleagues and friends in Uruguay who enabled the opportunity for me to start my graduate studies, Mario Fernandez, Guillermo Langwagen, Marcel Keschner, Roberto Anido, and Marta Castro, I will always be grateful for the help and support provided in my career.

The people at Drexel University were always supportive, willing to hear my questions, and offering their help countless times. Among these are the faculty Paul Kalata, Hisham Abdel-Aal, Teck Kah Lim, David Miller, Roger Marino, and Tom Chmielewski, as well as my colleagues from the Data Fusion and Re-Touch lab Raymond Canzaneze, Christopher Berry, Arjun Rajasekar, Donald Bucci, Scott Haney, Feiyu Xiong, Yifei Xu, Ji Wang, Jeffrey Wildman, Gabriel Ford, George Sworo, Sayandeep Acharya, Pramod Abichandani, Wade Kirkpatrick, Cole Gindhart, Xinwei Zhao, Nester Pereira, and Raghavendra Mudgalgundurao.

I am grateful to all my friends for sharing parts of this experience with me and encouraging me to go until the finish line. I am specially grateful to Jessica Snyder, Nicole Murphy, Lauren Klabonski,

Pratusha Reddy, Megan Hums, Pallavi Raj, Kristin Schwab, Chan Voong, Amrey Mathurin, David Tigreros, Manuel Figureoa, Jonathan Campos, Mohammad Nozari, Yohan Seepersad, Taz Kwok, Taif Choudhury and Nate McIntyre.

Table of Contents

List of Tables

List of Figures

List of Acronyms

CAD . . . . Computer Aided Design

CNS . . . . Central Nervous System

DOF . . . . Degrees Of Freedom

EDM . . . . Electrical Discharge Machining

EP . . . . Exploratory Procedure

FA . . . . Fast Adapting

FA-I . . . . Fast Adapting Type I

FA-II . . . . Fast Adapting Type II

FEM . . . . Finite Element Method

FRF . . . . Frequency Response Function

GOF . . . . Goodness Of Fit

GUI . . . . Graphical User Interface

HMI . . . . Human-Machine Interface

IEPE . . . . Integrated Electronics Piezo Electric

LED . . . . Light Emitting Diode

NLARX . . . . Non-Linear Auto Regressive Exogenous

NRMSE . . . . Normalized Root Mean Squared Error

RMS . . . . Root Mean Square

SA . . . . Slow Adapting

SA-I . . . . Slow Adapting Type I

SA-II . . . . Slow Adapting Type II

SMA . . . . Shape Memory Alloy

THD . . . . Total Harmonic Distortion

VPR . . . . Variance-to-Power Ratio

List of Symbols

$*$ . . . . The convolution operation

A_c . . . . Contact area between the fingertip and a surface

A_s . . . . Surface maximum height

C_p . . . . Pressure coefficient

D . . . . Empirical distribution of variable X

E_m . . . . Young's modulus

E . . . . Expected value

F_1 . . . . Force applied on piezo-electric transducer 1

F_2 . . . . Force applied on piezo-electric transducer 2

F_E . . . . Envelope of $\tilde{F}_T$

F_N . . . . Fingertip normal force

F_T . . . . Fingertip tangential force

F_m . . . . Measured force

F_r . . . . Rendered force

F_{adh} . . . . Adhesion force

F_{bN} . . . . Ball bearing model normal force

F_{bT} . . . . Ball bearing model tangential force

F_{def} . . . . Deformation force

F_{tot} . . . . Total friction force

G_{LPF} . . . . Zero-phase low-pass filter transfer function

H . . . . Empirical entropy of variable X

K_c . . . . Normal force to contact area (A_c) proportionality constant

K_i . . . . Spring constant (stiffness) of the ith element

L_i . . . . Length of the ith contact contour

$P_{\max}$ . . . . Maximum pressure

P . . . . Contact pressure

R^2 . . . . Coefficient of determination

R_f . . . . Radius of curvature of the fingertip

R_s . . . . Contact surface radius

S_s	. . . .	Shear strength
W_s	. . . .	Surface middle feature width
$^\circ$	. . . .	Degrees
α	. . . .	Surface slope angle
β	. . . .	Viscoelastic loss fraction
δ_s	. . . .	Spatial sampling interval
δ	. . . .	Length of skin indentation
ϵ	. . . .	Normalized root mean squared error
η_i	. . . .	i^{th} translation coefficient
γ	. . . .	Exponential factor between normal force and contact area
$\hat{F}_T$	. . . .	Fingertip tangential force estimate
λ	. . . .	Periodic surface spatial wavelength
$\mathbf{r}$	. . . .	Vector of regressors
$\mathcal{C}_i$	. . . .	i^{th} contact contour
$\mathcal{F}_T$	. . . .	Piece-wise linearly interpolated approximation of F_T
$\mathcal{R}$	. . . .	Region of contact between fingertip and surface
$\mathcal{X}$	. . . .	Piece-wise linear interpolated approximation of x
μ	. . . .	Friction coefficient
μN	. . . .	10^{-6} newtons (micronewton)
μm	. . . .	10^{-6} meters (micrometer)
μs	. . . .	10^{-6} seconds (microseconds)
ν	. . . .	Poisson's ratio
ω_i	. . . .	i^{th} wavelet coefficient
$\overline{F}_T$	. . . .	Mean fingertip tangential force pattern in spatial domain
$\overline{H}$	. . . .	Total empirical entropy X
π	. . . .	3.14159265359
ψ_i	. . . .	i^{th} dilation coefficient
ρ	. . . .	Pearson's correlation coefficient
σ_p	. . . .	Normal stress applied on a surface
σ_r	. . . .	Tangential stress applied on a surface
τ	. . . .	Signal delay
mm/s	. . . .	Millimeters per second
mm	. . . .	10^{-3} meters (millimeter)

$\tilde{F}_T$ . . . . Modulated fingertip tangential force in spatial domain

b_i . . . . Damping coefficient (viscosity) of the ith element

dA . . . . Infinitesimal contact area

f_p . . . . Prescribed normal force

$h'(x)$ . . . . Surface height slope

$h(x)$ . . . . Surface height profile

$h_{\text{sat}}(x)$ . . . . Saturated surface height

h_{thr} . . . . Surface height threshold

p_f . . . . Absolute position of the finger

r . . . . Distance between the finger center and a pressure point

v_p . . . . Prescribed sliding speed

v . . . . Fingertip speed

x . . . . X-axis coordinate of fingertip position

HC_0 . . . . Fundamental harmonic component

θ_M . . . . Vector of model parameters

θ_T . . . . Vector of texture parameters

$\overline{C}$ . . . . Normalized correlation

1D . . . . One dimensional

2D . . . . Two dimensional

3D . . . . Three dimensional

dB . . . . Decibel

DC . . . . Mean value of a waveform (direct current)

Hz . . . . $\sec^{-1}$ (hertz)

kHz . . . . 10^3 hertz (kilohertz)

kPa . . . . 10^3 pascals (kilopascal)

mN . . . . 10^{-3} newtons (millinewton)

ms . . . . 10^{-3} seconds (milliseconds)

N . . . . Newton

sec . . . . Seconds

W . . . . Watt

Abstract

Modeling of frictional forces during bare-finger interactions with solid surfaces

Marco A. Janko

Yon Visell, PhD

Touching an object with our fingers yields frictional forces that allow us to perceive and explore its texture, shape, and other features, facilitating grasping and manipulation. While the relevance of dynamic frictional forces to sensory and motor function in the hand is well established, the way that they reflect the shape, features, and composition of touched objects is poorly understood.

Haptic displays – electronic interfaces for stimulating the sense of touch – often aim to elicit the perceptual experience of touching real surfaces by delivering forces to the fingers that mimic those felt when touching real surfaces. However, the design and applications of such displays have been limited by the lack of knowledge about what forces are felt during real touch interactions. This represents a major gap in current knowledge about tactile function and haptic engineering. This dissertation addresses some aspects that would assist in their understanding.

The goal of this research was to measure, characterize, and model frictional forces produced by a bare finger sliding over surfaces of multiple shapes. The major contributions of this work are (1) the design and development of a sensing system for capturing fingertip motion and forces during tactile exploration of real surfaces; (2) measurement and characterization of contact forces and the deformation of finger tissues during sliding over relief surfaces; (3) the development of a low order model of frictional force production based on surface specifications; (4) the analysis and modeling of contact geometry, interfacial mechanics, and their effects in frictional force production during tactile exploration of relief surfaces.

This research aims to guide the design of algorithms for the haptic rendering of surface textures and shape. Such algorithms can be used to enhance human-machine interfaces, such as touch-screen displays, by (1) enabling users to feel surface characteristics also presented visually; (2) facilitating interaction with these devices; and (3) reducing the need for visual input to interact with them.

Chapter 1: Introduction

Haptics is the study of the sense of touch, and the interfaces that create and present tactile stimuli to the human body. It comprises topics such as object manipulation, and perception of object surface attributes through fingertip touch. This thesis is framed around understanding fingertip touch perception of surface attributes.

Touch is necessary for dexterous manipulation. Most notably, the frictional forces generated during fingertip touch provide sensory information necessary to regulate grip and account for the effects of loading. Touch sensing also allows us to discriminate the properties of touched surfaces, such as shape, texture and temperature among others during tactile exploration.

Recent studies [2, 3] have shown that reproducing the frictional forces felt by the skin is sufficient to facilitate the perceptual identification of surface textures. Haptic display technologies that elicit realistic touch sensations make use of this quality and modulate the frictional forces that correspond to physical non-flat surfaces in order to emulate textures artificially. This type of technology requires either recording frictional forces from real interactions, or predicting the frictional forces as they would be produced from the surface geometrical specification. The understanding of how frictional forces are affected by the geometry of the touched surface has been a long-term challenge in haptic technology development and is also of great interest for the development of tactile interfaces that emulate texture artificially.

Despite advances in haptic texture perception and the mechanics of touch, our understanding of how texture perception is facilitated by forces felt during tactile exploration is incomplete. Even less is known about how the forces that are felt by the skin during tactile exploration of an object or surface reflect perceptually meaningful attributes of the surface (such as its topography or material properties). Moreover, there are no comprehensive models that account for frictional force generation from attributes of a surface and characteristics of the fingertip. This dissertation aims to address some of these gaps.

1.1 Scope

The purpose of this dissertation is to characterize frictional force generation during bare-finger sliding touch on solid textured surfaces. It aims to explain how those forces vary according to texture or other surface features, and to characterize their role in the interfacial and bulk mechanics of contact with the skin.

To fulfill these objectives, we designed and developed a sensing system that captures forces and motion of a bare finger sliding over solid textured surfaces. We measured and studied frictional forces elicited during these interactions and identified the finger-surface interface features that affect and dominate the patterns of the frictional forces.

The main contributions of this dissertation are the description and modeling of these frictional forces in terms of the geometry of the surface of the object, and the sliding speed and normal force applied by the finger.

The models presented here have potential applications for enhancing human-machine interfaces (HMI) such as touch-screen displays. Synthesizing computer-generated tactile stimuli will allow emulation of textured surfaces using haptic displays, which in turn will enhance human interaction with electronic devices and, in some cases, will reduce the need for visual input to interact with them. Examples of HMIs that could benefit from this enhancement include touch-screen mobile phones and tablet computers, consumer electronics, entertainment platforms and medical diagnostic devices.

1.2 Overview

This dissertation is organized in seven chapters, of which Chapter 1 is this introduction.

Chapter 2 provides a survey of prior research on haptics, haptic perception, electronic haptic displays, haptic rendering, and the mechanics of the skin and of touch contact. Basic properties related to the sense of touch are summarized. Established models of haptic perception of surface texture are reviewed. Proposed models of the fingertip tissue and its behavior under both static and dynamic stimuli are introduced. This chapter closes with a review of haptic rendering strategies and

commonly used technologies.

Chapter 3 describes the development of a new sensing system composed of two main parts: 1) a high bandwidth, high resolution force-sensing device that was developed specifically for use in the experiments presented here; and 2) an optical fingertip tracking system. A brief comparison between design alternatives is provided in order to establish guidelines for the design of such devices.

Chapter 4 investigates frictional forces elicited during fingertip sliding interaction on textured surfaces of different scales, using two different normal forces and two different sliding speeds. Methods for improving spatial alignment between successive measurements and mitigating normal force modulation are presented and validated. The effects of the scale of the surfaces touched on the measured frictional forces are analyzed in detail. In addition, an attempt is presented to account for frictional force production exclusively from surface geometric specification. This effort used non-linear auto regressive exogenous models. The method was insufficient to capture the dynamics of frictional force production, which suggested the need to include more of the physical characteristics of the fingertip in the model in order to account for observed frictional forces.

Chapter 5 introduces a predictive modeling approach that captures discontinuous finger-surface contacts and models differential contact pressure with the finger. Comparisons with measured data show that this model can account for frictional force production of fingertips from different subjects sliding over undulating surfaces under different contact conditions.

Chapter 6 presents a biomechanically inspired model for the production of forces during tactile exploration of surfaces containing isolated features in the form of bumps and edges. This model captures finger-surface contact orientation, contact extent, and local interaction forces.

The model was validated using measurements of fingertip frictional forces and contact imaging as the finger slid over bumps and edges. The developed model was able to capture the most noticeable attributes of the frictional force measurements. Analysis of the measurements showed disconnections between the finger and the surfaces at highly concave regions of the surface. We named the regions

of disconnection "tactile blind zones", since they neither contact the skin nor stimulate the tactile sense.

The conclusions, a review of the contributions of this dissertation, and future research directions are discussed in Chapter 7.

1.3   Summary of Contributions

This dissertation addresses the modeling of contact interactions between the finger and touched objects during active touch sensing and interaction. The main contributions of this research are:

- The design and development of a new system for capturing motion and forces felt by a finger during tactile exploration of a textured surface, using custom force and optical sensors.

- Empirical measurement, characterization and analysis of complex spatial patterns of forces produced during sliding contact between a bare finger and undulating surfaces.

- A partial contact differential pressure model of sliding friction forces accounting for finger biomechanics and intermittent contact, based on four parameters, namely: skin disconnection threshold h_{thr}, contact surface radius R_s, fingertip radius curvature R_f and pressure localization r.

- Measurement and characterization of the role of contact geometry (synthesized as height slope), bulk and interfacial mechanics in jointly determining forces produced during tactile exploration of localized surface features.

- A quantification of the significance of "tactile blind zones", which are regions of touched surfaces never actually contacted by a finger.

Chapter 2: Background

The human body uses its five senses to interact with the physical world. Senses such as vision or audition have been investigated thoroughly, and the mechanisms underlying their functioning are relatively well understood [4, 5]. On the other hand, the senses of taste, smell and touch are less understood. The sense of touch is the only sense distributed through the entire human body, and its importance for the execution of daily activities is well acknowledged by numerous studies [6–9].

The word "touch" has many connotations, probably caused by the close relations between different sensing modalities whose sensory receptors are located on the skin. These sensing modalities include the sense of movement and position of limbs (proprioception), the sense of mechanical stimuli (mechanoreception) such as vibrations and pressure, also referred to as tactile sensing , the sense of pain (nociception), and the sense of temperature (thermoception). Touch refers to the combination of the four aforementioned sensing modalities for perception of our environment.

Among these four sensing modalities, perhaps the most used are mechanoreception and proprioception. For instance, it has been shown that precise object handling (dexterous manipulation) is not possible with limited mechanoreception [9], and skilled limb movement is nearly impossible without proprioception [7].

In this thesis the term "haptic touch" will be used to refer to active exploration of objects using a combination of proprioception and mechanoreception[1] in the hands. Hence, haptic touch refers to the set of actions and interactions necessary to explore objects to obtain information about their properties such as shape, texture, and stiffness, among others, using the hands.

Tactile texture[2] is an object's property that can be defined as the geometry of a touched object in the micrometer scale (micro-geometry) up to a few millimeters, that is, geometry in scales smaller than the size of a human fingertip. Based on the smallest texture detail (bump) that can be perceived (See Table 2.1) and the longest detail commonly considered as texture, in this document reference

---

[1]The combination of mechanoception and proprioception are also known as somesthesis [10]

[2]Tactile texture will be referred in the rest of this document simply as 'texture'

will be made to texture as geometry changes in the scale from 1 μm to 4 mm. Moreover, from a perceptual perspective, texture can also be defined as the resulting sensation elicited by an object's surface caused by the combination of sensed qualities of the object's surface, such as roughness, hardness, and stickiness, among others. The identification and interpretation of these qualities constitute texture perception.

Haptic engineering uses the knowledge about tactile perception and the limitations of it, in order to create systems that interact with the sense of touch. Thus, it involves the development of programmable devices capable of creating realistic haptic touch sensations in specified ways.

The rest of this chapter provides background on the basic physiology of touch, particularly the functions that are used for texture perception in haptic touch. It will also introduce the bio-mechanics involved during haptic touch, particularly sliding contact between a finger pad and a surface. Surface haptics technologies (haptic displays) and their working principles will be introduced, specifically those capable of rendering artificial textures from frictional force specification.

2.1 Physiology and perception

The sense of touch is a bi-directional, multi-modal sensory system. The bi-directionality implies that the sensing process is affected by the stimuli being sensed and vice-versa. Multi-modality implies stimuli used by the nervous system to discriminate different textures originate with signals (sensory cues) distributed both in the spatial and temporal domains [6].

The sensory receptors used for touch are distributed though the entire human body and located in the skin. Non-hairy skin (glabrous skin) is different from hairy skin, having a larger density of sensory receptors that are stimulated and activated by the sensory cues. Hence, glabrous skin has a finer spatial and temporal resolution to sense tactile stimuli [11–13]. This is likely to be the main reason why we usually use our hands, and more specifically our finger pads, to explore the physical properties of objects.

The perception of a physical object's properties during haptic touch starts with the activation of sensory receptors (mechanoreceptors [18]) by a mechanical stimulus above the mechanoreceptors' detection thresholds (supra-threshold stimuli). Once stimulated, the mechanoreceptors transform

Table 2.1: Afferent types and characteristics in glabrous skin [6, 14–17]

Afferent type	Mechanoreceptor	Receptive Field Size	Dynamic Response [a]
Slow Adapting Type I (SA-I)	Merkel	$2 - 3$ mm^2	< 5 Hz
Fast Adapting Type I (FA-I)	Meissner	$3 - 5$ mm^2	$5 - 50$ Hz
Slow Adapting Type II (SA-II)	Ruffini-like	~ 59 mm^2 [b]	$4 - 40$ Hz
Fast Adapting Type II (FA-II)	Pacinian	~ 101 mm^2 [c]	1000 Hz

[a]Approximate values based on studies using different stimuli
[b]SA-II react to skin strech over the entire hand [14]
[c]FA-II often react to distant stimuli
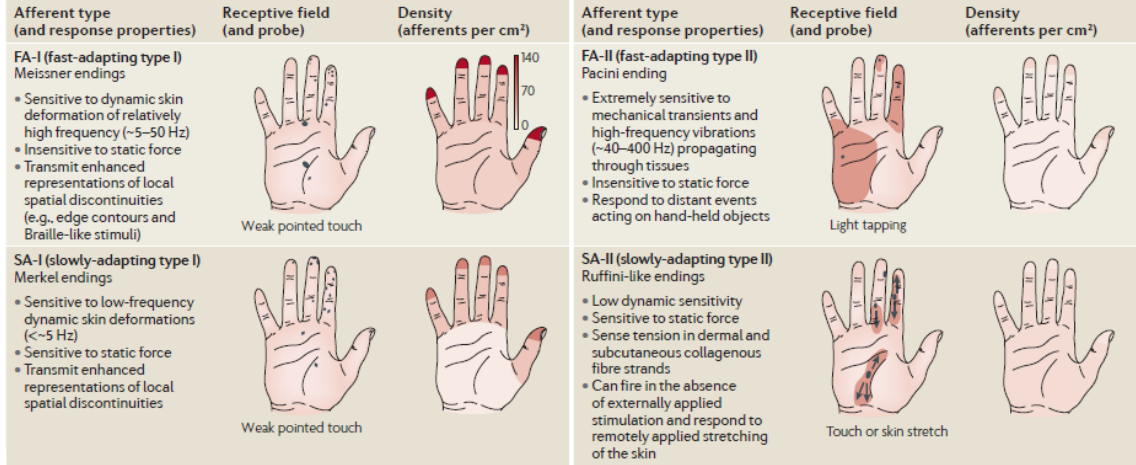
Figure 2.1: Illustration of the afferents present in the human finger pad. Adapted by permission from Macmillan Publishers Ltd: Nature Reviews Neuroscience (Johansson and Flanagan [6]), copyright (2009).

the stimulus to neural activity (sequence of action potentials [19], also referred to as spike trains). This neural activity then travels through specialized neurons (afferents) and reaches the central nervous system (CNS), where it is processed for haptic perception [6, 20]. Mechanoreceptors are present in high concentrations in glabrous skin of the hand, and particularly in the finger pads in humans [6, 15, 21] (Fig 2.1). Most of these mechanoreceptors respond to any mechanical stimulus, but their response is preferentially biased toward particular stimuli such as skin stretch, skin indentation, pressure and vibration, among others. These stimuli facilitate the perception of different object properties such as shape, texture, stiffness.

There are four main types of mechanoreceptors in the skin, each one paired with a corresponding afferent type (summarized in Table 2.1). Each of these is classified depending on the size of the physical area to which it responds (receptive field size) and its adaptation time. Afferents with

small receptive fields are classified as Type I, and those with large receptive fields are classified as Type II. Depending on how fast they adapt to a stimulus, afferents are classified as Fast Adapting (FA) or Slow Adapting (SA). The combination and spatial redundancy of the four types of afferents in the hand allow perception of different stimuli over the frequency band $0 - 1000$ Hz, with a static spatial resolution down to 0.5 mm [14]. Under dynamic loading conditions (variable skin indentation or sliding touch) the tactile resolution can be as fine as 1 μm [22].

Prolonged exposure to supra-threshold stimuli causes afferents to lose their sensitivity (a phenomenon commonly known as "adaptation") which can be expressed as either an increase of the excitation threshold or a reduction on the perceived intensity of supra-threshold stimuli [23, 24]. Changes in skin temperature has been shown to change the threshold of non-pacinian afferents [25]. For higher temperatures, the threshold is higher with an apparent upper bound reached at 40 $^\circ$ C.

Some aspects of texture perception such as range of perceived stimuli, perception thresholds, and sensitivity to stimuli duration for specific stimuli are widely understood, but how the spatial and temporal inputs from different afferents are related to perceptual interpretation by the CNS is still being investigated.

2.1.1 Spatial and temporal perceptual encoding

The characteristics of the four types of mechanoreceptors suggest that the encoding for texture perception involves the sensing of stimuli distributed both temporally and spatially. Hollins and Risner [26] found evidence for the existence of different mechanisms to encode roughness in the tactile system. They found that movement was necessary for subjects to perceive differences between smooth stimuli, but it was not necessary for differentiation of rough stimuli. It could be argued that if the perception of rough surfaces is possible under no relative movement between the fingertip and the object, then the spatial deformation patterns in the skin (strain and indentation) caused by the surface are enough to encode the texture of the surface. On the other hand, these spatial (static) cues seemed to be insufficient for the perception of soft surfaces, implying that if motion is necessary for perception in these cases, then the information necessary to code roughness should originate from cues in the temporal domain (vibration of the skin or other variables changing over time).

Hollins and Risner [26] also found that, in the absence of motion, differences between stimuli could only be perceived for surfaces with mean spatial period above 200 μm. This effect was not observed during discrimination involving movement. These observations led to the hypothesis that vibrations in the skin might convey the information for roughness perception of fine textures. Hollins et al. [27] investigated this hypothesis by using a wide range of periodic gratings with spatial periods above and below 200 μm (coarse and fine respectively), and asked subjects to discriminate fine or coarse stimuli under two conditions: 1) Exposing the finger pad of the subject to sustained vibrations at 100 Hz for 30 sec before the discrimination task (to selectively adapt mechanoreceptors) 2) No exposure to vibrations before the discrimination task. The results showed that adaptation prevented the subjects from discriminating between fine stimuli, but did not affect discrimination of coarse ones. Thus, the perception of fine texture seemed to be achieved through mechanisms sensitive to vibration in the skin.

It could also be argued that some types of mechanoreceptors may take a dominant role in the perception of either fine or coarse stimuli. Perceptual studies [28, 29] have confirmed that the Merkel corpuscles together with the SA-I afferents are mostly implicated in the perception of shape and roughness of coarse surfaces, while the Pacinian corpuscles together with FA-II afferents have been implicated in the perception of fine textures [27, 30]. Also, the Pacinian corpuscle's response has been characterized to be mostly of intensive nature, that is, the Pacinian corpuscles weigh the frequency content of the vibrations (amplitude of vibrations) selectively, assigning a higher weight to vibrations in the range 100 Hz to 300 Hz [30].

In summary, the duplex model of tactile texture perception states that fine textures are coded in temporal cues and coarse textures are mostly coded in spatial ones [31, 32]. Several studies [32] have provided evidence showing that discrimination between rough stimuli (spatial periodicity above 200 μm) is achieved through spatially distributed cues (without the necessity of skin vibration), mainly through activation of SA-I afferents, and fine stimuli (spatial periodicity below 200 μm) can only be discriminated when skin vibrations caused by lateral sliding motion occur; the Pacinian corpuscles and FA-II afferents (also referred to together as the Pacinian system) are mostly implicated in the

perception this type of stimuli.

2.1.2 Texture perception

The haptic perception of object attributes is achieved through the detection and processing of stimuli felt by the skin and body. Perceptually, texture is the attribute of an object that can be referred to as a combination of at least three descriptive qualities of an object during touch, namely roughness (rough/soft), hardness (hard/soft) and stickiness (sticky/slippery) [33, 34]. These qualities are not independent from one another, and their own perception might depend on common variables (temperature, moisture, applied pressure and sliding speed, among others). These qualities are better perceived through relative motion of the skin than through static contact [31, 35]. The most natural method to obtain information about an object's texture is through exploratory movements [36] (tangential sliding motion, pressure of the finger pads against a surface, or even static touch) which generate mechanical stimuli sensed by the mechanoreceptors in the skin [36, 37].

Roughness

Roughness refers to the surface topography of an object. It can be described as the difference in height, width and/or separation of topographical elements. Surfaces with few or smooth changes in their topography can be referred to as smooth, and surfaces with large variations on their topography can be referred to as rough. During direct touch, roughness perception is affected by the normal force applied by the finger pad against the object. Studies conducted by Lederman [38, 39] reported a shift in the subjective perception of roughness caused by differences in applied normal force. That is, objects feel rougher with increasing applied normal force. The sliding speed of the finger pad touching the object affected roughness perception slightly during active touch, but it had a larger impact for roughness perception during passive touch, making objects feel significantly rougher with increasing speed.

The characteristics of the surface also affect subjective roughness perception. It was reported [38–40] that perceived roughness increases with increasing distance between raised elements along the sliding direction of the surface (i.e., the longer the distance between elements, the rougher it

feels).

Moreover, increments in the raised element's width along the sliding direction seemed to decrease the perceived roughness, although this effect is of smaller scale[3]. The depth of the grooves did not seem to influence roughness perception, except in the cases where the finger pad may have touched the bottom of the gratings, in which case there was an apparent reduction of perceived roughness for gratings with larger spatial period [39]. Similar studies using different stimuli[4] also reported that the depth of the grooves did not affect roughness perception significantly [41, 42], and they further indicate that the spatial periodicity of the raised elements in the surfaces is also strongly correlated with the perceived roughness.

The effect of friction on roughness perception was discussed by Smith et al. [42], who used soap to reduce the coefficient of friction between the finger pad and the touched surface. A decrease in roughness perception with decreasing friction was evident, indicating that friction has a significant effect in the perception of roughness.

It is clear from the aforementioned studies that the key variables affecting roughness perception are derived from object attributes, such as surface geometry, which changes over space, and that roughness may also be affected by the applied force or sliding speed, which change over time. Nevertheless, the predominance of either spatially or temporally distributed cues is not evident from these studies.

These results provided insights on the dependence of perceived roughness on the geometry of the surface of objects, and how the former is affected by the exploratory movements and normal force that are applied.

Hardness

Hardness refers to the compliance or deformability of an object. If an object is easily deformable, it is referred to as soft and otherwise it is referred to as hard. Hollins et al. [34] found that hardness is a descriptive quality that, together with roughness, is sufficient to describe and discriminate between different textures. Subjective hardness perception could be explained by the patterns in

---

[3]These studies used square gratings with variable groove and land widths as well as variable land depths.
[4]These studies used arrays of raised square truncated cones, with varying distances between adjacent arrays.

contact area and temperature (in a lower scale) a subject feels while touching an object. A relation between hardness perception and cold temperature has been reported in a study in which subjects were asked to report the perceived hardness of objects at different temperatures; often cold objects felt harder than objects at room temperature or higher [43]. The effect of temperature is not a strong determinant of hardness perception, but it seems to introduce a bias when objects have low temperatures with respect to the finger pad's temperature.

The contact area between the fingertip and an object during touch has been directly related to softness perception [44, 45]. A finger pad touching a hard object will deform to accommodate the shape or texture of the object. In this case, the contact area between the finger pad and the object will increase slowly with increasing applied pressure on the object. Conversely, if an object is soft, the finger pad will tend to preserve its shape and the object's surface will change its shape; in this case, the contact area with the fingertip increases faster with increasing applied pressure. This observation allowed the artificial recreation of soft object sensations by Ben Porquis et al. [44], who provided evidence that contact area has a large effect on softness perception. Although normal applied pressure is not a variable directly related to the perceived hardness, it is directly related to the contact area [46].

Stickiness

Stickiness could be defined as the readiness of an object to adhere to other objects, and it is also a qualitative descriptor for texture, that has lesser impact than roughness and hardness for texture perception. This quality of objects is closely related with friction which, as discussed earlier, has an impact on roughness perception. The stickiness of a surface affects the contact conditions of the finger pad with the object, and increases the drag during sliding touch. Studies of the perception of texture in terms of stickiness or slipperiness have been more limited, but this quality was often referred to by subjects when asked to describe the texture of a variety of objects [34].

Together, these descriptive qualities (roughness, hardness and stickiness) are the most commonly used to describe the texture of an object. Nevertheless, the descriptive qualities used or acknowledged

by different people may vary depending on a variety of factors. In addition, according to the aforementioned studies, roughness plays a fundamental role in texture perception.

2.1.3 Active and passive touch

Klatzky and Lederman [1, 47] conducted a series of studies in which they observed the specific Exploratory Procedure (EP) used by subjects (e.g., sliding touch, static contact, contour following) when they were asked to make judgments about particular attributes of an object (e.g., hardness, shape, texture, weight). They found that different subjects tend to use the same EPs to perceive a given attribute. These exploratory procedures during unconstrained touch, although intuitive to humans, exhibit patterns in movement and force that are not easy to predict. The mechanical stimuli delivered to the skin are affected by the voluntary exploratory movements performed on the surface of objects, and these exploratory movements are in turn affected by the mechanical stimuli felt depending on the information sought in the surface [48–50]. This bi-directionality yields motion and forces that are highly unpredictable and by extension difficult to model analytically. Despite this variability and complexity in EPs, humans tend to be consistent about those used to extract a particular type of information about an object.

In a separate study, Lederman and Klatzky [1] ranked the EPs based on their usefulness (optimality, sufficiency) to provide information about seven different object attributes (Table 2.2). They concluded that while each EP could provide information about more than one attribute, they are not sufficient in themselves to provide information about all attributes assessed. Moreover, they claimed that it is not the sufficiency which determines the EP used to explore a given attribute; humans tend to use the optimal EP to identify a given attribute.

It could be inferred from the studies of Klatzky and Ledeman that, in order to extract information about the texture of an object, subjects preferred to use lateral motion (sliding touch) as an optimal EP, but they could also perceive texture using other EPs, such as applying normal pressure on the surface of the object or enclosing it with the hand. Interestingly, among these, there were two EPs that involved fingertip touch alone, normal pressure and sliding touch, which further emphasizes the

Table 2.2: Exploratory procedures. For each object attribute (from second to last column), each of the EPs in the leftmost column were assigned: 0 if subjects could not use the EP to get information about an attribute, 1 if subjects could use the EP to get information (sufficient) about an attribute, or 2 if the EP was optimal to get information about an attribute.[5]

	Texture	Hardness	Temperature	Weight	Volume	Global shape	Exact shape
Lateral motion	2	1	1	0	0	0	0
Pressure	1	2	1	0	0	0	0
Static contact	1	0	2	0	1	1	0
Unsupported holding	0	1	1	2	1	1	0
Enclosure	1	1	1	1	2	2	0
Contour following	1	1	1	1	1	1	3

important role fulfilled by the fingertip for touch.

Perhaps one of the most interesting results of studies conducted for haptic touch concerns the perceptual distinction between voluntary finger exploratory touch on a fixed surface (active touch) and moving surface pressed against the skin (passive touch). Schwartz et al. [35] and Lederman [38] reported no significant difference between active and passive touch for perception of roughness and shape during haptic touch. However, the importance of movement for accurate roughness and shape perception was demonstrated in studies that showed a degradation in roughness perception when subjects were asked to differentiate the roughness from different objects while the hand of the subject and the objects were in static contact [35, 36]. In spite of these results, a more recent study by Yoshioka et al. [50] showed a significant effect on texture perception caused by different sliding speeds during passive touch, i.e., subjects perceived increased roughness with increasing sliding speed while touching the same surface. During active touch this effect was not observed. On this basis, the authors asserted that active unconstrained touch is necessary for texture perception constancy, which refers to the situation in which a given stimulus is perceived the same under different exploratory conditions. While texture perception constancy is a natural and desirable characteristic of touch, it

[5]Reprinted from Acta psychologica, 84(1), Susan J. Lederman and Roberta L. Klatzky, Extracting object properties through haptic exploration, 29:40, Copyright (1993), with permission from Elsevier.

potentially means that mechanical stimuli being sensed is somehow optimally modified by free hand movements to achieve the perceptual constancy, making such stimuli challenging to model given the large number of free exploration parameters such as speed, pressure and orientation among others.

Perceptual studies conducted with controlled conditions, imposed to reduce the complexity of bare finger-surface interactions, (e.g., constant sliding speed, constant normal force applied) have provided interesting insights about the perceptual capabilities and limitations of haptic touch. It has been established that such perceptual capabilities are affected by factors intrinsic to the subject (such as the applied force on the object, scanning speed) [39, 42, 50] and they are also affected by factors intrinsic to the objects touched (geometry, temperature, moisture) [42, 51, 52].

2.1.4 Perception through tool-mediated interfaces

In contrast with direct touch of objects by a bare finger, several researchers have studied the perception of texture by subjects using a hand-held tool (indirect touch) sliding on a textured surface. It has been shown that texture discrimination is possible during indirect touch to an extent comparable to that of direct touch [53]. In this context, it is the geometry of the tool used to mediate touch, and not that of the finger pad, that defines and affects the stimuli and signals elicited during touch, which are used for perception of textures [54]. Some of the descriptive qualities used for texture perception during active touch, also play a role during indirect touch [55]. Nevertheless, since there is no direct contact between the skin and the object that is touched, the sensory system has no spatially distributed information reflecting the surface of the object explored, hence its texture is most likely perceived by cues in the temporal domain (skin vibration). Hollins and Bensmaia [32] reported that, during indirect touch, roughness perception is achieved by vibrotactile stimulation of the Pacinian system. Although, it is interesting to note that Hollins et al. [56] found that indirect touch on fine surfaces during extended periods can cause adaptation, and, as a result, the perceived roughness can be reduced, an effect also seen in a lesser scale during direct touch with fine textures, whereas the perception of rough textures was almost not affected by adaptation.

Perception has been compared for both direct and indirect touch by Yoshioka et al. [55]; the

main findings were that roughness, hardness and slipperiness can be used as descriptive qualities for an object's texture during indirect touch, and during direct touch. Nevertheless, it is worth noting that some qualities may be perceived completely differently during indirect touch and direct touch on the same object. For instance, it was reported that glass felt sticky for most subjects during direct touch, while it felt slippery during indirect touch. It is clear from these observations that the mechanical interactions may be very different, but the perceived phenomena still convey enough information for the sensory system to be able to discriminate among different textures.

Bensmaia and Hollins [57] showed that roughness perception during indirect touch is more closely associated with the amplitude of vibrations than with frequency, and they also reported that amplitude is weighted by the frequency response of the Pacinian system, which is implicated in vibrotactile perception.

Since there is a single solid contact point between the probe and the materials tested, the mechanics are easier to measure and model during indirect touch than during direct touch. This situation facilitates the study of the temporally distributed cues for describing the texture of an object.

Although the dependency of the qualities used to describe texture on physical phenomena and object geometry has been studied for indirect touch, to date, there is no comprehensive analytical model relating the geometry or texture of an object to the physical signals (frictional force, vibrations) elicited during indirect touch. Nevertheless, with the knowledge gathered about how texture perception is achieved during indirect touch (almost exclusively through vibrations in the skin activating the Pacinian system), it has been possible for experimenters to recreate realistic tactile sensations during indirect touch using a hand-held probe sliding on a flat surface [58, 59]. It seems clear from these studies that vibrations in the skin are necessary to convey realistic texture sensations during indirect touch.

2.2 Characteristics of fingertip touch interactions

Motion and force data measured from fingertip touch interactions vary widely even between two similar touch interactions [2, 60]. During these interactions, frictional forces have been found to be correlated with perceptual magnitude estimates of texture [2, 42]. Studies by Smith et al. [42],

have demonstrated that frictional forces are highly correlated with roughness estimates from different subjects, and the rate of change (derivative over time) of these frictional forces is also a good predictor for the perceived roughness. Wiertlewski et al. [2, 61] found that the interactive tangential forces seemed to play a determinant role for accurate texture recreation. They concluded that tangential force patterns have the potential to encode texture.

Recent efforts to describe the mechanics of frictional force patterns and their relation to the geometry of the touched object have led to models that can predict elicited forces under suitable conditions. For instance, Fujii et al. [62] predicted frictional forces, generated by bare finger touch on 'wavy surfaces' (sinusoidal gratings with spatial period larger than the finger pad), using lumped parameter models where the finger pad was modeled as a viscoelastic material and the contact conditions changed according to the surface geometry.

Robles-De-La-Torre and Hayward [3] demonstrated that perception of geometry of relief surfaces is not solely dependent on the vertical displacement elicited by the object's geometry, but in fact also depends strongly on frictional force cues. The experimenters designed an apparatus (mounted under the finger pad of subjects) that could record and playback the tangential force generated by bumps or holes while a subject slid the apparatus with the fingertip over these surface features. Using this apparatus, subjects were presented with physical holes and bumps using the apparatus recording the forces. Then, subjects were presented with flat surfaces and the apparatus generated the force elicited by either holes or bumps and subjects identified these sensations as being holes or bumps (virtual holes or bumps). Furthermore, using the same apparatus, a physical bump could be masked (felt as flat) or even overcome (felt like a hole) by reproducing the tangential force corresponding to a hole (raw or scaled by two, respectively) at the same time the subject's finger pad passed through the bump. Conversely holes could be masked or overcome using the tangential force corresponding to a bump. This study clearly showed that frictional forces (and related data such as movement speed) can be sufficient to elicit realistic geometric illusions, providing insights on the importance of geometry dependent forces for surface perception.

The contact conditions between the finger pad and an object's surface also greatly affect the

overall elicited frictional forces [37, 42]. For instance, Bicchi et al. [45] provided evidence that shows a dependency in contact area spread rate on the finger pad with the perceived softness of a material. It was clear from these studies that information about the position and movement of the hand (kinesthetic information) alone was not sufficient to convey a sensation of softness, as such sensations were significantly dependent on the contact area spread rate on the finger pad. A similar observation was made by Srinivasan and LaMotte [63], who reported that softness discrimination relies strongly on tactile information and not so much on kinesthetic information when touching compliant objects; in other words, the deformation of the object touched conveys sufficient information for softness discrimination.

2.2.1 Biomechanical properties of the fingertip

From a biomechanical standpoint, the finger pad is composed of many layers of tissue. A commonly accepted model [64–67] for the finger pad consists of four layers, modeling four main parts of the finger pad, namely skin (dermis and epidermis), subcutaneous tissue, bone and nail. Each layer may be modeled, mechanically, as a material with specified properties, such as Young's modulus (E) and Poisson ratio (ν) [68].

The bone and nail of the finger pad are usually assumed to be solid. Several studies [69–72] have indicated that the layers of subcutaneous tissue and skin behave as viscoelastic materials that can be modeled as soft materials with viscoelastic properties. A commonly accepted method of modeling the mechanical behavior of the finger pad is through lumped parameter models (mass-spring-damper models) that summarize the dynamics of the viscoelastic layers [69, 73]. Different lumped parameter models, involving combinations of ideal springs and dampers, allow mechanical characterization of viscoelastic materials. For instance Dinnar [74] used a Maxwell-Kelvin model to describe the behavior of the finger pad pressing down on a surface, and Nakazawa et al. [73] performed an analysis of the finger pad undergoing lateral (shear) traction using a Kelvin model. These models are used to study the responses of the finger pad under different conditions, such as external force (loading), free restitution (relaxation) and alternating continuous applied force (dynamic). The stiffness of the finger (modeled as spring constants K_i) and its viscosity (modeled

as damping coefficients b_i) determine the loading, relaxation and dynamic responses of a finger pad. Such responses are know to vary for different fingers and loading conditions (normal force applied, speed and direction) [73, 75, 76], hence the parameters of the models also change. The effects of temperature in the fingertip tissue mechanical behavior have not been thoroughly researched. Based on human soft tissue characterization studies [77, 78], it is reasonable to expect the stiffness of the fingertip to decrease with increasing temperature.

Pataky et al. [72] measured the response of the finger pad to increasing tangential displacement of a sand paper textured surface in contact with it. The results showed a linear (positive) relation between the steady state tangential force measured[6] and relative tangential displacements. Nevertheless, during unloading conditions (decreasing displacements) the tangential force decreased faster initially, showing a large hysteresis, and providing evidence of non-linear viscoelastic behavior.

Nakazawa et al. [73] applied a similar analysis to the contact dynamics of the finger pad against a flat surface under lateral traction. Their method increased the tangential force instead of the displacement of the flat surface. The results showed a transient effect of finger pad deformation with respect to position which then reaches steady state. Another experiment in this study used a linearly increasing tangential force (ramp force) with the normal force held constant. The results showed that the finger pad undergoes an elastic deformation for a range of tangential forces under which the surface remains steady, and there is a threshold tangential force at which the surface slides (steady slip). These studies by Pataky et al. [72] and Nakazawa et al. [73] measured the overall static stiffness of the finger pad, which showed a linear increase with increasing normal force. This can be attributed to the compression the finger pad. Both studies illustrate the complexity of the viscoelastic behavior of the finger pad.

Wiertlewski and Hayward [76] measured the dynamic response of finger pads to tangential forces. The main result was that the finger pad behaves elastically for frequencies below 100 Hz. For frequencies above 100 Hz, the finger pad's response was dominated by damping (see Fig 2.2). This

---

[6]Transient effects were observed after each displacement increment following an exponential trend. The steady value was obtained by fitting the observed signals to an exponential modeled signal.

[7]Reprinted from Journal of biomechanics, 45(11), Michael Wiertlewski and Vincent Hayward, Mechanical behavior of the fingertip in the range of frequencies and displacements relevant to touch, 1869:1874, Copyright (2012), with permission from Elsevier

---
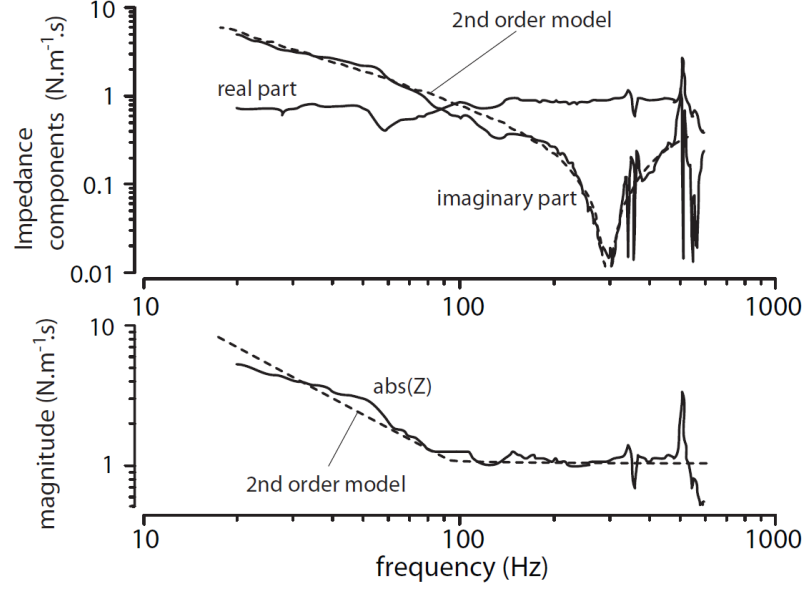
Figure 2.2: Dynamic response of the finger pad[7].

observation is consistent with the study performed by Cohen et al. [79] in which they observed a contact decoupling between the finger pad and a vibrating surface for frequencies above 100 Hz. These two observations together provide evidence of an apparent 100 Hz cut off frequency in the characteristic impedance of the finger pad under dynamic loading, providing further evidence of the viscoelastic behavior of the finger pad and how it changes for rapidly varying stimuli.

Contact area

The contact area between the finger pad and an object's surface varies depending on the relative hardness between the two (see Fig. 2.3). If the object is softer than the finger pad, the object deforms and acquires the shape of the finger pad. Conversely, if the object's surface is harder than the finger pad, the latter deforms in contact with the object. These latter situation is of greatest interest for this thesis. Interactions of this kind have been studied and are well defined for a variety of conditions.

The contact area A_c between the finger pad and a hard object's surface can be approximated by a disc. Xydas and Kao [80] reported that the radius of the contact area increases as a power
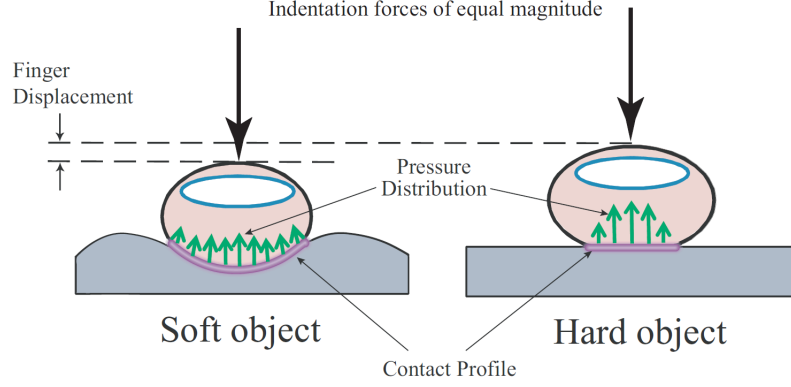
Figure 2.3: Illustration of a finger pad applying normal pressure on both a soft object and a hard object. Image reprinted from Ben Porquis et al. [44] **(copyright 2011 IEEE)**.

function of the normal force applied under static loading conditions. The relation was given by:

$$A_c = K_c \cdot F_N{}^\gamma \tag{2.1}$$

Where K_c is a proportionality constant, F_N is the normal force applied and γ is an exponent that can vary between 0 and 1/3. The lower bound ($\gamma = 0$) corresponds to an ideal soft finger, which reaches its maximum contact area upon contact with the surface, on the other hand, the upper bound ($\gamma = 1/3$) corresponds to the Hertz contact model [81] for a linear elastic material.

$$A_c = \frac{R_f}{E_{m\text{tot}}}(F_N)^{1/3} \tag{2.2}$$

$$\frac{1}{E_{m\text{tot}}} = \frac{1 - \nu_1{}^2}{E_{m1}} + \frac{1 - \nu_2{}^2}{E_{m2}} \tag{2.3}$$

In the Hertzian model of contact (Eq. 2.2), the proportionality constant K_c is determined by the radius R_f of the circular object (fingertip in this case) that contacts a flat surface and the total Young's modulus $E_{m\text{tot}}$ calculated from Eq. 2.3, where E_{m1}, E_{m2} represent the Young's modulus and ν_1, ν_2 the Poisson ratios of both materials. In the case of a finger pad contacting a flat surface, these parameters are difficult to measure or estimate and show a large variability between different
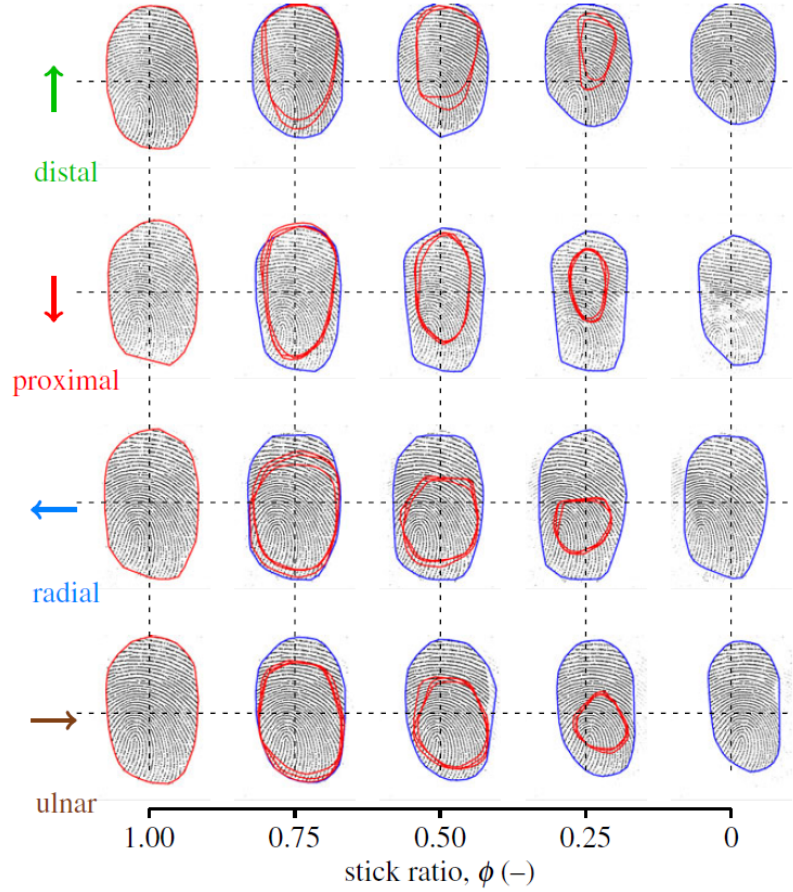
Figure 2.4: Example images of the evolution of the finger pad stuck area with background picture of the contact area. Blue contours surround the contact area, red contours represent the stuck area. Image adapted from "Dynamics of fingertip contact during the onset of tangential slip" by Delhaye et al., used under CC BY / Subfigure (a) from the original.

fingers. The study conducted by Xydas and Kao [80] suggests that the parameter K_c is higher for softer materials (they compared the values obtained experimentally for silicone and rubber). The same study also suggests the exponent γ depends on the finger pad's softness, yielding a lower γ for softer finger pads. Hence, both K_c and γ depend on the relative difference between the finger and the object.

The effects of the hardness of the object's surface on both pressure and contact area seem to be linked together; this situation can be explained by basic contact mechanics theory [46]. A finger pad applying pressure on an soft object tends to cause a deformation that will increase the contact area around the finger pad. Also the distribution of pressure at different locations under the finger pad

tends to not be uniform as a result of the object's deformation. Conversely a finger pad applying pressure on a hard object tends to flatten on the object and the contact area increases slowly with increasing pressure, so that the pressure distribution under the finger pad is more concentrated [44].

Xydas et al. [82] and Nakazawa et al. [73] showed that the contact area between a finger pad and a flat surface increases with increasing normal force, following a trend that reaches a maximum where increments in normal force do not cause a significant increments in contact area. The finger pad also shows interesting properties during lateral traction, Delhaye et al. [75] showed that there is a threshold tangential force for which the outer border of the contact area in the finger pad (slipping area) starts slipping while the innermost part remains "stuck" (stuck area) to the plate (see Fig. 2.4). Above the tangential force threshold, the stuck area reduces linearly with increasing force until it reaches zero, i.e., the whole finger pad contact area slides (steady state slip). Furthermore, the contact area was shown to decrease systematically during lateral traction. These studies help to explain the complexity of the transient of the onset motion and force patterns seen while measuring bare finger interactions with textured surfaces, although it is not clear whether these transient effects provide information used for the perception of texture.

2.2.2 Modeling of fingertip biomechanics

The research of in-vivo fingertip models [76, 83, 84] have provided insight about the physical characteristics of the human fingertip and its response under external loading conditions. High performance computing methods also allow the creation of numerical models and simulations [66, 67, 85–87], enabling the study of structures analogous to human fingertips that provide insight about fingertips undergoing external stimuli.

Analytic modeling

Several authors have proposed analytic models of fingertip biomechanics. A pioneering model based on modeling the fingertip as a thin membrane enclosing a fluid undergoing deformation was proposed by Srinivasan [83], which was later enhanced by accounting for the bending stiffness of the membrane undergoing deformation (which becomes a thin shell) [88]. These two models can predict skin

deflection of fingertips undergoing indentation. Lumped parameter models in the form of bulk stiffness and viscosity were also used successfully to describe the dynamics of a fingertip undergoing lateral loads by Nakazawa et al. [73]. Wiertlewski and Hayward [76] used a custom made apparatus to measure the mechanical impedance of different fingertips and found the behavior of the fingertips is mostly elastic for dynamic mechanical stimuli under 100 Hz and mostly viscous for stimuli above 100 Hz.

A more recent model developed for bare finger unconstrained touch was proposed by Fujii et al. [84], based on describing the resultant fingertip frictional force as the sum of two point contact elements sliding over a surface of size larger than the width of the fingertip. The results show this model is capable of capturing bulk frictional forces elicited by real human fingers sliding over coarse surfaces.

Numerical modeling

Finite Element Method (FEM) [89] is a numerical technique for solving differential equations. Hence, it is widely used to obtain numerical solutions for the response of physical systems (such as mechanical systems), modeled as an input-output relation using differential equations, to boundary conditions or loads (inputs). Thus, FEM consists in representing the problem as the interconnected union of non-overlapping components called finite elements that together represent the overall problem. Each finite element is used to approximate the output of the overall system to an input by calculating the response of each finite element, following the interconnections between adjacent elements and the loads, to compute the overall result. This technique is commonly used to simulate the behavior of mechanical systems under physical loads.

Finite element modeling was used to model the finger pad undergoing different types of loads such as downward contact pressure or sliding touch. Some of these models assume an homogeneous distribution of physical properties of the finger pad, whereas others propose a viscoelastic layered model. The latter seems to predict force patterns better in FEM simulations [69]. The production of vibrations during bare finger sliding touch was modeled by Wu et al. [66] using a layered model. The simulations provided insights into the propagation of vibrations in soft tissue, resulting in the

statement that high frequency vibrations are most likely to be concentrated on the skin and low frequency vibrations are prone to be located in deeper tissues. Also, the simulation results revealed resonances in the simulated fingertip at near 125 Hz and 250 Hz, although there was no direct evidence that these resonances occur in real fingertips.

Shao et al. [67] also used a layered model and, in addition modeled the fingerprints as equally separated ridges to study their effects on textured surface touch. They compared the response of two finger pad models, one with fingerprints and one without them. The simulation results showed that vibrations induced by sliding touch on surfaces with small roughness wavelengths (comparable to that of the fingerprints) were more prominent in the model with fingerprints, and interestingly they were located at regions on the finger pad where Meissner and Pacinian mechanoreceptors are located. Gerling et al. also used FEM to assess the effect of fingerprint ridges on object edge detection, in this study two dimensional (2D) models of a finger tip with and without fingerprints were compared under indentation by a double contact indenter. The stress patterns were compared, showing a stress amplification effect in the model with fingerprints. The authors claimed this could be one of the functions of the fingerprints, i.e., to aid discrimination of edges with the finger pads.

Wagner et al. [65] developed a three dimensional (3D) finite element model that could accurately mimic the response of the finger pad under indentation loading. They successfully validated the model, comparing the resulting surface deflections at different load displacements with previously published data [83, 85].

Finite element models have their limitations, since it is difficult to model the imperfections of a finger pad in detail. For example, the resonances in the simulations reported by Wu et al. [66] were not observed in experimental data collected (for example) by Wiertlewski and Hayward [76]. Possible causes for this discrepancy are the fact that the model used by Wu et al. [66] was a two dimensional model, the failure of the model to account for the fingerprint ridges, and the fact that the shape of the finger tip did not exhibit the imperfections of real fingertips. This provides evidence that simplistic models that assume that the finger pad's geometry and mechanical properties are homogeneous may lead to inaccurate predictions.

2.2.3   Frictional forces during active sliding touch

The magnitude of friction during sliding touch of textured surfaces is usually lower than that of grip forces during object grasping [37]. Friction has been implicated in the perception of roughness and slipperiness. For instance Smith et al. showed a correlation between subjective estimates of roughness and both friction and the rate of change in friction. Perception of slipperiness has also been correlated with frictional forces for sliding touch on different materials [90].

Different models have been used to quantify friction, the simplest being the Coulomb-Amonton model of dry friction between two objects, characterized by the friction coefficient (μ) describing the ratio between the tangential force and the normal force

$$\mu = \frac{F_T}{F_N} \tag{2.4}$$

The Coulomb model has been successfully used in studies modeling finger pad sliding touch, which indicates it is a good approximation for the modeling of frictional forces. The Coulomb model of friction makes the assumptions of dry and inelastic contact, which do not generally hold for sliding touch. A more detailed friction model was proposed by Adams et al. [91], including the effects of both skin moisture (adhesion) and skin deformation. In this model, the total friction force F_{tot} is calculated as

$$F_{tot} = F_{adh} + F_{def} \tag{2.5}$$

Where F_{adh} is calculated as

$$F_{adh} = S_s \cdot A_c \tag{2.6}$$

The parameter A_c is the contact area between the finger pad and the surface. The parameter S_s represents the shear strength of the interface. It could be calculated as a function of the mean

contact pressure P

$$S_s = S_{s0} + C_p \cdot P \tag{2.7}$$

The parameter C_p is known as the pressure coefficient, and S_{s0} is the intrinsic interfacial shear strength. Common values for C_p reported in the literature vary from 0.8 to 2, depending on skin hydration and the materials touched. Typical S_{s0} values range from 1 kPa to 6.1 kPa, and have been determined to increase with increasing skin hydration [92]. The skin temperature has also been shown to affect the coefficient of friction between the skin and a touched surface [93]. This might be due to the reduction of skin hydration with increasing temperature, which in turn affects the adhesion force.

The second term of the two-term friction model is meant to account for deformation of the finger pad due to the viscoelastic behavior of the skin. Considering that asperities on the surface of the object touched cause indentation in the skin of size δ in a surface contact area with radius R_s, and assuming that there is viscoelastic loss fraction β, the friction accounting for deformation is calculated as

$$F_{def} = \frac{3}{16} \beta \frac{\delta}{R_s} F_N \tag{2.8}$$

As shown by Nakazawa et al. [73], sliding motion of the finger pad may cause stick-slip behavior even on flat surfaces. A possible cause for stick-slip to take place is an object having texture or geometry that causes a spatial dependence of friction, it is also likely to happen during rubbing motion under high normal force applied.

2.3 Haptic rendering devices

Recent technological advances have yielded electronic devices that can recreate haptic sensations to a user with high fidelity [59, 94–97]. This process is commonly referred to as haptic rendering, while the devices engineered for haptic rendering are called haptic displays. A haptic display is a system capable of recreating the mechanical stimuli associated with an object or its surface (haptic
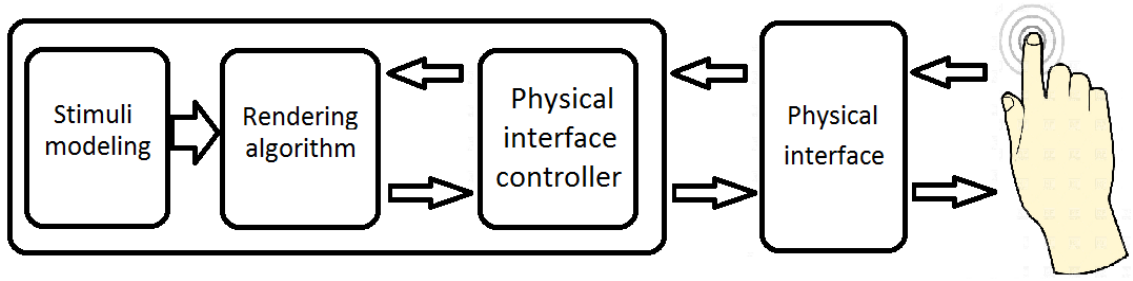
Figure 2.5: Generalized diagram of a haptic display

appearance) in a pre-determined manner. This type of system can be divided in four parts: 1) Stimuli modeling, which refers to the abstract numerical definition of an object or an object's surface for which the haptic stimuli is to be rendered. 2) Rendering algorithm, defines a procedure or strategy to present mechanical stimuli to emulate the 'haptic appearance' of the modeled object, depending on the motion and force of the user. 3) A controller in desgined to command the physical interface acording to the putput from rendering algorithm. 4) The physical interface, which comprises the hardware necessary to sense motion and force from the user that will enable the rendering algorithm to control the actuators to present with the proper mechanical stimuli (Fig. 2.5). The first three parts; stimuli modeling, rendering algorithm and physical interface controller are usually implemented by software in a computer or microcontroller.

There are diverse types of haptic rendering devices with functions targeting different parts of the body that capable of sensing the mechanical stimuli related to touch [98]. The type of haptic displays of greater interest for the present study consist of physical interfaces designed to interact with the hand, and more specifically the fingers, of a user. Some of the most used technologies of haptic displays in this category can be classified (based on the type of physical interface involved) as follows: tool mediated displays, force feedback displays, tactile displays, electrotactile displays, vibrotactile displays and variable friction displays (Table 2.3).

Tool mediated haptic displays

Tool mediated haptic displays usually consist of a hand-held stylus or handle that is used as an interface to provide force or vibrotactile stimuli to the hand while the tip of the tool slides on a flat

Table 2.3: Types of haptic display technologies

Display type	Display Principle	Remarks
Tool Mediated [99, 100]	Stimulation by mechanical vibration	Indirect touch
Force Feedback [3, 101]	Mechanical impedance simulation	Constrained touch
Tactile [102, 103]	Variable surface or shape	Direct touch
Electrotactile [104, 105]	Electrical stimulation	Invasive method
Vibrotactile [2, 59]	Stimulation by mechanical vibration	Direct touch
Variable friction [94, 106, 107]	Friction modulation	Direct touch

surface. The surface can be passive, or it can provide visual stimuli as well [58, 59]. Since there is no direct relationship between the contact areas between the hand and the tool with the surface texture of the object scanned, the perception of the object's surface texture in this case relies highly on vibrotactile stimuli delivered through the hand-held stylus. Interestingly, the Pacinian corpuscles in the hand are sensitive to the magnitude and relatively insensitive to the direction of these vibrations [108], allowing simplifications in the modeling of vibrations through hand-held tools. Culbertson et al. [99] showed that texture sensations can be reproduced using mathematical models of the relations between pre-measured position, speed, acceleration and force data at the tooltip.

Force feedback displays

Tool mediated force feedback displays use a contact interface (joystick, stylus, finger holder) providing force feedback while being manipulated by a subject. These devices are based on simulating the mechanical impedance (stiffness, viscosity and mass) of an object and exerting an opposite force to that of the user exerted on a virtual object depending on the virtual object's properties and the position of the users contact point (finger or hand) in space.

An example of this type of devices is the system "sandpaper" developed by Minsky [100], which is a 2 Degrees Of Freedom (DOF) force feedback haptic display. It uses a joystick as an interface to synthesize textures. This device was designed to recreate lateral forces depending on the position of the joystick. The gradient of the virtual object's height was also used to present forces that are associated with roughness. More sophisticated devices, like the phantom [95], are capable of rendering forces with 3 DOF, and can render forces with high resolution using a combination of three motors and rotational to translational converting mechanisms.

The forces simulated by force feedback displays are constrained by the maximum stiffness of the device and the maximum force rating, which limit the capacity of the feedback display to render virtual objects. Moreover, this type of device should (ideally) have little natural mechanical resistance, i.e., low mass (to emulate free space touch), should have high maximum force rating, frequency bandwidth to cover that of tactile mechanoreceptors, high position resolution and should be balanced to avoid undesired effects that could alter the perception of a simulated object [95].

Other force feedback displays, like the Falcon Omni [109] consist of a hand-held stylus that is constrained in motion by a force feedback device which makes it capable of rendering geometry of objects in a virtual environment.

Tactile displays

Tactile displays are devices that can transmit distributed small scale deformation to the skin via their surface, which provides tactile stimulation. Examples of this type of devices are matrices of variable height dots, as developed by Wagner et al. [102] or Moy et al. [103]. These type of mechanisms are realized using a complex design of mechanical, electronic or a combination of both. Common types of actuators, that allow independent control of each dot in the arrangement, include but are not limited to electrical, pneumatic, DC electrical motors, electrostatic, piezoelectric, Shape Memory Alloy (SMA), electro active polymers, electrorheologic.

Electrotactile displays

Electrotactile (or electrocutaneous) displays can be considered to be invasive devices. These devices pass an electrical current through the skin to stimulate the mechanoreceptors directly and elicit touch sensations. Devices that aim to use relatively high voltages and small currents to make the skin conduct, although the skin conductivity changes with variations in skin location, thickness and hydration, among other variables [105].

Subjects have described electrotactile stimuli as itch, vibration, pressure, tingle and in some cases pain. This type of stimulation could be entirely modulated over time or can be distributed in space (stimulating different mechanoreceptors) to elicit different touch illusions.
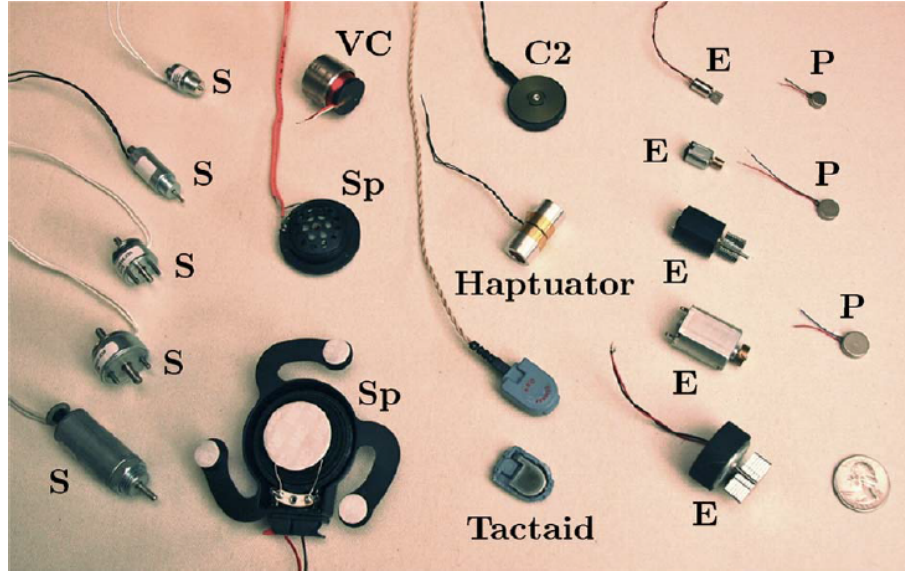
Figure 2.6: Sample actuators for vibrotactile display. S:Five solenoids of varying sizes. VC: A commercial voice coil without bearings. SP: Two audio speakers. C2: a C2 tactor from EAI. Haptuator: a Haptuator from Tactile Labs, Inc. Tactaid: One complete Tactaid form AEC and one opened to shod the suspension inside. E: Five shafted/cylindrical eccentric rotating mass motors. P: Three shaftless/pancake eccentric rotating mass motors. A U.S. quarter coin appears at the bottom right. Image reprinted from Choi and Kuchenbecker **(copyright 2013 IEEE)** [110].

These displays can stimulate mechanoreceptors directly which, in comparison with other displays, offer advantages such as delivering fast speed stimuli, high energy efficiency and easy miniaturization, among others. Nevertheless, given their invasive nature, these type of displays require special care during setup and the electrical stimuli delivered should be adapted to the electrical impedance of the skin under different conditions [104]

Vibrotactile displays

Vibrotactile displays consist of an arrangement of one or more vibrotactile actuators [110] (see Fig. 2.6) mounted on a rigid object, which is the interface with the user. These vibrotactile actuators elicit controlled vibrations of the entire interface that are usually in the frequency range detectable by fast adapting mechanoreceptors. Vibrotactile displays can take various shapes at the interface, for instance Wiertlewski et al. [2] developed a vibrotactile apparatus with a horizontal-flat interface. Other examples include tool mediated devices like the one used by Culbertson et al. [59].

Variable friction displays

Variable friction displays are intended for use during direct touch, they consist of flat (usually glass) plates that can artificially modulate the coefficient of friction between a fingertip and the plate using one of two methods: electro-vibration [97, 106, 111] or ultrasonic vibration [112, 113]. Electro-adhesion (also known as electro-vibration) uses a conductive polarizing plate that can induce an electrostatic force acting on the finger pad, increasing the friction between the plate and the finger pad (which creates a "drag effect"). On the other hand, ultrasonic vibration can reduce the coefficient of friction between the finger pad and the contact plate by making the later vibrate at ultrasonic frequencies (typically greater than 35 kHz). This effect produces slipperiness sensations that vary according to the frequency and amplitude of the ultrasonic vibrations. Possible explanations for this effect are: 1) Ultrasonic vibrations seem to create a thin layer of pressurized air between the contact plate and the finger pad which reduces drag caused by the fingertip contact with the plate [113] (squeeze film effect). 2) The ultrasonic vibrations make the finger pad to be in intermittent contact with the plate as a consequence of the plate vibrating at a small scale [114], this "bounce" effect can reduce the effective coefficient of friction.

Surface haptics

Surface haptics concerns the development of haptic devices via rigid flat surfaces that are capable of generating haptic sensations through variable friction, vibrotactile stimulation, electrotactile stimulation or a combination of these techniques. Thus, the term surface haptics is commonly applied to haptic touch screens and the methods used to program them in order to elicit haptic sensations.

Rendering algorithms

Haptic rendering algorithms have been extensively studied for tool mediated interactions with virtual objects. In them, the physical haptic interface is differentiated from the virtual environment as a virtual tool from which the output is, typically, the controlled force elicited by a change in position from the physical haptic interface [115].

A rendering algorithm can be divided in two main subcomponents: 1) A subcomponent in charge

of computing the virtual tool configuration from both the constraints of the environment and the physical haptic interface position. 2) A subcomponent in charge of computing the force elicited by changes in the virtual tool configuration. Together, these subcomponents are adapted to generate virtual interactions with a virtual environment through a tool (usually handle or stylus). The key aspects of virtual object interaction have to do with collision (between the virtual tool and a virtual object) detection and reaction, as well as the virtual object dynamics. This type of rendering algorithm allows the rendering of objects in environments with two, three or six degrees of freedom, which puts burdens on the processing units and the type of virtual interactions allowed. Most of the challenges faced using this type of rendering algorithm have to do with spatial resolution, update rate and stability of the system (affected by discretization). Nevertheless, this rendering scheme is capable of creating compelling illusions of interaction with solid objects.

One feature not (explicitly) included in the aforementioned rendering technique is friction. Haptic rendering techniques that do not render the frictional forces associated with the surface of the objects, elicit a sensation described by subjects as "icy slippery". In effect, for virtual objects to have a representation similar to their counterpart in the real world, they should include the attribute of friction that is present in most objects we usually interact with. Frictional forces have been closely related with texture of an object, therefore there has been recently a growing interest in recreating textures of objects using haptic rendering techniques.

Algorithms used to render textures depend on the type of interface used for rendering. The algorithm starts by the virtual definition of the stimuli to be delivered as a function of movement and force from the user. The algorithm then uses the measurements of variables including (but not limited to) position, speed and force to present appropriate stimuli (typically frictional force) to the user based on specified texture. For example, the sandpaper system developed by Minsky [100] used a position and height gradient dependent force field generation algorithm to recreate textures, whereas the phantom system developed by Massie and Salisbury [95] allows force feedback in a three dimensional space which allows it to present normal forces in addition to lateral forces, enabling the rendering of three dimensional objects.

Siira and Pai [116] proposed a stochastic approach to render textures synthetically. This method made use of Fourier series and/or white noise signals as force components to be added on smooth surfaces to create the sensation of texture. In the case of added white noise, subjects indicated the perceived roughness increased with increasing the standard deviation of the normal distribution used. Other methods, like the one applied by Fritz and Barner [117] extended this stochastic approach by decomposing the geometry of the object to be rendered using Fourier analysis, then representing the texture as a sum of Gaussian distributions (or other types of distributions). The main short come of the stochastic methods, is that they rely on pseudo random number generators to define a particular force at a given point in space. Nevertheless, given the nature of the random number generator, the force calculated at a given point is likely to not be the same for successive interactions resulting in lack of consistency of the forces generated over the surface.

Other rendering approaches, are based on measurement of physical variables. As described by Okamura, Kuchenbecker, and Mahvash [118], these methods are based on measurement of physical variables (such as contact position, normal force, sliding speed among others) during interaction with a textured surface. The measurements are used to perform rendering, typically recreating forces and vibrations elicited, using three main methods:

1) Create a database of signals to render directly (replay measured data). For instance, for every force signal measured in time domain $F_m(t)$ or space domain $F_m(x)$, the rendered forces ($F_r(t)$ or $F_r(x)$) are as follows:

$$F_r(t) = F_m(t) \tag{2.9}$$

$$F_r(x) = F_m(x) \tag{2.10}$$

2) Create input-output models that define pre-determined mappings of the signals to render depending on the interaction input(s) (position $x(t)$, velocity $v(t)$ or acceleration $a(t)$). In this case the rendered forces are computed as a function of the input forces, kinematic signals ($x(t)$, $v(t)$,

$a(t)$) and the model parameters θ_M estimated from the measured forces:

$$F_r(t) = f(t, x(t), v(t), a(t), \theta_M(F_m(t), F_m(x))) \tag{2.11}$$

$$F_r(x) = f(x, x(t), v(t), a(t), \theta_M(F_m(t), F_m(x))) \tag{2.12}$$

3) Create a physics based model that allow simulation of the physics involved for a given type of interaction. For instance, for a specified texture with parameters θ_T, the rendered forces are defined as:

$$F_r(t) = f(t, x(t), v(t), a(t), \theta_T) \tag{2.13}$$

$$F_r(x) = f(x, x(t), v(t), a(t), \theta_T) \tag{2.14}$$

An example of the first method is the procedure used by Wiertlewski et al. [2], in this case, the frictional forces as a function of position were stored and then rendered depending on the position of the user's finger pad. The second method was used, for example, by Culbertson et al. [99], in this case the measured force, acceleration, speed and position measured for a discrete set of magnitudes were used to create continuous mathematical models that allowed rendering of textures for unconstrained indirect touch. The third method is probably the least used for texture rendering, there have been approaches in which measured data was used to model the underlying forces from geometry, like Fujii et al. [62, 84]. Nevertheless, this approach is rarely used for the rendering of texture for active direct touch.

Chapter 3: Measurement apparatus

In order to investigate how frictional forces are generated during active sliding touch, a measurement apparatus was designed and constructed. This apparatus is capable of capturing both instantaneous frictional force and position of a fingertip sliding on textured surfaces with high dynamic range over a frequency bandwidth relevant to touch. Typical reported magnitudes of forces used for exploratory touch rarely exceed the order of 10 N (usually applied normal force) and they could be as small as 1 mN (usually frictional force) [37, 119–121]. Moreover, the force bandwidth relevant for haptic touch interactions is approximately 1-1000 Hz, although dynamic forces above 500 Hz are rarely reported and/or measured.

Based on these observations, the measurement apparatus was designed to fulfill three main requirements:

1. High measurement range (1 mN to 10 N)
2. High bandwidth (5 to 500 Hz)
3. Minimally or non invasive to the finger

Requirements 1 and 2 assure accurate measurement of forces in the range 1 mN to 10 N and artifact-free over a frequency bandwidth relevant to active dynamic touch. Requirement 3 ensures the finger interactions with the surface are not affected by the measurement apparatus.

3.1 Force measurement technologies for tactile sensing

The design of force measurement devices that allow measurement of interactive forces between interchangeable textured surfaces and a bare finger usually requires the design of a supporting structure (to hold textured surfaces) combined with force transducers that provide force measurements in electronic format.

Many researchers have used custom designed force measurement devices for tactile sensing allowing them to study the force dynamics of a bare finger sliding on surfaces of various characteristics.

Two of the most commonly used force transducers are 1) Strain gauge based and 2) Piezoelectric based.

Strain gauges have the advantage of allowing direct mounting on the supporting structure [60], while being comparatively inexpensive and allowing comparatively easy electrical interfacing with data acquisition devices. On the other hand, piezo-electric transducers provide higher measurement bandwidth than strain gauges, but require more sophisticated electronics to interface the sensing elements (piezo-electric) and the static force measurement component drifts over time, reducing the usable frequency band to frequencies above 0 Hz (usually > 2 Hz).

Examples of strain gauge based force sensing devices were either used or developed by Smith et al. [42], Fujii et al. [62, 84] who used commercially available strain gauge based force transducers mounted in a custom made tray to measure comparatively large scale forces (> 1 N) in their studies. We also designed a similar device in a preliminary study [60], such device had a usable bandwidth of 130 Hz (enhanced digitally after data collection).

Piezo-electric based force measurement devices were recently developed by Wiertlewski [122] whose device ensured a usable bandwidth from 20 to 500 Hz, with high sensitivity (50 μN). Another design by the same author [123], that was also further adapted and used by [124–126], ensured a bandwidth of at least 500 Hz with an unreported sensitivity, but very low baseline noise (< 1 mN).

3.2 Force measurement device

The apparatus designed for the present studies included a piezo-electric based custom-made new force measurement device, a fingertip tracking device (either an optical motion capture system or a high speed camera), data acquisition hardware, and a personal computer running data acquisition software and a custom-made graphical user interface Graphical User Interface (GUI) programmed in MATLAB that was used to monitor data collection and provide feedback during the experiments.

We designed and fabricated a custom force sensing instrument (Fig. 3.1) to precisely capture forces applied by a finger sliding on a textured surface. The sensor consisted of a rigid tray suspended on a compliant mechanism. Two pairs of flexure hinges provided constraints that limited the motion in all but the horizontal and vertical directions (Fig. 3.1 B & C). The device structure was
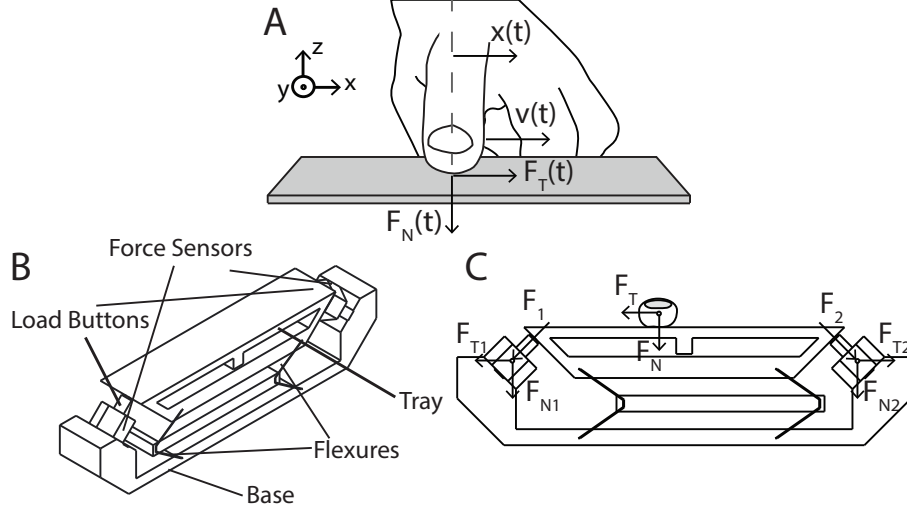
Figure 3.1: A Variables to be measured and estimated by the apparatus; fingertip position $x(t)$, scanning speed $v(t)$, and mechanical forces $F_N(t)$ and $F_T(t)$ exerted by the finger. **B** Isometric illustration of the force sensing device. **C** Front view of the force sensing device illustrating normal and tangential force decomposition during sliding contact with the finger.

designed using compliant mechanism theory [127], solid Computer Aided Design (CAD) modeling and simulated using Finite Element Method (FEM) numerical simulation (COMSOL Multiphysics, Boston, MA), ensuring a usable measurement bandwidth extending to 500 Hz, i.e structural resonant modes at frequencies above 500 Hz (Fig. 3.2). We fabricated the rigid sections of the device from type 6010 aluminum alloy using precise Electrical Discharge Machining (EDM), and constructed the flexures from 0.25 mm type 1095 spring steel. The top section of the tray (top dimensions 120×25 mm) was specified to support textured surfaces that were to be used in our experiments.

Electronic sensing was performed by a pair of piezoelectric force sensors (Model 9712A5, Kistler Instruments, Winterthur, Switzerland) terminating on hemispherical contact buttons, and positioned to contact the tray at $45\,^\circ$ angles (Fig. 3.1B), allowing normal and tangential force components to be measured. The sensors were powered using an Integrated Electronics Piezo Electric (IEPE) compliant supply (Model 5134, Kistler Instruments).

Due to the $45\,^\circ$ orientation, the force signals F_1 and F_2 measured by the sensors are linear combinations (with equal weights) of the force components normal and tangential to the surface F_N
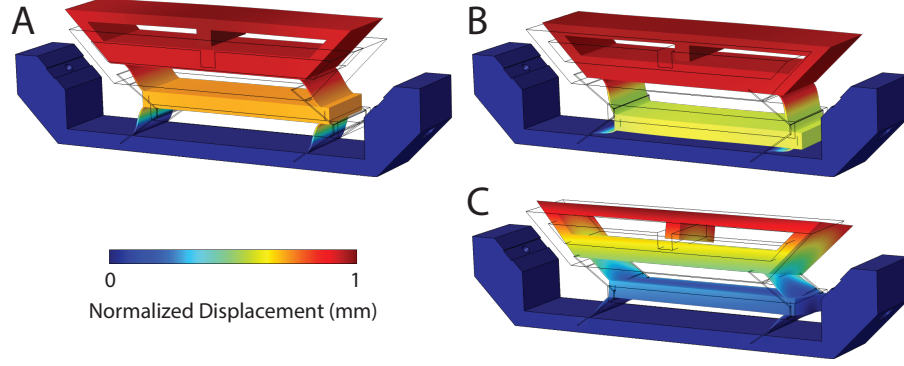
Figure 3.2: First three structural resonant modes of the force sensing instrument . **A** First resonant mode, frequency 679 Hz. **B** Second mode, frequency 902 Hz. **C** Third mode, frequency 1265 Hz.

and F_T respectively, of the resultant force applied to the tray (Fig. 3.1 C).

$$F_N = \frac{1}{\sqrt{2}}(F_1 + F_2), \quad F_T = \frac{1}{\sqrt{2}}(F_1 - F_2) \tag{3.1}$$

Once the device was assembled, an experimental Frequency Response Function (FRF) was measured using a pendulum to strike the tray horizontally (emulating an impulse force input) on a flat sample fabricated using the same material as the sinusoidal gratings. A total of 20 trials were measured and the frequency response was obtained by transforming the resulting force signals using the Fourier transform (Fig. 3.3). We calibrated the electronic sensor using a step force input of known magnitude, the electronic measurements required an amplification of 3.7 dB relative to the manufacturer's specifications. Moreover, to ensure repeatability of the force measurements, we compared the measurements provided by our force measurement device to those provided by a factory calibrated strain gauge based S-beam force transducer (Model LSB200, Futek Irvine, CA) mounted on top of the tray. A set of random forces applied on the tray with bandwidth within the S-beam bandwidth were used. The comparison between the measurements from both sensors verified the measurements of our force measurement device were accurate.

A picture of the assembled force measurement device can be seen in Figure 3.4.
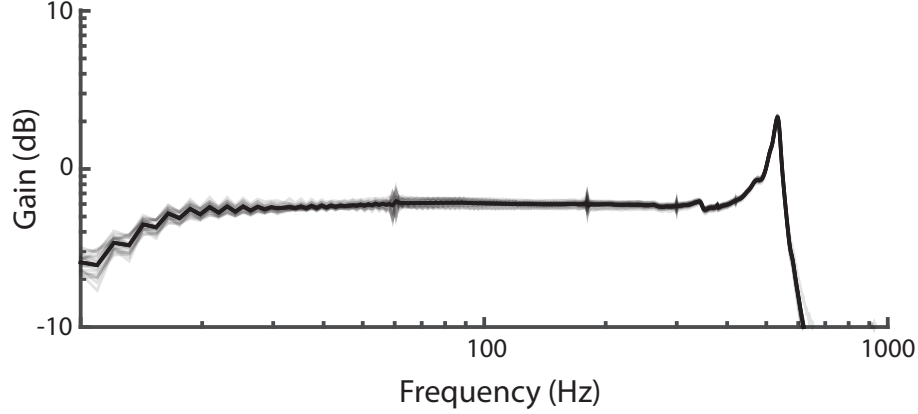
Figure 3.3: Frequency Response Function (FRF) of the force sensing apparatus in the tangential direction. Twenty individual trials in gray, average in black. The FRF shows a resonant mode above 500 Hz and low amplitude interference from the power supply at 60 Hz and its harmonics. The usable bandwidth is approximately from 15 - 500 Hz.

3.3 Fingertip tracking methods

The two main experiments presented in this thesis required two different methods for tracking subjects' fingertips undergoing sliding contact with different surfaces. The two methods used were A) Motion capture system and B) High speed camera. Both methods are described in detail hereafter.

3.3.1 Motion capture system

The instantaneous position of the fingertip was captured using an optical motion capture system (V120:Trio Natural Point, Corvallis, OR). This system tracked a small reflective marker that was adhered to the fingernail. The optical motion capture system operated with a sampling period of 8.3 ms and an approximate spatial resolution of 0.2 mm. It was positioned and calibrated to have the zero reference at the center of the apparatus along the x axis (Fig. 3.5).

Using this setup, the signals from two piezo eletric force sensors were conditioned and digitized (55.6 μs sample period, 16 bits) using data acquisition hardware (NI 9215 and Compact DAQ, National Instruments Inc., Austin, TX). Both force data acquisition and optical motion capture data were managed by a computer running a custom software Graphical User Interface (GUI) (MATLAB Release 2014b, The MathWorks, Inc., Natick, Massachusetts) that controlled the data recording process and kept both streams of data synchronized.
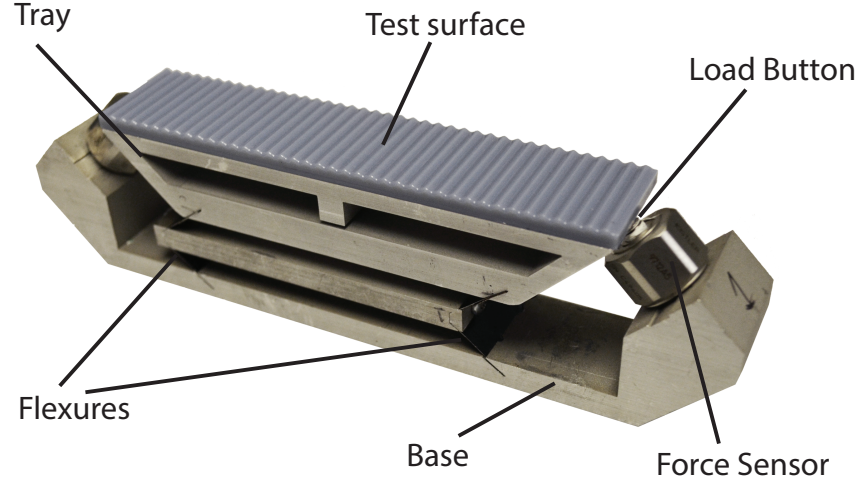
Figure 3.4: Fully assembled measurement apparatus picture. A sample surface (blue) is mounted on top of the tray.
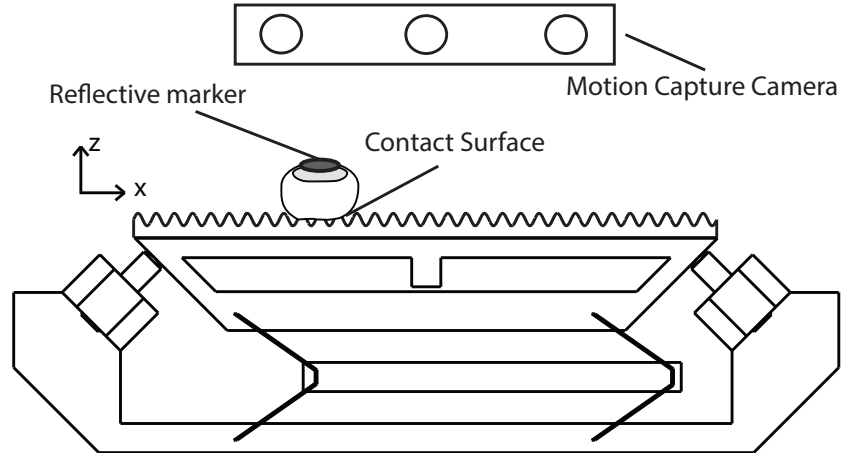
Figure 3.5: Illustration of apparatus setup using motion capture for fingertip tracking.

3.3.2 High speed camera

Frontal video of the finger was captured using a high-speed camera (Phantom Miro M110, Vision Research Inc., Wayne, NJ), with 1 ms sample period and resolution 1280x720 pixels. The camera view range centered at the center of the interaction region, the spatial resolution in our setup was approximately 0.02 mm. Illumination was provided by a 40 W light emitting diode (LED) light source (No 5 LED, HS Vision GmbH, Ettlingen, Germany) generating a light beam that covered the entire aperture of the lens of the camera, and yielding high-speed video that consisted of the
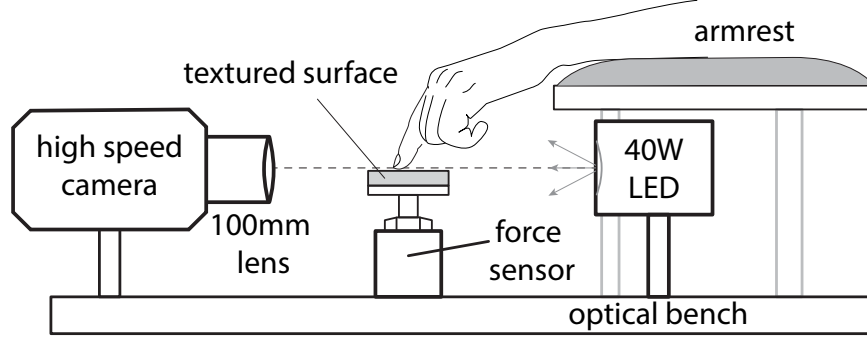
Figure 3.6: Illustration of apparatus setup using a high speed camera for fingertip tracking.

background (bright light), the contour of the surface profile (dark zone) and the shaded area caused by the fingertip obstructing the light. This configuration (Figure 3.6) made it possible to accurately track the fingertip contour and its evolution during the sliding contact while capturing the contour of the surfaces used in the experiments as well.

Using this setup, the signals from the piezo eletric force sensors were conditioned and digitized (100 μs sample period, 16 bits) using with data acquisition hardware (NI-6229, National Instruments Inc., Austin, TX). The force data acquisition was managed by a computer running a custom software GUI (MATLAB Release 2016a, The MathWorks, Inc., Natick, Massachusetts) and the high-speed camera control software (Phantom Camera Control Application). Both streams of data were recorded separately, but synchronization was maintained by sending a "record" trigger signal to the camera from the MATLAB GUI.

3.3.3   Comparison between finger tracking methods

Both methods used for finger tracking during the experiments have comparative advantages and drawbacks, the preference of use of one above the other depends on the parameters of the experiment to be performed such as the setup time available and variables to measure, which in turn determine the precision and bandwidth required.

We utilized a motion capture system for finger tracking in our experiments to collect data during time intensive intensive recording sessions involving human subjects. In this scenario, the setup time had to be minimized and the resultant data sets were anticipated to be large which resulted

in an upped bound on the data memory and storage could be used during a recording session and the posterior data analysis. In these experiments the low update rate was mitigated by linearly interpolating the measured data points under the assumption that the fingertip position does not change drastically in time scales of tens of μs.

In contrast, when the design of the experiment required capturing high detail images of the fingertip tissue and tracking of not only the fingertip position, but also the skin deformation pattern, we utilized a high-speed camera at the cost of reducing the size of the data set and increasing both time and complexity of data analysis.

The choice of finger tracking technology to be used is ultimately dependent on the parameters of the experiment and the materials available. As a guideline Table 3.1 provides a comparison between both technologies used in this dissertation.

Table 3.1: Comparison between finger tracking methods

Motion capture		High speed camera	
Advantages	Drawbacks	Advantages	Drawbacks
Fast deployment	8.3 ms update rate	1 ms update rate	Complex setup
Fast data processing	Requires marker	Allows contour tracking	Slow data processing
Low memory	Minimally invasive	100% Non-invasive	High memory
Low storage	0.2 mm spatial resolution	0.02 mm spatial resolution	High storage
Low cost			High cost

Chapter 4: Measurement and characterization of frictional force patterns during tactile exploration

The material in this chapter was adapted from the published manuscript: Marco Janko, Richard Primerano, Yon Visell, "On Frictional Forces Between the Finger and a Textured Surface During Active Touch" IEEE Transactions on Haptics. Volume: 9, Issue: 2, April-June 1 2016.

In this chapter we describe measurements of forces felt by a bare finger in sliding contact with a periodically textured surface, and how they depend on properties of the surface and contact interaction.

Prior research has shed light on haptic texture perception. Nevertheless, how texture-produced forces depend on the properties of a touched object or the way that it is touched is less clear. To address this, we used the apparatus described in chapter 3 (with motion capture for fingertip tracking) to accurately measure contact forces between a sliding finger and a textured surface. We fabricated periodically textured surfaces, and measured spatial variations in forces produced as subjects explored the surfaces with a bare finger. We analyzed variations in these force signals, and their dependence on object geometry and contact parameters. We observed a number of phenomena, including transient stick-slip behavior, nonlinearities, phase variations, and large force fluctuations, in the form of non-periodic signal components that proved difficult to model for fine surfaces. Moreover, metrics such as total harmonic distortion and normalized variance decreased as the spatial scale of the stimuli increased. The results of this study suggest that surface geometry and contact parameters are insufficient to account to determine force production during such interactions. Moreover, the results shed light on perceptual challenges solved by the haptic system during active touch sensing of surface texture.

We measured force and kinematic data as individuals explored periodically textured surfaces with their index fingers, at specified speeds and normal forces. In order to identify invariant properties of these interactions, we analyzed the force patterns in the spatial domain, and aligned them,

compensating for fine variations in contact position from trial to trial.

4.1 Textured surfaces

We fabricated textured surfaces with known geometries, which were specified through height functions $h(x)$, in order to study the variation of forces with surface geometry during sliding touch of these surfaces with the finger. These surfaces were sinusoidal surfaces with height profiles given by $h(x) = A_s \sin(2\pi x/\lambda)$. Amplitude A_s and spatial wavelength λ varied for each sample. Eight such surfaces were used in the experiment, with $\lambda = 0.5$ mm, 1 mm, 1.5 mm, 2 mm, 2.5 mm, 3 mm, 3.5 mm and 4 mm. The amplitude of each sinusoidal surface was equal to a fixed fraction of the wavelength for all samples, $A_s = 0.1\lambda$, ensuring that the maximum slope was constant for all sinusoidal surfaces – only the scale varied. All surfaces were 120 mm long and 25 mm wide (Fig. 4.1 B,C). The surfaces were modeled parametrically in software and fabricated using a photopolymer resin 3D printer (Objet 30, Stratasys Inc., Boston, USA) yielding an artifact-free finish at the scales of interest (approximate resolution: 100 μm). No further processing was performed to modify the surface finish. The surfaces were firmly affixed to the measurement apparatus with two-sided adhesive tape during the experiments.

4.2 Measurement procedure

The measurement apparatus was used to capture normal forces, tangential forces, and movement during sliding contact of a bare finger on a textured surface. Nine individuals participated in this experiment (5 male and 4 female, ages 19 to 28). None evidenced any abnormality of biomechanics or function of the finger or hand, and all were right hand dominant. Each participant was seated in front of the apparatus with the right elbow supported and forearm held at a comfortable angle. They each performed sliding touch of the eight different sinusoidal surfaces a total of 30 times in alternating directions, using the second digit of the right hand. There were four different measurement conditions (Table. 4.1), which varied in nominal scanning speed (80 mm/s and 120 mm/s) applied normal force (0.3 N and 1 N).

In order to enable participants to produce normal forces and sliding speeds close to those that
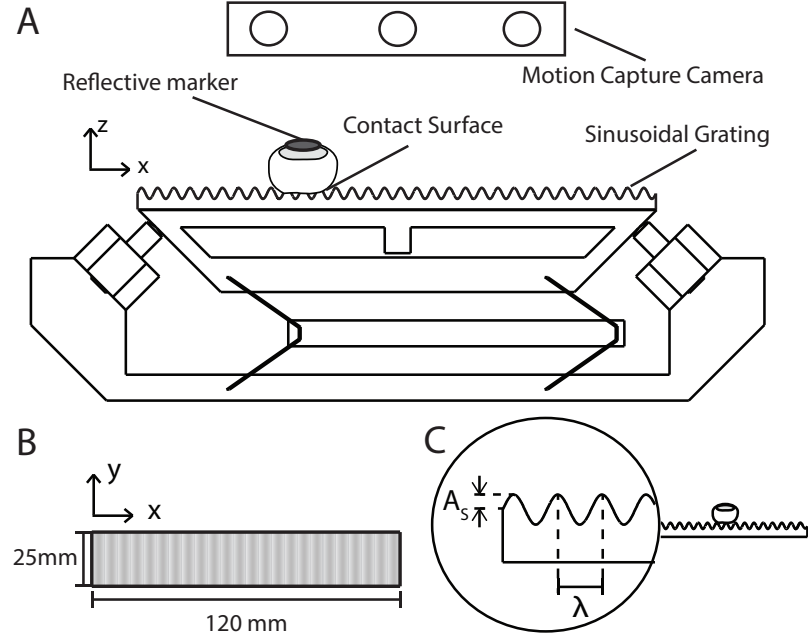
Figure 4.1: A Experimental system designed to measure displacement, normal and tangential forces during sliding contact between a finger and a textured surface. Top (**B**) and front (**C**) view illustrations of one of the eight textured surfaces (all sinusoidal surfaces) used in the experiment; Top dimensions as shown. Eight different textures were employed, differing in a single parameter (spatial scale).

Table 4.1: Measurement conditions for the experiment

	Conditions			
	1	2	3	4
Prescribed sliding speed (v_p)	80 mm/s	80 mm/s	120 mm/s	120 mm/s
Prescribed normal force (f_p)	0.3 N	1 N	0.3 N	1 N

were specified during the experiment, feedback was provided during practice trials via an automated system. A graphical user interface indicated the force level to be produced relative to that performed by the participant during the trial. An audio metronome was used to enforce sliding speed, by indicating the regular tempo at which the finger was to be slid across the surface. Participants were readily able to follow the metronome, but there were variations in force and speed trajectories, due to normal human motor control limitations, as discussed below. Training was provided in advance of each of the four measurement conditions and continued until the participant achieved consistent performance as determined by the experimenter. Prior to data collection in each condition, each of the sinusoidal gratings and finger pad were cleaned using a cotton cloth and isopropyl alcohol.

4.3   Data processing

The discrete time signals from each force sensor were digitized, and used to compute normal and tangential force components $F_N(t)$ and $F_T(t)$ (Eq. 3.1). The measurement conditions were indexed by the surface texture wavelength λ, and the prescribed force level f_p and prescribed speed v_p. We also recorded the position $p_f(t)$ of the finger, but only the x-component was employed. Subsequent processing stages are summarized in Fig. 4.2. The force signals were band pass filtered to remove effects of motor variability and high frequency artifacts. This was accomplished with a zero-phase filter with cutoff frequencies of 15 and 500 Hz. Three zero-phase notch filters (60 Hz, 180 Hz and 300 Hz) were used to eliminate a small amount of power supply interference (Fig. 2); the narrow bandwidth and linear phase response ensured the filter could correct for this interference without significantly affecting the measurements. Position information was re-sampled to 18 kHz to match the sampling frequency of the force data.

Further analysis focused on the tangential (frictional) force component $F_T(t)$. We segmented these signals into trials, each of which consisted of one left-to-right scan of the middle 80 mm of the respective surface. We eliminated 20 mm at each end of the trial to avoid transient effects accompanying the change in direction of motion. For each of the eight wavelengths, two force levels, and two speeds, we considered ten left-to-right trials from each of the nine participants, yielding a total of 2880 signals that were used for our analysis.
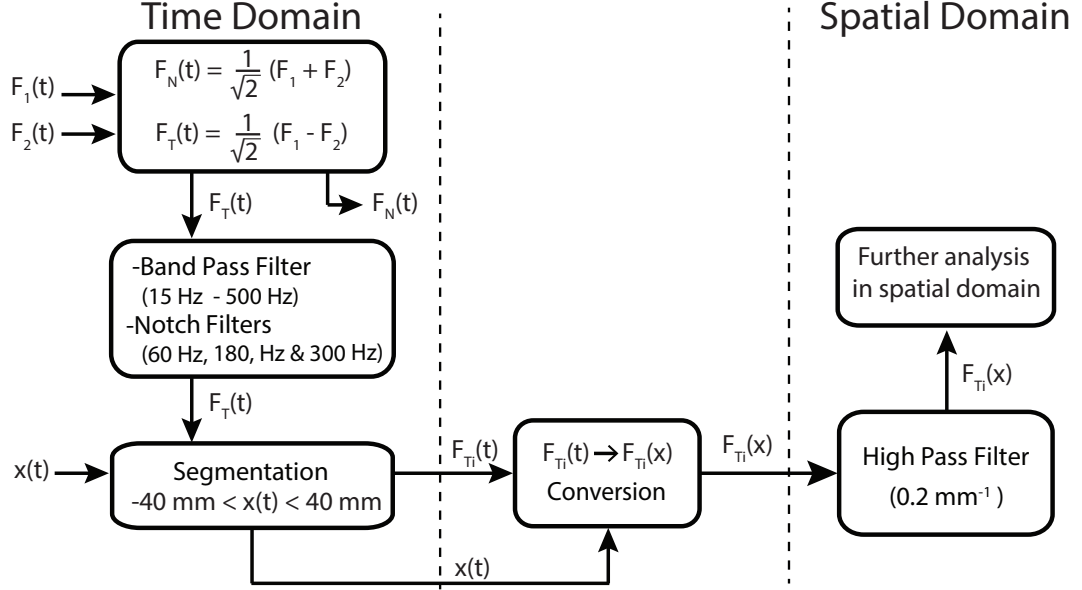
Figure 4.2: Signal processing of the measurements captured in the present investigation, including both time and space domain processing.

Using the method of Wiertlewski et al. [2], we transformed the tangential force for each trial from the time to the spatial domain, yielding a spatial force pattern $F_T(x)$ given by

$$F_T(x) = \mathcal{F}_T(\mathcal{X}^{-1}(x)) \tag{4.1}$$

Here, $\mathcal{F}_T(t)$ and $\mathcal{X}(t)$ are piecewise linear approximations to $F_T(t)$ and $x(t)$. The inverse function of $\mathcal{X}(t)$ was resampled at regular distances, yielding a spatial sample period of 0.01 mm. The resulting spatial domain tangential force data were filtered using a zero-phase high-pass filter with cut-off frequency at 0.2 mm^{-1} to eliminate slow varying fluctuations in the data.

4.4 Stick slip phenomena

A small number of trials in each condition (fewer than three for every participant) exhibited periodic or transient frictional stick slip events, marked by a sustained increase of force magnitude followed by a rapid decrease in force (Fig. 4.3). Consistent with expectations from basic mechanics, these could be assumed to reflect the occurrence of static finger-surface contact (sticking), followed by the rapid resumption of sliding motion (slip) [128–130]. Although interesting, these events occurred
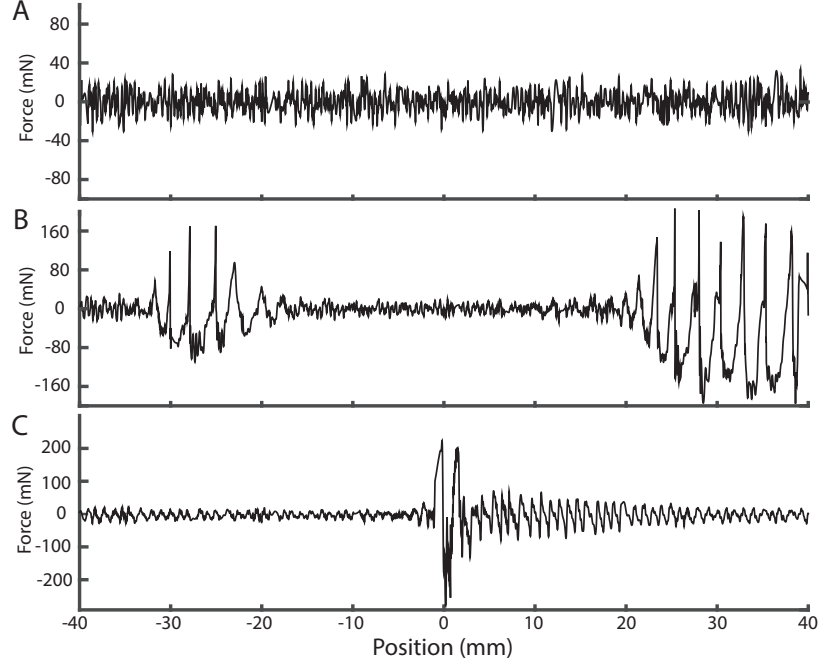
Figure 4.3: Example tangential force signals with and without stick-slip. **A** Trial without stick-slip events, $\lambda = 0.5$ mm, prescribed speed $v_p = 80$ mm/s, prescribed normal force $f_p = 1$ N. **B** Trial exhibiting stick-slip oscillations, $\lambda = 0.5$ mm, $v_p = 80$ mm/s, $f_p = 1$ N. **C** Trial exhibiting transient stick-slip events, $\lambda = 0.5$ mm, $v_p = 80$ mm/s, $f_p = 1$ N.

sparsely and at irregular intervals, and were larger in force magnitude than the regular variations in texture-produced forces that we observed. Consequently, we removed trials in which stick slip events were identified, eliminating a number between 0 and 2 trials for each participant and condition (0 being the common case).

4.5 Amplitude demodulation

In order to eliminate effects of amplitude modulation in the force signals, which were due to changes in the average normal force applied caused by variations in motor activity during sliding of the finger, we processed the force signals in order to remove the modulating effects of an envelope signal $F_E(x)$ using a square law envelope detector, given by

$$\tilde{F}_T(x) = F_T(x)F_E(x), \tag{4.2}$$

$$F_E(x) = \sqrt{F_T(x)^2 * G_{LPF}(x)} \tag{4.3}$$
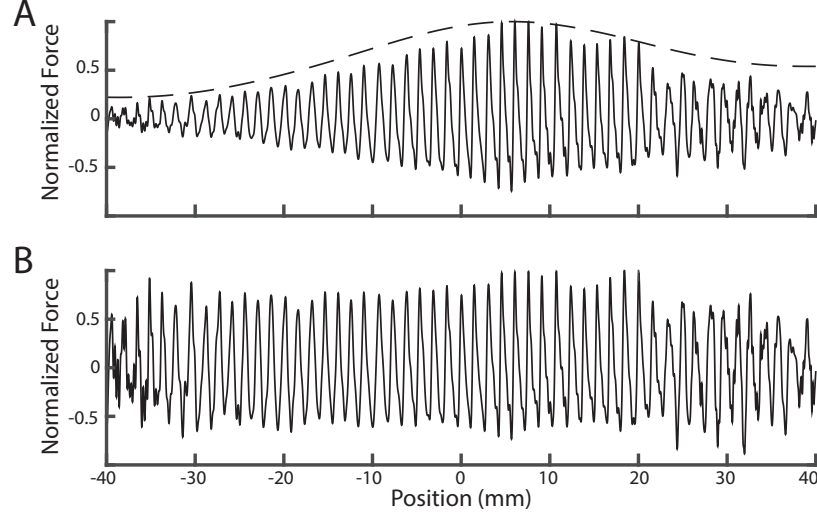
Figure 4.4: Example trial, $\lambda = 1.5$ mm, prescribed speed $v_p = 120$ mm/s, prescribed normal force $f_p = 0.3$ N. **A** Before amplitude demodulation. Force $\tilde{F}_T(x)$ in black, envelope $F_E(x)$ in dashed lines. **B** Demodulated force pattern, $F_T(x)$.

Here $G_{LPF}(x)$ is a zero-phase low-pass filter (cutoff freq. 0.05 mm^{-1}), and $*$ denotes convolution. For each trial, we divided the force signal by the envelope estimate, and normalized the resulting signal (peak amplitude 1 mN), see Fig. 4.4.

4.6 Optimal phase alignment

In order to facilitate the analysis of trial to trial variations in force signals, we processed the force data to compensate for fine differences in contact position between the finger and the surface, which could be attributed to finger orientation or mechanical factors, using an optimization based phase alignment method, and performed an inter-session alignment in order to eliminate phase artifacts due to small variations in system calibration between measurement sessions. The technique we used was inspired by methods previously developed for image comparison in computer vision [131]. The essence of the approach is to determine a rigid displacement τ (in mm) for every trial such that the difference between the force patterns in the ensemble of trials is minimized. To this end, we first aligned all trials in each condition (λ, v_p, f_p) for each participant, in order to compensate for contact mechanical variations due to participant motor behavior. We then estimated a constant phase shift between participants, in order to compensate for artifacts of the measurement configuration (i.e.,

1: $\overline{C} \leftarrow -1$
2: $\overline{F}_T(x) \leftarrow \frac{1}{n} \sum_{i=1}^{n} F_{T,i}(x)$
3: $\overline{C}' \leftarrow \frac{1}{n} \sum_{i=1}^{n} \rho(F_{T,i}(x), \overline{F}_T(x))$
4: **while** $(\overline{C} < 1.05 \, \overline{C}')$ **do**
5:    **for** $i = 1$ **to** n **do**
6:       $\tau_i \leftarrow \arg\max_{\tau} \rho(F_{T,i}(x - \tau), \overline{F}_T(x))$
7:    **end for**
8:    $\overline{F}_T(x) \leftarrow \frac{1}{n} \sum_{i=1}^{n} F_{T,i}(x - \tau_i)$
9:    $\overline{C} \leftarrow \overline{C}'$
10:   $\overline{C}' \leftarrow \frac{1}{n} \sum_{i=1}^{n} \rho(F_{T,i}(x - \tau_i), \overline{F}_T(x))$
11: **end while**

Figure 4.5: Trial alignment algorithm; The quantities $\overline{C}$ and $\overline{F}_T$ were computed on the middle 60 mm of each trial.

slight differences in the position of the optical marker and surface position).

To align trials, we used an optimization algorithm (Fig. 4.5) similar to expectation-maximization, which alternately computed the mean force pattern $\overline{F}_T(x)$ for a given set of offset values τ_i (i indexes the measurement trial)

$$\overline{F}_T(x) = \frac{1}{n} \sum_{i=1}^{n} F_{T,i}(x + \tau_i)$$

and selected the displacements τ_i that maximized, in the respective condition, the (normalized) resultant correlation coefficient $\overline{C}$ with the mean force pattern $\overline{F}_T(x)$,

$$\rho(F_T, \hat{F}_T) = \frac{E(F_T \hat{F}_T) - E(F_T)E(\hat{F}_T)}{\sqrt{E(F_T{}^2) - E(F_T)^2}\sqrt{E(\hat{F}_T{}^2) - E(\hat{F}_T)^2}} \tag{4.4}$$

$$\overline{C} = \frac{1}{n} \sum_{i=1}^{n} \rho(F_{T,i}(x + \tau_i), \overline{F}_T) \tag{4.5}$$

Here $\rho(X, Y)$ is Pearson's correlation coefficient [132]. These two steps were iterated until convergence. The value $\overline{C}$ employed here is similar to the R^2 value for a regression fit. τ_i was constrained to the range from -2 to 2 mm, and the minimum permissible change in displacement was 10 μm. The algorithm terminated when ρ increased by less than 5% (Fig. 4.5).

4.7 Signal entropy

Inspired by prior literature on image alignment [131, 133], we used entropy as an independent assessment of the quality of the phase alignment of the force signals, by computing its change, in each condition (λ, v_p, f_p), before and after alignment. Entropy provides a nonparametric measure of the degree of disorder or dispersion in a distribution of values. Denote by $D_{\lambda, v_p, f_p}(F_T(x))$ the empirical distribution (histogram) among all trials of force values at position x in condition (λ, v_p, f_p). The empirical entropy of the ensemble of J signal values at x is given by

$$H_{\lambda, v, f}(x) = -\sum_j D(F_T(x))_j \log_2 D(F_T(x))_j \tag{4.6}$$

where $D(F_T(x))_j$ is the number of values of $F_T(x)$ in the jth histogram bin. We computed the total entropy among all trials in each condition by integrating the pointwise empirical entropy over the sample

$$\overline{H}_{\lambda, v_p, f_p} = \int H_{\lambda, v_p, f_p}(x)\, dx \tag{4.7}$$

The change in entropy after alignment provided a measure of the extent to which the rigid translations τ_i resulting from the alignment procedure reduced trial to trial variability in the force signals. Stated differently, the entropy values quantified how well the observed variability in force signals could be accounted for by small trial to trial changes in contact position.

4.8 Signal variance

In order to compare the extent of variation in force signals F_T across trials in each condition (λ, v_p, f_p), we computed the ratio of the average signal variance to the Root Mean Square (RMS) amplitude of the mean force pattern $\overline{F}_T(x)$. This ratio, which we refer to as VPR, is given by

$$\text{VPR} = 100 \left(\frac{1}{n} \frac{\sum_{i=1}^{n} \text{var}(F_T(x))}{\text{rms}(\overline{F}_T(x))} \right), \tag{4.8}$$

$$\text{rms}(X) = \sqrt{\frac{1}{N} \sum_{n=1}^{N} \text{abs}(X_n)^2}. \tag{4.9}$$

This ratio was higher when the signal mean in a given condition was less representative of the individual trial measurements.

4.9   Nonlinear distortion

Forces produced as a result of mechanical interactions associated with sliding contact of a finger against a textured surface can exhibit significant nonlinearities [2, 134]. The sinusoidal excitation of a nonlinear dynamical system can yield harmonic signal distortion, which is reflected in the total harmonic distortion Total Harmonic Distortion (THD) of the input-output response of the system given by

$$\text{THD} = \frac{\text{rms}(F_T - HC_0)}{\text{rms}(HC_0)} \tag{4.10}$$

We computed THD in each condition (λ, v_p, f_p) in order to quantify the extent to which our measurements may have reflected such nonlinearities. We extracted the first harmonic component of the signal HC_0 (which coincided with the spatial frequency of the surface) using a band pass filter with a narrow bandwidth of 0.04 mm^{-1} about the fundamental frequency.

4.10   Predictive modeling

We measured force signals produced by interactions between the finger and the textured surface. In order to shed light on these interactions, we adopted an input-output system model with the surface texture height function $h(x)$ as the input and the friction force $F_T(x)$ as output (Fig. 4.6). Other parameters affecting the interaction (sliding speed, normal force, humidity, etc.) were regarded as constant (the foregoing processing helped to ensure this). We adopted a deterministic model, since the fundamental physical processes involved are not stochastic at the length scales of interest, and utilized nonlinear models, since such interactions are known to possess nonlinearities (as further supported by the outcome of the foregoing analysis; See Results, below).

To model our data, we adopted a general black box nonlinear system modeling approach, utilizing NLARX Models (Fig. 4.7). We trained these models on a subset of our data, and assessed their ability to predict forces from surface texture using an independent data set as a control.

The NLARX model related an input signal $u(x) = h(x)$ to an output $y(x) = F_T(x)$ via a time
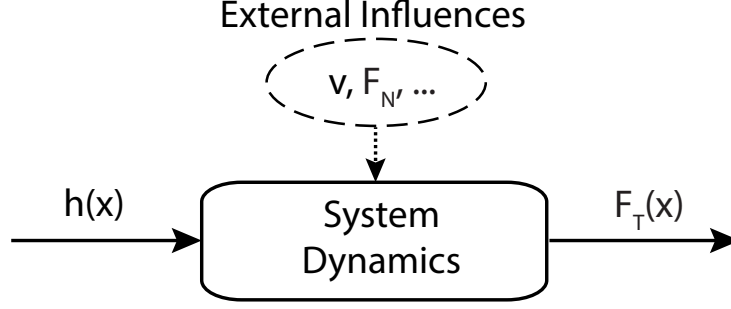
Figure 4.6: Nonlinear dynamical system model mapping an input geometry $h(x)$ to output force pattern $F_T(t)$. Parameters include the speed v_p, contact force f_p. It could be assumed to depend on other factors such as temperature and humidity.

delay nonlinear autoregression. The vector of regressors $\mathbf{r}(x)$ at each x was given by

$$
\begin{aligned}
\mathbf{r}(x) &= (u(x)\ u(x - \delta_s)\ \cdots\ u(x - (n_i - 1)\delta_s) \\
&\quad y(x - \delta_s)\ \cdots\ y(x - n_o\delta_s))^T
\end{aligned} \tag{4.11}
$$

where $\delta_s = 0.01$ mm is the spatial sampling interval. The output $y = y_{\text{lin}} + y_{\text{nl}}$ was a sum of linear and nonlinear terms (Fig. 4.7), with a linear part given by

$$
y_{\text{lin}}(x) = \mathbf{a}^T \mathbf{r}(x) \tag{4.12}
$$

where $\mathbf{a}$ is a vector of linear regression weights that were estimated from data. The nonlinear component had the form of a wavelet nonlinearity

$$
y_{\text{nl}}(x) = \sum_{i=1}^{n_w} \omega_i \kappa(\psi_i(\mathbf{r}(x) - \bar{\mathbf{r}} - \eta_i)), \tag{4.13}
$$

$$
\kappa(\mathbf{u}) = (N - \|\mathbf{u}\|^2)e^{-0.5\|\mathbf{u}\|^2} \tag{4.14}
$$

The parameters ω_i, ψ_i and η_i were the wavelet coefficient, dilation, and translation parameters that were estimated from data as part of the regression. The number of parameters and model
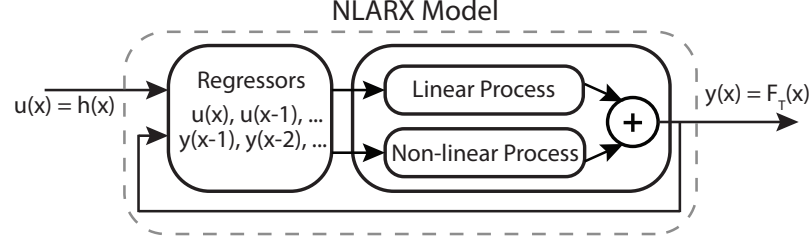
Figure 4.7: Block diagram of the Non-Linear Auto Regressive Exogenous (NLARX) model.

order were determined by values (Table 4.2) obtained via model selection (see below). Estimation was performed with Levenberg-Marquardt search, using the Matlab system identification toolbox (Matlab Release 2014b, The MathWorks, Inc., Natick, Massachusetts).

Table 4.2: NLARX model parameters and search range

Parameter	Description	Span
$n_i = 2k$	Num. Input regressors	k = 1,2,3, ... ,15
$n_o = 2k$	Num. Output regressors	k = 0,1,2, .. . ,15
$n_w = 5k + 1$	Num. Wavelets	k = 0,1,2,3,4,5,6,7
$n_k = 4k$	Num. Nonlinear regressors	k = 0,1,2,3,4,5

The NLARX model structure was selected because it provided a higher average GOF metric (on the data subset tested) than that of several other model alternatives that we evaluated, which included Hammerstein-Weiner (with static nonlinearity) models and linear autoregressive models. The nonlinear part of the NLARX model used was chosen to be modeled by a wavelet network. This type of nonlinearity was selected because its use resulted in a higher average GOF (on the data subset tested) than that of other evaluated alternatives, including single and multiple layer sigmoidal neural networks

The regression weights $(a, m, \omega_i, \psi_i, \eta_i)$ were estimated to minimize the Normalized Root Mean Squared Error (NRMSE) $\epsilon(F_T, \hat{F}_T)$ between the measurements $F_T(x)$ and the model output $\hat{F}_T(x)$, where

$$\epsilon(F_T, \hat{F}_T) = \frac{\|\hat{F}_T - F_T\|}{\|\hat{F}_T - \overline{\hat{F}_T}\|}, \qquad \overline{\hat{F}_T} = \frac{1}{L} \sum_{x=1}^{L} \hat{F}_T(x) \tag{4.15}$$

We estimated an NLARX model for each trial in the spatial domain (60 mm in length), using the first 40 mm for model estimation, and the second 20 mm for testing. Our test criterion was the GOF metric

$$\text{GOF} = 1 - \epsilon(F_T, \hat{F}_T) \tag{4.16}$$

Before training and testing, we used a model selection procedure to determine the order parameters n_i, n_o, n_k and n_w best suited to each measurement condition (Table 4.2). In order to avoid overfitting, we used independent data sets for this purpose, consisting of ten randomly selected trials in each measurement condition; these trials were subsequently excluded from training and testing. A grid search over all even values of the model order parameters was used in order to select those that maximized the sum of GOF metrics between the trials in each respective condition.

4.11   Results

4.11.1   Force patterns before and after phase alignment

The ensemble of trials in each condition exhibit significant variation about the mean $\overline{F}_T(x)$ (Fig. 4.8) both before and after phase alignment of trials. However, the amplitude of the mean signal was increased in all conditions. After alignment, the value of the normalized correlation coefficient $\overline{C}$ increased in all conditions (λ, v_p, f_p), and increased by more than 100% in 29 out of 32 conditions (Fig. 4.9). We used entropy values $\overline{H}_{\lambda,v_p,f_p}$ as an independent and nonparametric measure of the spread between trials. In all 32 conditions, the value of $\overline{H}$ decreased after alignment, indicating that entropy was reduced (Fig. 4.10).

The distribution of displacements τ that were obtained through the optimal alignment procedure provide an indication of the extent of variability in the effective phase offset between force patterns from trial to trial (Fig. 4.11,4.12). Although phase aligning the force signals greatly increased the correlation between trials and decreased the entropy, the values of τ needed to achieve this were very small, on the order of 0.1 mm. No qualitative differences were observed between conditions, and the distribution of displacements was also qualitatively similar for different subjects (Fig. 4.12).
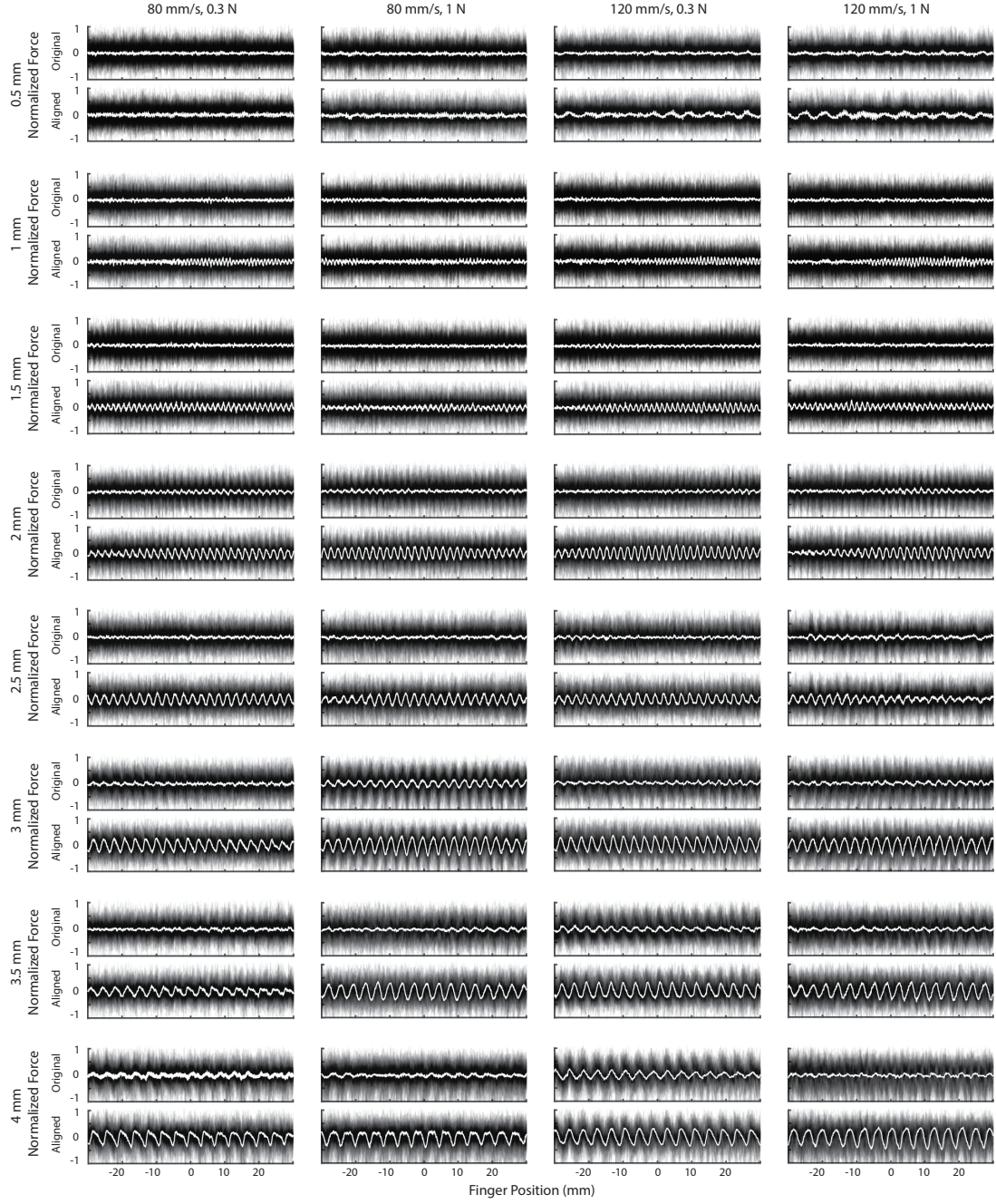
Figure 4.8: Illustration of the effect of alignment under the 32 measurement cases (2 forces f_p, 2 speeds v_p and 8 wavelengths λ). Trials corresponding to all subjects, single trials $F_T(x)$ in black, trials average $\overline{F}_T(x)$ in white. The average between all trials with $\lambda > 1$ mm, shows a pseudo-periodic behavior with the same wavelength as the sinusoidal surface used. The patterns in the averages for the $\lambda = 0.5$ mm and 1 mm surfaces are less readily distinguished by inspection.
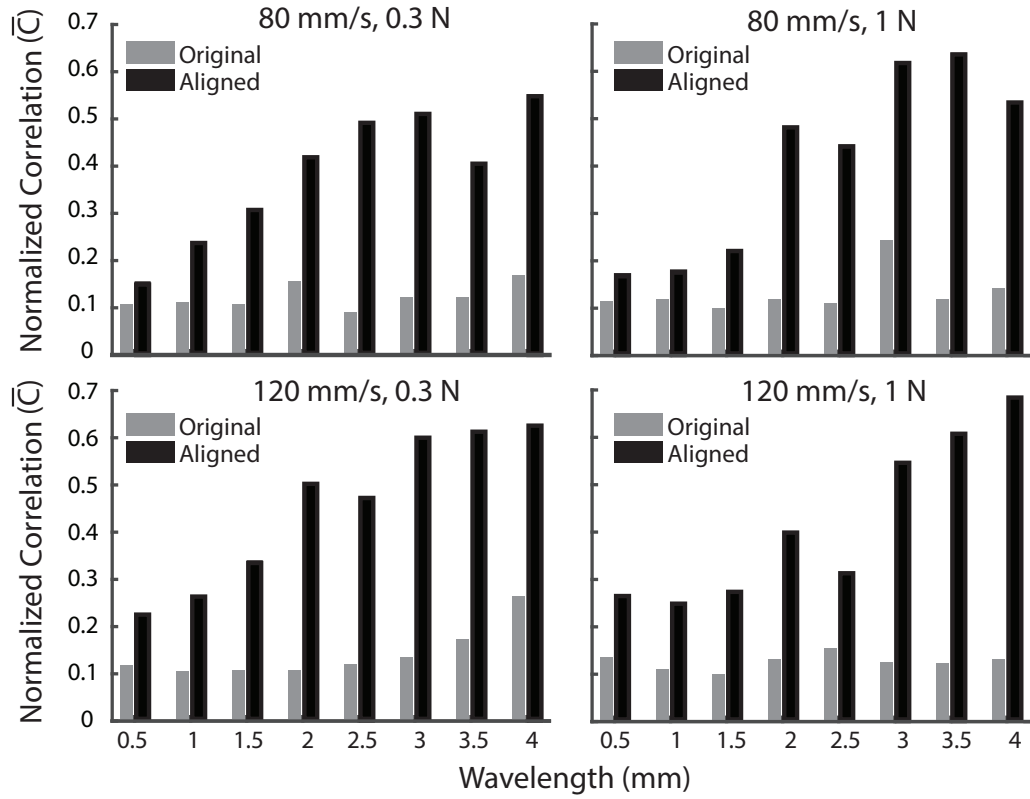
Figure 4.9: Normalized correlation $\overline{C}$ vs. sinusoidal surface wavelength under four measurements conditions, before and after alignment. The alignment process increases considerably the normalized correlation in all cases.
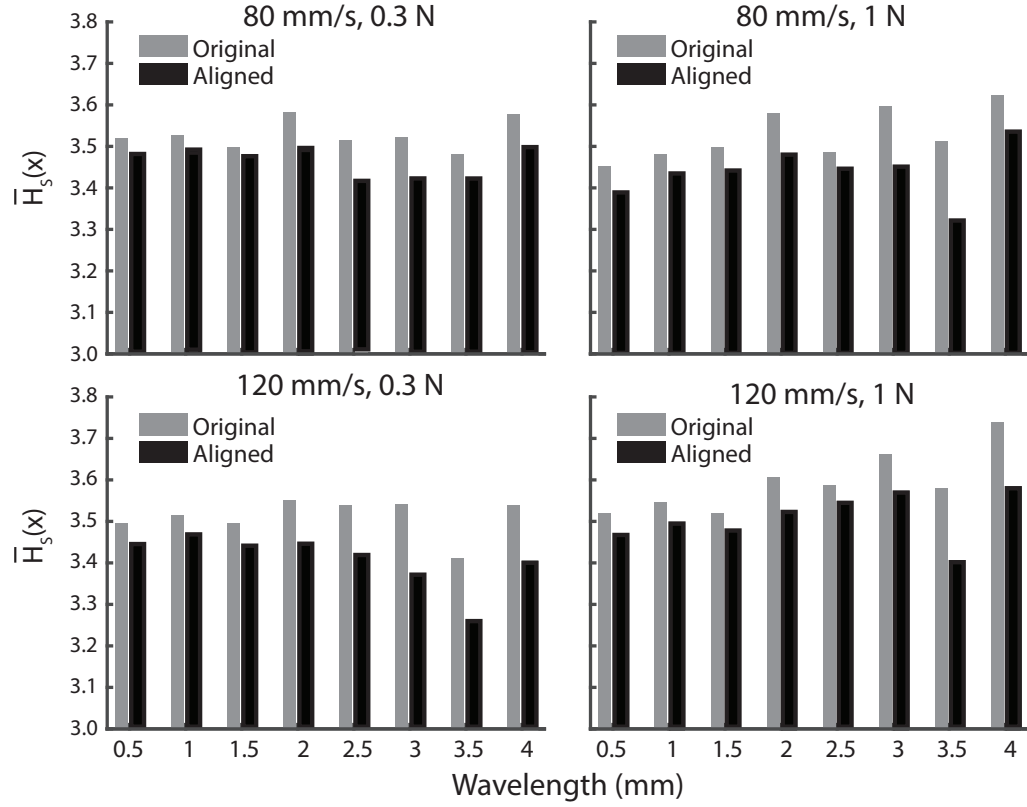
Figure 4.10: Empirical entropy H vs. wavelength λ in all four conditions (v_p, f_p). After the alignment process, the signals show a reduction in the average spatial entropy, indicating a reduction in the variability between trials.
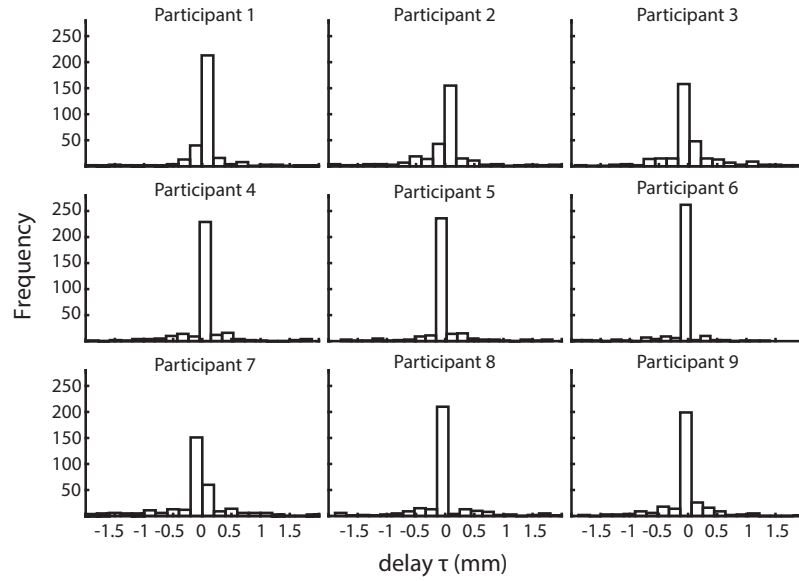
Figure 4.11: Phase alignment histogram grouped by participant. Typical values of τ were small, approximately 0.1 mm.
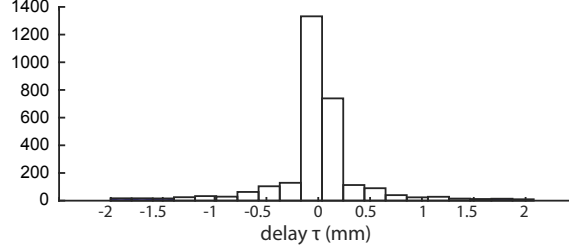
Figure 4.12: Phase alignment histogram for all participants.

4.11.2 Force patterns in spatial domain

At all but the shortest wavelength λ, the mean force signals $\overline{F}_T(x)$ exhibit quasiperiodicity in all conditions, with the wavelength of force oscillation equal to that of the surface (Fig. 4.8). Individual trials also exhibited irregular quasiperiodicity (e.g., Fig. 8). We further measured the extent of variance about the mean signal in each condition using a Variance-to-Power Ratio (VPR) (Fig. 4.14). In all conditions, the highest two values occurred at the shortest wavelength, and the lowest value occurred at one of the longest wavelengths, indicating that there was more variance about $\overline{F}_T(x)$ at low wavelengths, and that the mean $\overline{F}_T(x)$ was more representative at long wavelengths. The data analysis in the spatial frequency domain provided evidence of nonlinearities, in the form of frequency content that was harmonically related to the periodicity of the surface texture (Fig. 4.13). The nonlinearity of the finger-surface interactions is evidenced by the multiple harmonics that are present in the force data. Consistent with prior literature [2, 60], the harmonic amplitude decreased with increasing harmonic number.

Total Harmonic Distortion (THD) was used to measure nonlinearity in the source interactions (Fig. 4.15). These values decreased with wavelength for all values of (v_p, f_p), indicating an increasingly nonlinear relationship between force and surface geometry at smaller spatial scales, or shorter wavelengths.

4.11.3 Predictive modeling

We assessed the extent to which force patterns $F_{T,i}(x)$ could be predicted from surface height $h(x)$ using NLARX modeling. The prediction quality on the test set is shown for all conditions (λ, v_p, f_p)
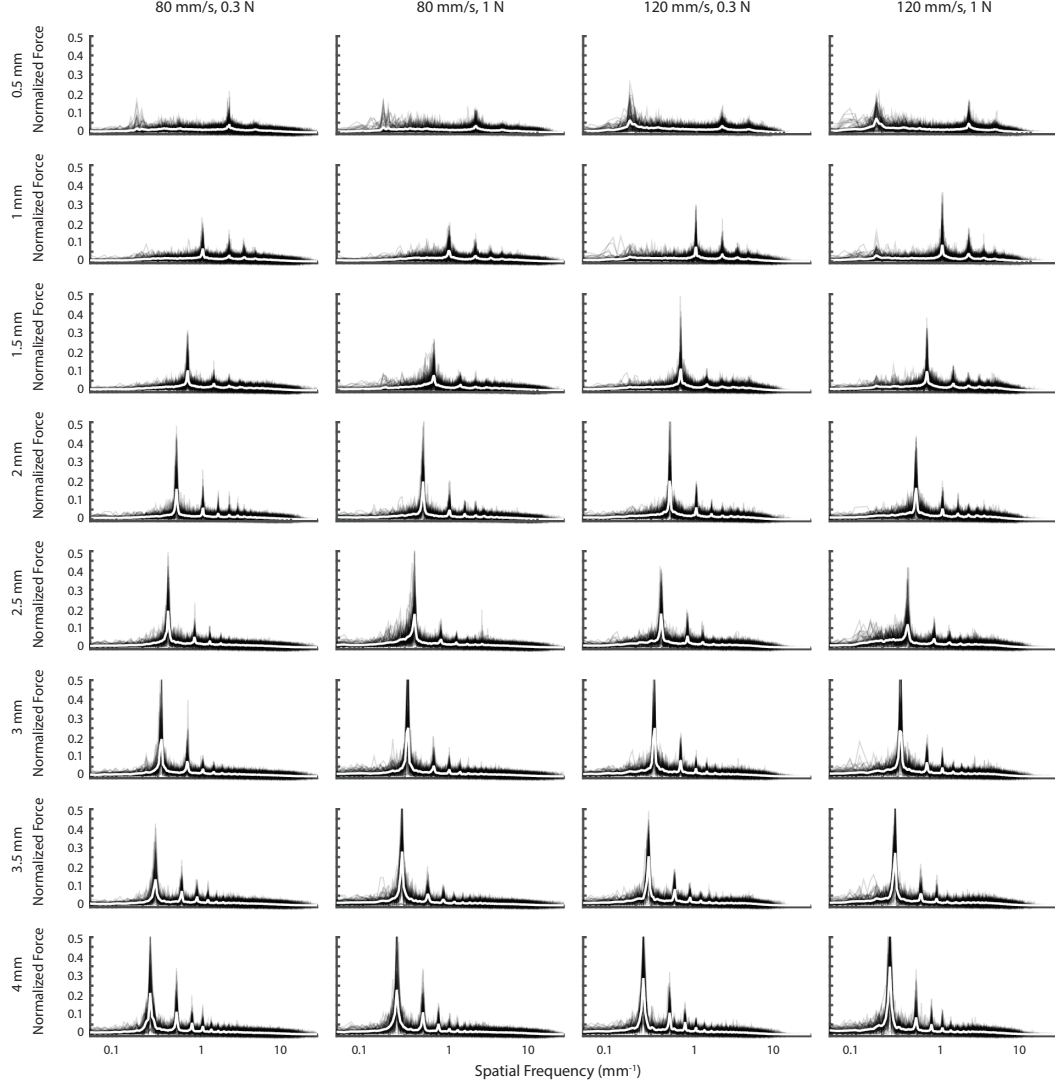
Figure 4.13: The spatial magnitude spectrum of force patterns in all recorded trials (black lines), and all measurement conditions (λ, v_p, f_p). Average of spatial magnitude spectra in white. A series of decaying harmonics is evident, dominated by a fundamental frequency component with the same spatial frequency as the surface texture. Harmonic content for the high spatial frequency surfaces was less evident. In addition, these surfaces manifested a low frequency peak that may be attributed to finger pad mechanics or to low frequency surface noise (which was high-pass filtered in pre-processing stages) or other factors.
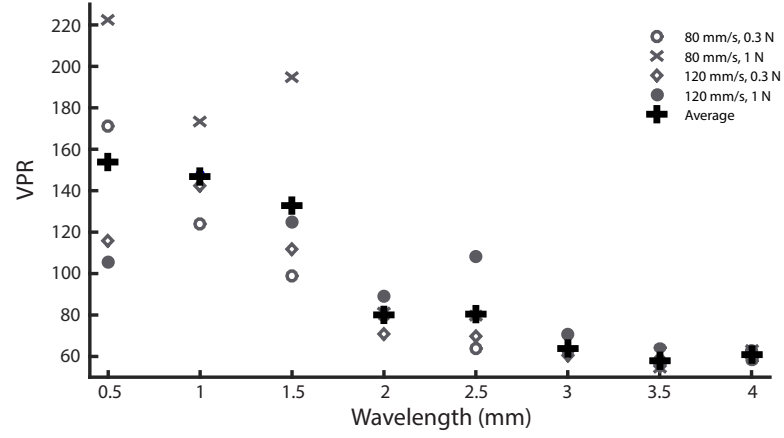
Figure 4.14: Average of Variance-to-Power Ratio (VPR) computed in 90 trials per each wavelength and experimental conditions (λ,v_p,f_p). Different experimental conditions in gray markers, the average VPR of the VPR under the four conditions is shown as black crosses.
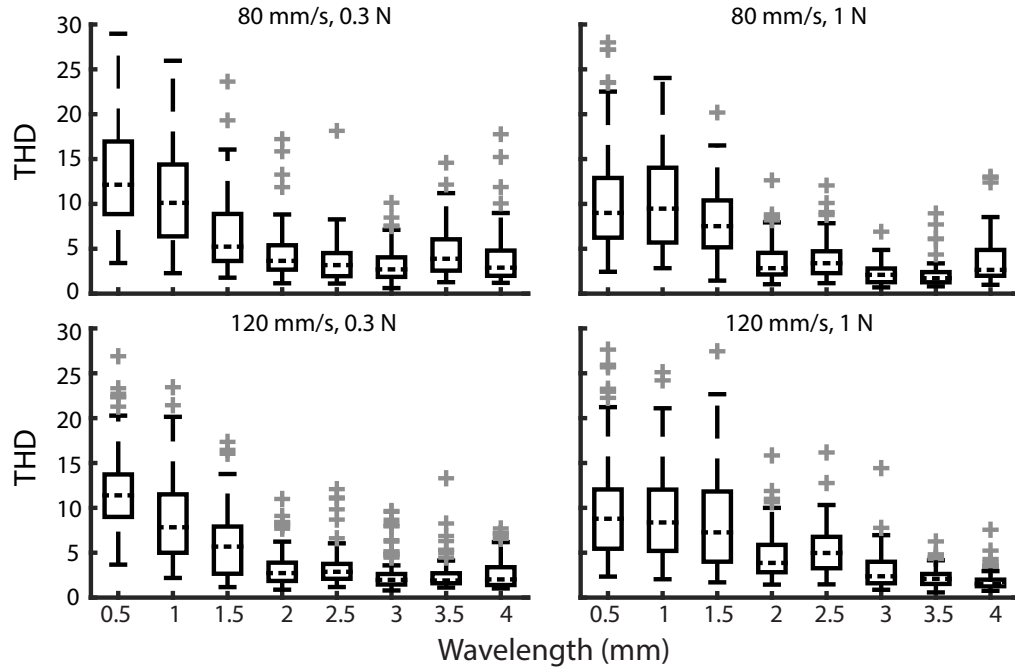
Figure 4.15: Average of Total Harmonic Distortion (THD) computed in 90 trials per each wavelength and experimental conditions (λ,v_p,f_p). Each box plot delimits the region where 80 % of the samples lie, median values marked as dashed lines, outliers marked as gray crosses (Some data points are outside the plot area).
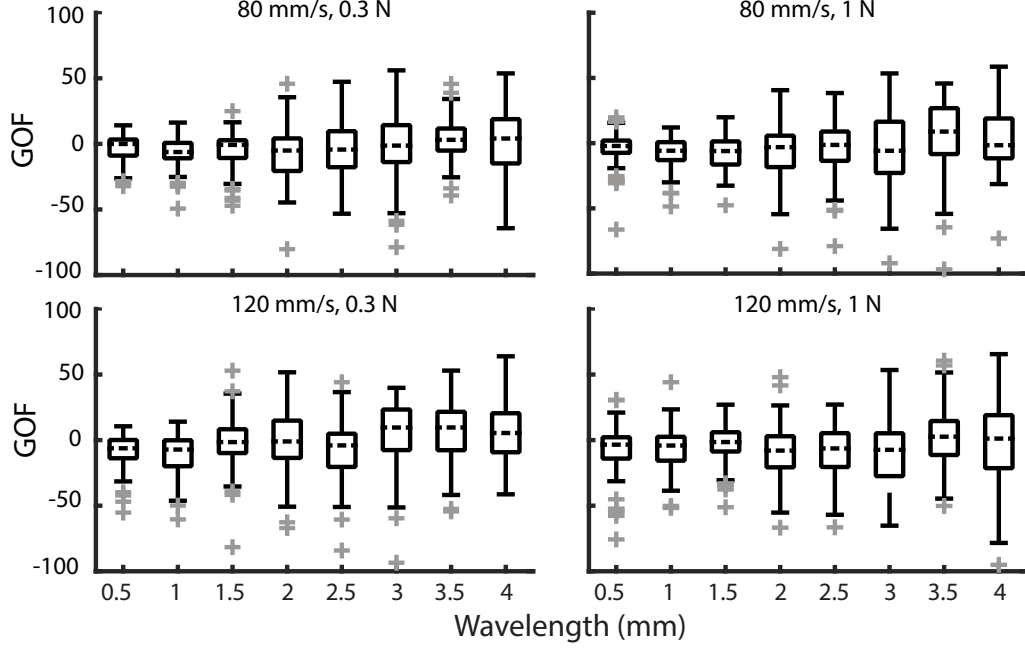
Figure 4.16: Average of NLARX prediction GOF at 4 mm prediction window computed in 90 trials per each wavelength and experimental conditions (λ, v_p, f_p). Each box plot delimits the region where 80 % of the samples lie, median values marked as dashed lines, outliers marked as gray crosses (Some data points are outside the plot area).

in Fig. 4.16. A separate model was fit for each trial, and the model structure was constant for all trials in a given condition (λ, v_p, f_p). We assessed fit quality by computing the average GOF metric for each trial on a moving 4 mm prediction window (Fig. 4.16). The GOF metric could be positive or negative, with higher (more positive) values indicating a better fit. The results increase from near zero at small wavelengths to values of approximately 10, indicating relatively poor predictability in all conditions, but especially so at small spatial wavelengths.

We further investigated the predictability of force patterns from surface geometry by computing correlation values between the model predictions and measurements on a 4 mm prediction horizon, by averaging values of Pearson's correlation coefficient ρ between trials (Fig. 4.17). The highest mean correlation values, near $\bar{\rho} = 0.5$, were observed at the longest wavelengths, indicating that model predictions best matched measurements for the most slowly varying surfaces, but also reinforcing the observation that the force data exhibited important variations, even within a single trial.
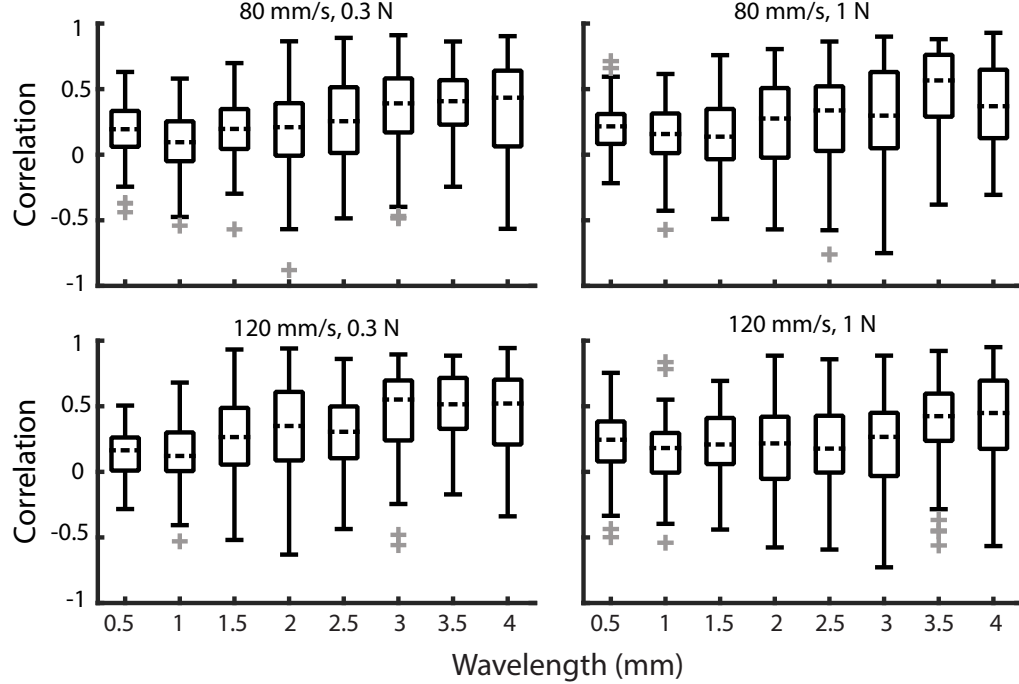
Figure 4.17: Average of NLARX prediction correlation at a 4 mm prediction window computed in 90 trials per each wavelength and experimental conditions (λ, v_p, f_p). Each box plot delimits the region where 80 % of the samples lie, median values marked as dashed lines, outliers marked as gray crosses (Some data points are outside the plot area).

4.12 Discussion

The results provide concrete insight into the frictional forces that are produced during bare-finger sliding contact, and their relation to the geometry of the underlying surface, as well as interaction parameters (v_p, f_p). Most notably, the data we captured exhibited large variability between trials, in essentially all conditions. We hypothesize that this variability is due, in part, to small trial to trial variations in contact conditions. Indeed, our results show that by introducing small signal-dependent offsets in displacement, which were determined through optimization to be on the order of 100 μm, it was possible to greatly increase the amplitude of the mean force pattern in every condition (λ, v_p, f_p), and to reduce the empirical entropy of the force signal ensemble.

Our analysis methods, including spatial domain processing and amplitude demodulation, expressly compensated for variations in applied force f_p and speed v_p. Nonetheless, it is also possible that small trial-to-trial variations in applied force and speed contributed to the trial-to-trial varia-

tions in force that were observed. A further cause may be the nonlinear dynamical nature of the interactions themselves, which can exacerbate all of the aforementioned effects, since nonlinearity is known to amplify dynamical sensitivity to initial conditions. Our analysis demonstrated that at least one measurement of nonlinearity, THD, was highest for textures with the smallest wavelengths. The presence of such nonlinearities was consistent with predictions from prior literature [2]. These same textures exhibited the highest VPR in all conditions (v_p, f_p), indicating that highest trial-to-trial variability where interactions were found to be most nonlinear. Nonetheless, the analysis revealed that several signal features, including the fundamental frequency of spatial force patterns, were stable and well preserved, especially for $\lambda > 1$ mm, despite these variations. Such signal components might be hypothesized to be cues that aid the perceptual recovery of surface texture. For smaller wavelengths ($\lambda = 0.5, 1$ mm), however, the fundamental and harmonic components of the signals were less prominent.

Although we evaluated a large number (nearly 8000) candidate models for predicting spatial force patterns $F_T(x)$ from surface height $h(x)$, the NLARX system models we estimated from data proved to have limited predictive power, even when evaluated on a short horizon of 4 mm, possibly due to the aforementioned signal variability. Consequently, it was difficult to identify any clear relation between the interaction conditions and the quality of fit (GOF metric) or the correlation between the true and predicted force pattern. However, we did observe modestly higher correlation values in the long wavelength conditions, which might indicate that prediction is somewhat more accurate at longer spatial scales. In previous work (using data captured from a different apparatus and different textured surfaces), we observed that it was possible to predict the mean force pattern $\overline{F}_T(x)$ with reasonable quality using similar models, and that prediction quality was dramatically better at wavelengths λ of at least 3 mm [60]. However, perhaps due to the overwhelming variability in the force signals recorded in individual trials, as were analyzed in the present experiment, no clear conclusion could be drawn here about the predictability of forces produced from interaction with long versus short wavelength surface textures.

4.13 Conclusion

The forces that result from sliding contact of a bare finger with a textured surface depend on a number of factors, including the geometry of the surface, the detailed nature of finger-surface contact, and the time-varying exploratory trajectory of the finger. Here we focused on the integrated (resultant) frictional force between the finger and surface. Our results suggest that macroscopic knowledge of these parameters is insufficient to constrain force production. Even when sliding over very regular textures, and correcting for temporal and contact differences, frictional forces were observed to vary greatly from moment to moment and trial to trial.

Although our study did not directly investigate texture perception, it does raise relevant questions. Informally, the textured surfaces used in this investigation all feel highly regular; when exploring them with the finger one is left with the impression of a perceptually constant, regular, corrugated surface. This stands in stark contrast to the variability seen in individual force trials, from which one might, a priori, expect a perceiver to feel something different every time that the finger is stroked along the sample. How is the apparent perceptual stability of surface texture achieved, and which features of these signals enable the nervous system to solve this problem? The latter question is also highly relevant to the problem of haptic rendering. Many techniques have been developed for accurately reproducing frictional forces produced by a virtual surface, including those based on force feedback devices [135] and surface haptic displays [112]. Although other possibilities have been explored in the literature, one attractive option is to specify the surface texture geometrically, in the spatial domain. However, our results strongly suggest that such a specification, even when combined with measured interaction parameters (such as speed, position, and normal force), are by themselves insufficient to constrain the actual forces that should be produced in order to simulate interactions with the surface. Consequently, it is far from clear what rendering algorithm might be appropriate for producing realistic texture-generated forces from geometric surface specifications. One approach to this problem could be based on perceptual criteria, but as alluded to above, it is not obvious what the most perceptually salient features of these force signals may be.

Despite the promising nature of this study, several open questions remain, and additional research

could shed further light on them. Based on our experiment, it was not possible to definitively identify the origin of the force fluctuations that we observed. Possible factors include the continuum dynamics of the finger pad, interactions with the finger ridges, the multi-contact surface that is involved, the presence of unstable stick-slip motion, or other unstable or chaotic modes of oscillation (possibly created by nonlinearities in the finger-surface interaction forces). In order to clarify which of these may be important, further research is needed on the dynamics of force production between the bare finger and a textured surface. Although the measurement apparatus presented here improves greatly on that presented in our preliminary work [60], one with greater temporal resolution and bandwidth would further aid this line of inquiry. A system that facilitates direct measurement of the complex contact geometry and local forces would allow a more direct investigation of the mechanics involved, but such a device has not yet been realized. The nonlinear models that we developed, after extensive search in model space, used data driven system identification methods that proved unable to fully capture the dynamics of finger-surface interactions. While this suggests the challenging nature of this task, further work is needed in order to explore what model structures might more effectively capture the dynamics. In future efforts, we aim to develop force production models that explicitly integrate models of contact mechanics and finger dynamics. This work will also be complemented by research aimed at identifying the mechanical signal features that are most salient to texture perception. Finally, we studied force production for a limited range of surfaces, materials, and interaction parameters. We plan to generalize further in future work using periodic and non-periodic textured surfaces with different shapes and study the frictional forces elicited to better understand the how the texture profile and the finger account for their generation.

Chapter 5: Predicting sliding friction forces with a partial contact differential pressure model

In chapter 4 we measured frictional forces of bare fingers sliding on sinusoidal surfaces with wavelength (λ) smaller than the size of the finger ($\lambda \leq 4$ mm). We used Non-Linear Auto Regressive Exogenous (NLARX) models to predict these frictional forces. The NLARX models proved insufficient to capture and reproduce the patterns in frictional forces accurately.

Consider a finger making contact with the surface of an object with relief features of size smaller than the finger. This situation would cause the finger to be in touch with the high relief features more than the bottom parts of it (see Figure 5.1). A model that accounts for the contact discontinuities is expected to aid accurate frictional force production modeling.
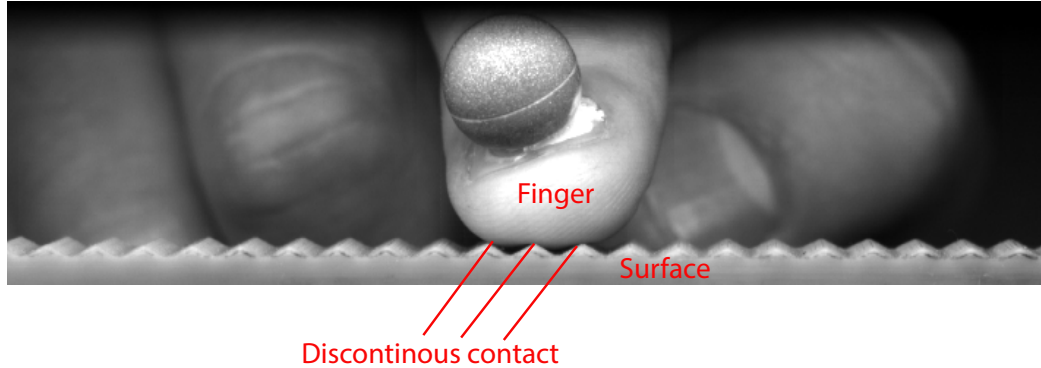
Figure 5.1: Grayscale picture of a real finger sliding on an undulating surface ($\lambda = 4$ mm). The image was obtained during one of the trials described in chapter 4. Dark areas under the fingertip are not in contact with the surface.

We sought to identify a model that could capture both the biomechanical response of the finger tissue and the effects of intermittent contact with the surface. Our approach builds in part upon a recently proposed model that accounts for the differential pressure in the finger pad, as proposed by Fujii et al. [84]. This model is applicable for a bare finger sliding on sinusoidal surfaces with wavelength larger than the size of the finger ($\lambda \geq 10$ mm). Hence, it is not directly applicable to our study because the wavelength of the surfaces we used is $\lambda \leq 4$ mm. This model yielded poor results on our data during preliminary research.

We adopted a similar approach to model differential pressure in the finger produced by small scale finger-surface interactions, re-scaling the differential pressure model to better suit the surfaces of interest. We combined it with a saturating function nonlinearity that accounts for disconnection between the finger and the bottom parts of the surfaces. To further simplify the model formulation, we hypothesized that the total frictional force can be accounted by a single (small) contact region sliding over the surface.

This chapter thus presents a partial contact differential pressure model composed by: 1) A saturating function, 2) Scale-reduced differential pressure model, and 3) A band-pass filter.

The effectiveness of the model was measured in terms of Pearson's correlation coefficient (ρ) and Goodness Of Fit (GOF) metrics. We compared these metrics to those obtained using NLARX models. The comparison showed that the partial contact differential pressure model captures the gross patterns of the frictional forces measured with higher accuracy than NLARX models.

5.1 The partial contact differential pressure model derivation

We seek to model frictional forces ($F_T(x)$) as the output of a system that takes surface height ($h(x)$) as input (See Figure 4.6). Both input and output of the system are defined as functions of the fingertip position x.

A finger making contact with the surface of an object with small relief features would be in touch mostly with the high relief features. The fingertip has limited elasticity and, for sufficiently non-flat surfaces, never contacts the lowest relief features [40] (see Figure 5.1). Here we model the fingertip contact disconnection with the surface as a saturating function of the form:

$$h_{sat}(x) = \begin{cases} h(x) & h(x) \geq h_{thr} \\ 0 & h(x) < h_{thr} \end{cases} \tag{5.1}$$

Where h_{thr} represents the minimum height at which the finger loses contact with the surface described by $h(x)$. We envision using such a high-relief surface function ($h_{\text{sat}}(x)$) as a means of

approximating the finger-surface contact geometry. The surface function $h_{\mathrm{sat}}(x)$ is used as input for a scale-reduced version of the differential pressure model [84].

5.1.1   The differential pressure model

To account for the mechanical response of finger tissues to surface height variations, we used a differential pressure model inspired by research of Fujii et al. [84] on large-scale surface variations. This differential pressure model uses Hertz contact theory and geometrical analysis to derive a parametric model that accounts for force generation of a finger sliding over raised surface features. In this scenario, the two objects in contact are the finger and the solid surface touched.

In this model, two pressure points were enough to account for frictional force production of the whole finger (see Fig. 5.2 B) as it slides over the sinusoidal surface. The two pressure points were used to obtain the ratio between tangential force and normal force applied by the finger onto the surface. Each of the two pressure points are modeled as a single contact "ball bearing" model.

In a single contact "ball bearing" model (Fig. 5.2 A), the ratio between the tangential force $F_{bT}(\mathrm{x})$ and normal force $F_{bN}(\mathrm{x})$ components at a position x along a surface is defined by:

$$Q(x) = \frac{F_{bT}(x)}{F_{bN}(x)} = \frac{\tan \alpha(x) + \mu}{1 - \mu \tan \alpha(x)} \qquad (5.2)$$

Here $\alpha(x)$ is the slope of the surface at point x, and μ is the friction coefficient between the finger and the surface. Equation 5.2 allows computing the ratio of tangential force to the normal force under single contact point conditions.

The finger in touch with a surface exerts a pressure which is distributed non-uniformly over the surface. According to Hertz's contact theory [81], in a contact region between two objects the pressure is distributed in a parabolic manner with the maximum pressure $P_{\max}$ located at the center of the contact region. Assuming that the contact region has diameter of $2R_s$, the pressure at a point located at a distance r from the center of the contact region (which is the fingertip center position

x in our case) is given by

$$p_f(x + r) = P_{\max}\sqrt{1 - (\frac{r}{R_s})^2} \tag{5.3}$$

Assuming that the radius of curvature of the finger is R_f, when the finger is on an inclined surface with slope angle α (Figure 5.2 B), the pressure point r is displaced horizontally by a factor of $\sin\alpha$. Considering this displacement, Eq. 5.3 becomes

$$p_f(x + r) = P_{\max}\sqrt{1 - (\frac{r - R_f \sin\alpha(x)}{R_s})^2} \tag{5.4}$$
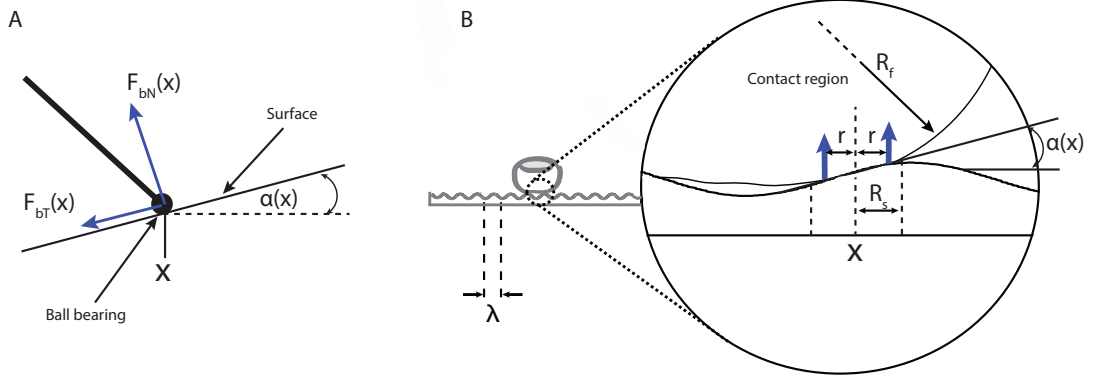
Figure 5.2: Partial contact differential pressure model illustration. **A.** Ball bearing contact model free body diagram illustrating the surface normal and tangential reaction forces ($F_{bN}(\mathrm{x})$ and $F_{bT}(\mathrm{x})$ respectively). **B.** Partial contact differential pressure model illustrating radius of curvature of the finger at the contact region (R_f), the radius of the contact region (R_s) and the pressure points located at a distance (r) from the contact region center x.

Equation 5.4 allows the computing of the ratio between the normal and tangential forces applied at an arbitrary point in the fingertip contact area, as long as $r \leq R_s$. The conversion of pressure to force is given by $F_N = p_f \cdot dA$, where dA is an infinitesimal area. Since the differential pressure model focuses on computing the ratio $\frac{F_T(x)}{F_N(x)}$, the implicit equivalency $p(x + r) = F_{bN}(x + r)$ is assumed.

Considering the total normal and tangential forces ($F_N(\mathrm{x})$ and $F_T(\mathrm{x})$ respectively) as the sum of the normal and tangential forces from two ball bearing elements located at distances r and $-r$

from the center of contact area (x), equations (5.2) and (5.4) can be combined to yield

$$\frac{F_T(x)}{F_N(x)} = \frac{F_{bN}(x+r)Q(x+r) + F_{bN}(x-r)Q(x-r)}{F_{bN}(x+r) + F_{bN}(x-r)} \tag{5.5}$$

If we assume that a constant normal force F_N is applied, the total tangential force at a finger position x can be estimated by

$$\hat{F}_T(x) = F_N \frac{\sqrt{1 - (\frac{r - R_f \sin(\alpha(x))}{R_s})^2}Q(x+r) + \sqrt{1 - (\frac{-r - R_f \sin(\alpha(x))}{R_s})^2}Q(x-r)}{\sqrt{1 - (\frac{r - R_f \sin(\alpha(x))}{R_s})^2} + \sqrt{1 - (\frac{-r - R_f \sin(\alpha(x))}{R_s})^2}} \tag{5.6}$$

The input to this model is the geometry of the surface, represented in terms of its slope angle $\alpha(\text{x})$. The output is the tangential force $F_T(\text{x})$. The model depends on three main parameters (R_f, R_s, r), that are affected mainly by the characteristics of each interaction.

5.1.2   The partial contact differential pressure model

The force model of equation 5.6 is valid when the diameter of the finger is less than the wavelength of the surface. When this is not the case, the most important consequence is that the finger contacts the surface at more than one discontinuous regions. We modeled this by using a saturating function (Eq. 5.1), whose output represents the discontinuous surface contact regions.

For this case, each contact region can be treated as independent. Compared to the model of Fujii et al. [84], the contact parameters R_f, R_s and r are scaled to reflect the typical dimensions of a contact region. Moreover, we simplified the partial contact differential pressure model by assuming the frictional forces are dominated by the a single contact region, located close to the center of mass of the finger.

In order to account for the viscoelasticity of the finger tissues, we used a low pass filter modeling the dynamic response of the fingertip, which eliminates high frequency components. In order to facilitate comparison with our experimental results (which have no DC component), we also filtered out the near DC force components from the output of the model, making this last step a band-pass filter with lower cutoff frequency at 0.1 mm^{-1} and upper cutoff frequency at 2 mm^{-1}.

The partial contact differential pressure model we propose takes the surface height $h(x)$ as input

A
Partial contact lumped parameter model

$h(x)$ → Saturation function $h_{SAT}(x) = \begin{cases} 0, & h(x) < thr \\ h(x), & h(x) \geq thr \end{cases}$ → $h_{SAT}(x)$ → Differential pressure model $\hat{F}_T(x) = f(s, r, R, \mu, F_N)$ → $\hat{F}_T(x)$ → Band pass Filter → $\hat{F}_T(x)$

B $h(x)$ $h_{SAT}(x)$ $\hat{F}_T(x)$
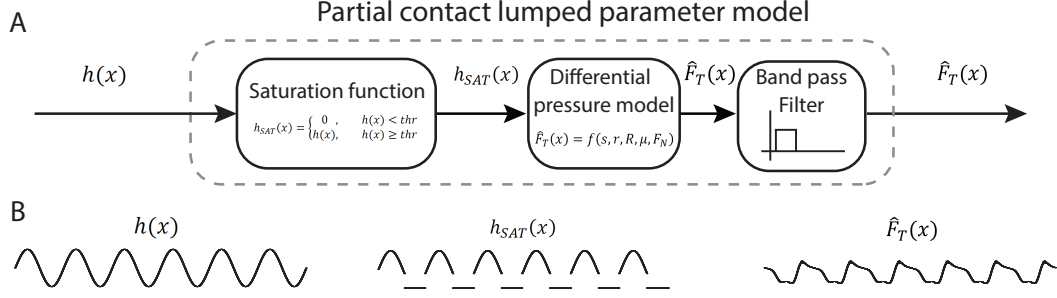
Figure 5.3: A. Partial contact differential pressure model block diagram. Each block from left to right are: 1) a saturating function (Eq. 5.1) representing the intermittent finger-surface contact, 2) a local (small-scale) differential pressure model (Eq. 5.6) and 3) a band-pass filter, accounting for tissue viscoelasticity and measurement bandwidth. **B.** Typical signals used and produced by the model. Each signal represent (from left to right) represend: 1) input $h(x)$, 2) saturating function output $h_{\text{sat}}(x)$, and 3) output generated by the model $F_T(x)$.

and produces a frictional force $F_T(x)$ as output. The model is illustrated in Figure 5.3 and consists of a cascade of three sub-systems: 1) A saturating function (Eq. 5.1) representing the intermittent finger-surface contact, 2) A local (small-scale) differential pressure model (Eq. 5.6) and 3) A band-pass filter, accounting for tissue viscoelasticity and measurement bandwidth.

5.2   Data set used for validation

The data set used to validate the partial contact differential pressure model was composed of data from 4 subjects sliding their index fingers 10 times over each of two sinusoidal surfaces of spatial period $\lambda = 2$ mm and 4 mm, under four measurement conditions. The four measurement conditions consisted in two different prescribed normal forces ($f_p = 0.3$ N and $f_p = 1$ N) and two different prescribed average sliding speeds ($v_p = 80$ mm/s and $v_p = 120$ mm/s).

A total of 320 frictional force measurements were available[1]. The center segment of 24 mm, of each signal ($-12 \leq x \leq 12$ mm) was considered for validation of the partial contact differential pressure model.

---
[1]This is a subset of a data set described in detail in Chapter 4
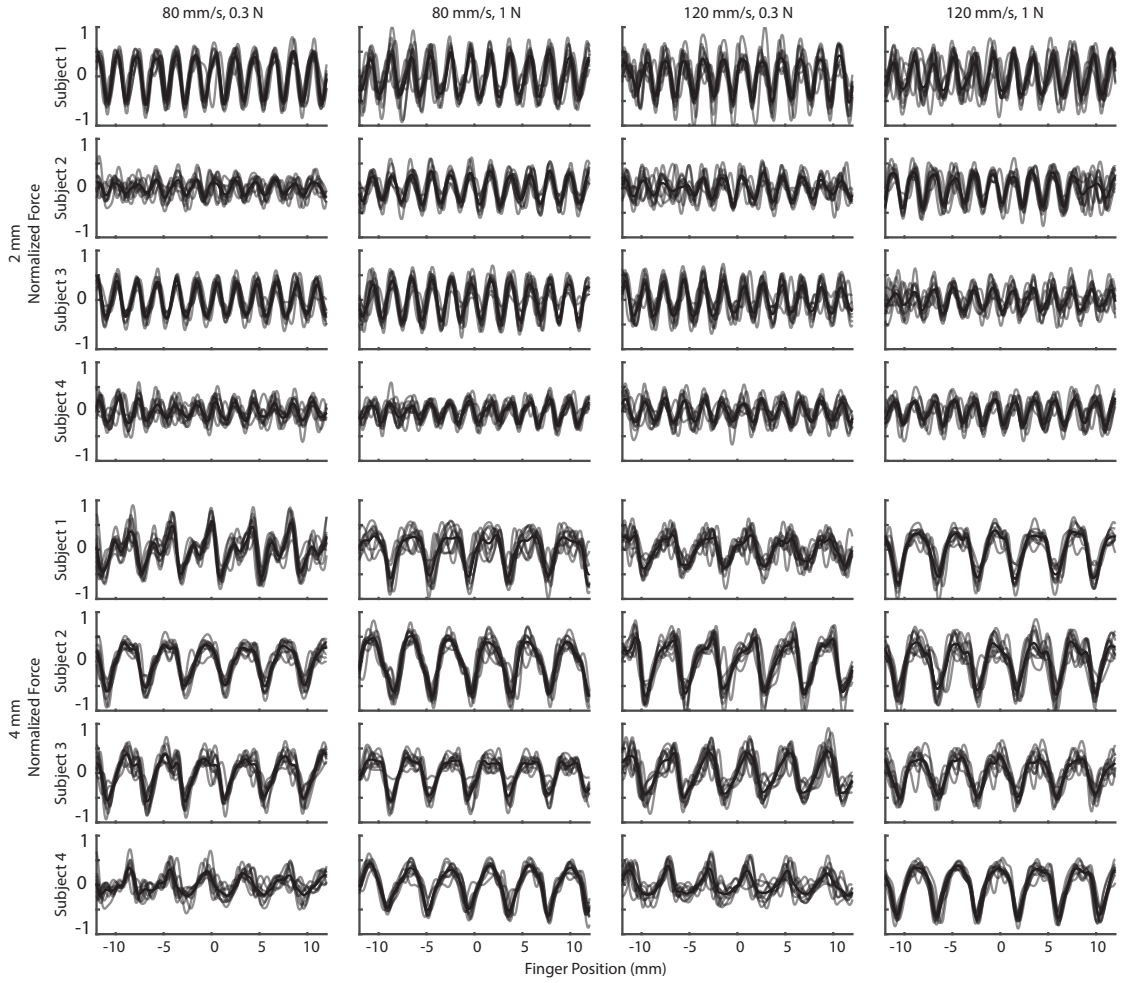
Figure 5.4: Data subset used for validation of the force generation model. Data from two subjects measured under four different sliding conditions. Ensemble of 10 trials in each box grouped by measurement condition and subject. Individual signals in gray-scale, mean of 10 trials in black.

5.3 Optimizing the model parameters to fit the data

The parameters R_s, R_f, r, μ and h_{thr} were tuned for each measured signal by minimizing the Normalized Root Mean Squared Error (NRMSE) $\epsilon(F_T, \hat{F}_T)$ between each signal F_T and the estimated output $\hat{F}_T$ from the model (Eq. 5.7). This process was conducted using a custom made GUI programmed in MATLAB to allow visualization of each F_T measurement together with the estimate from the model, $\hat{F}_T$. The GUI allowed the experimenter to manually modify the parameters of the model and displayed the NRMSE, thus providing an indication used to obtain an estimate $\hat{F}_T$ close to each measurement F_T.

A total of 320 signals were used for this validation. The parameters used were stored together with the Pearson's correlation coefficients ρ (Eq. 5.9) between the measurement and the force estimate as well as the GOF (Eq. 5.8).

$$\epsilon(F_T, \hat{F}_T) = \frac{\|\hat{F}_T - F_T\|}{\|\hat{F}_T - \overline{\hat{F}_T}\|}, \qquad \overline{\hat{F}_T} = \frac{1}{L_x}\sum_{x=1}^{L_x}\hat{F}_T(x) \tag{5.7}$$

$$\text{GOF} = 1 - \epsilon(F_T, \hat{F}_T) \tag{5.8}$$

$$\rho(F_T, \hat{F}_T) = \frac{E(F_T\hat{F}_T) - E(F_T)E(\hat{F}_T)}{\sqrt{E(F_T{}^2) - E(F_T)^2}\sqrt{E(\hat{F}_T{}^2) - E(\hat{F}_T)^2}} \tag{5.9}$$

5.4 Results

We obtained 320 force estimates $\hat{F}_T$ for each force measurement F_T. Individual tangential force signals showed variable patterns for different sliding scans. These differences were accentuated by differences in sliding speed, normal force applied and subject. Examples of typical F_T measurements with the corresponding $\hat{F}_T$ computed from the partial contact differential pressure model are shown in Figure 5.5.
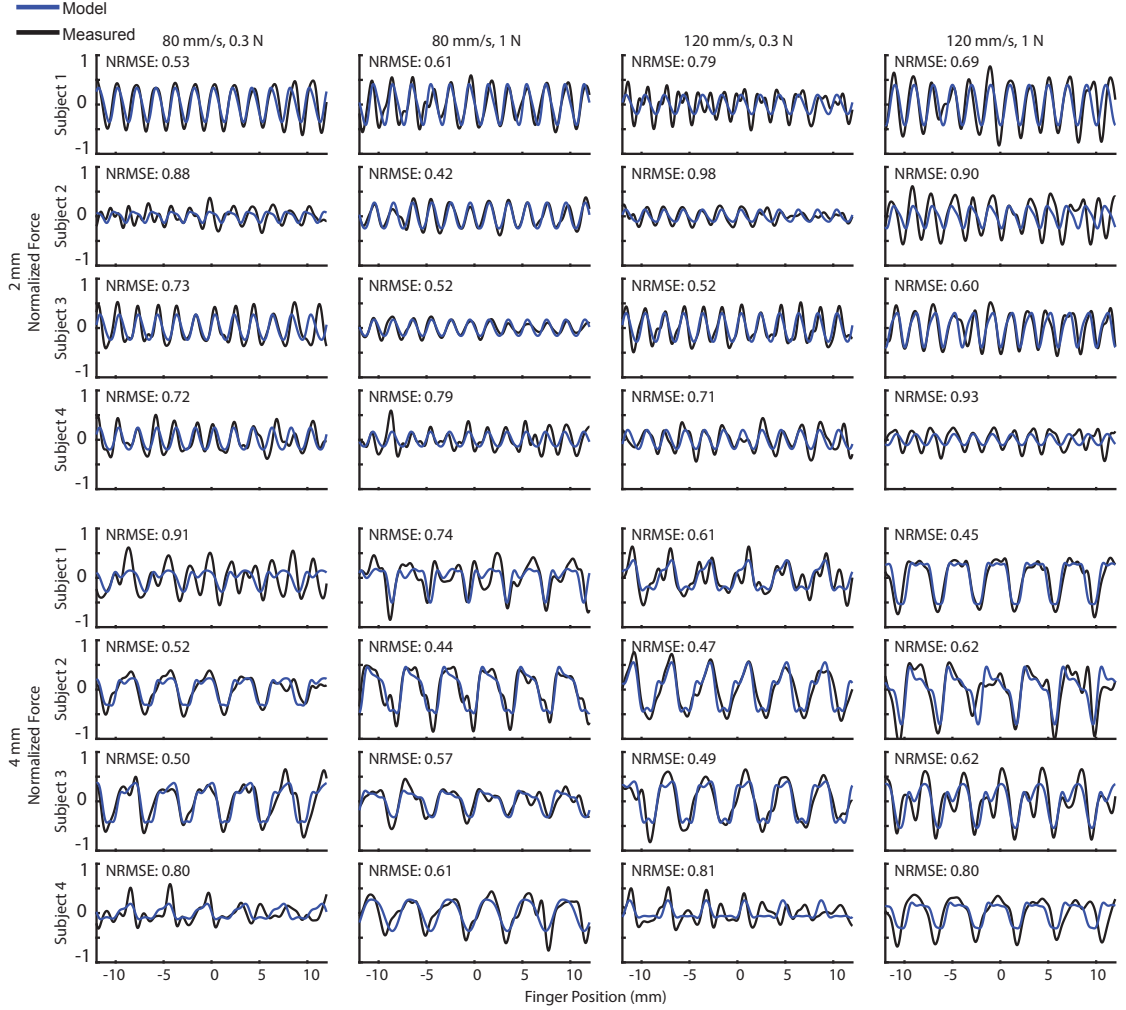
Figure 5.5: Typical F_T measurements and their corresponding force estimates using the partial contact differential pressure model $\hat{F}_T$. Data displayed corresponds to frictional forces elicited by four subjects sliding their bare finger over two surfaces ($\lambda = 2$, 4 mm) under four measurement conditions (see Table 4.1). F_T measurements in black and their corresponding force estimates $\hat{F}_T$ in blue. The Normalized Root Mean Squared Error (NRMSE) is indicated for each case.

Figure 5.5 illustrates that the partial contact differential pressure model may be capable of capturing the gross patterns present in the measurements. Small scale differences are observed which we quantified in terms of the GOF. We compared the 320 GOF metrics to those obtained for the same measurements using NLARX models. Figure 5.6 shows a summary of the GOF metrics computed using both the NLARX approach and the partial contact differential pressure model. The GOF improves with increasing wavelength (λ) of the surface touched. This suggests that the models used here perform better over surfaces that vary slowly. Also, the partial contact differential pressure model was better than NLARX models, showing higher GOFs. This held true irrespective of the normal force applied f_p and the average sliding speed v_p.
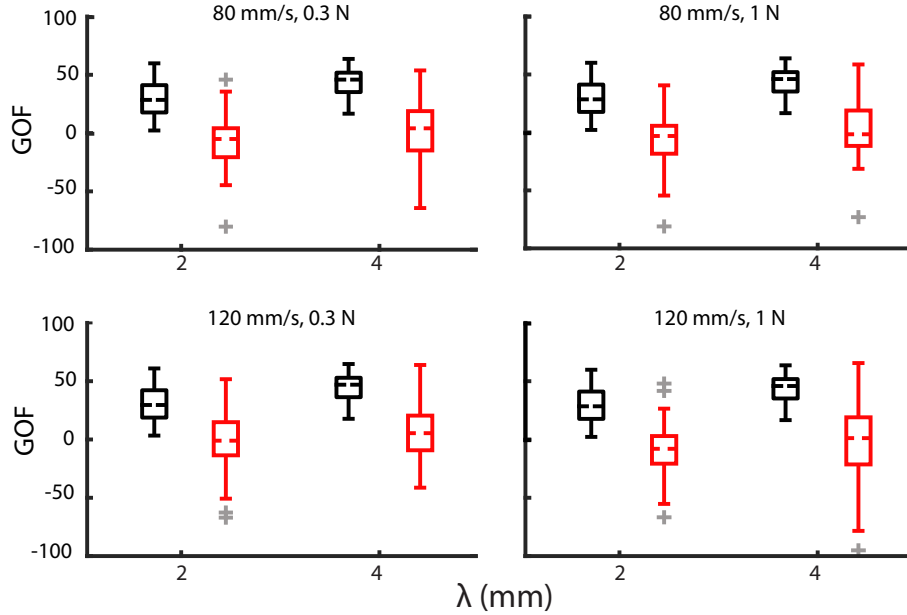
Figure 5.6: Goodness Of Fits (GOFs) summary computed in 40 trials per each wavelength and experimental conditions (λ,v_p,f_p). Each box plot delimits the region where 80 % of the samples lie, median values marked as dashed lines, outliers marked as gray crosses. NLARX model results in red, partial contact differential pressure model in black. The GOF increases with increasing λ. The partial contact differential pressure model produces better results.

We also compared the 320 correlation coefficients ρ to those obtained for the same measurements using NLARX models. Figure 5.7 shows a summary of ρ measured using both the NLARX approach and the partial contact differential pressure model. The correlation coefficients obtained using the partial contact differential pressure model were above 0.6 in more than 90% of the cases. The correlation coefficients obtained using NLARX models were below 0.5 in 60% of the cases, and in

some cases they even showed negative correlation. This held true irrespective of the normal force applied f_p and the average sliding speed v_p. Similarly to the GOFs, the correlation values are higher for forces measured over surfaces with larger wavelength, suggesting that the model is better suited for coarser surface features.

Figure 5.7: Correlation (ρ) summary of 40 trials per each wavelength and experimental conditions (λ, v_p, f_p). Each box plot delimits the region where 80 % of the samples lie, median values marked as dashed lines, outliers marked as gray crosses. NLARX model results in red, partial contact differential pressure model in black. The correlation ρ increases with increasing λ. The partial contact differential pressure model produces better results.

We also attempted to model frictional forces using a variation of the partial contact differential pressure model that excluded the saturating function. The parameters were tuned to obtain the lowest NRMSE, but this was harder to achieve compared to the case including the saturating function. Figure 5.8 shows the same measurements as Figure 5.5, but with the model estimates computed excluding the saturating function. This model is able to capture some of the trends seen in the measurements, although discrepancies can be seen, specially for $\lambda = 4$ mm. The GOFs decreased with the exclusion of the saturating function in most of the cases. Overall, the exclusion of the saturating function from our model resulted in a decreased qualitative and quantitative fits.

The parameters R_s, R_f and r (Fig. 5.2 B) represent the contact length of the surface of contact
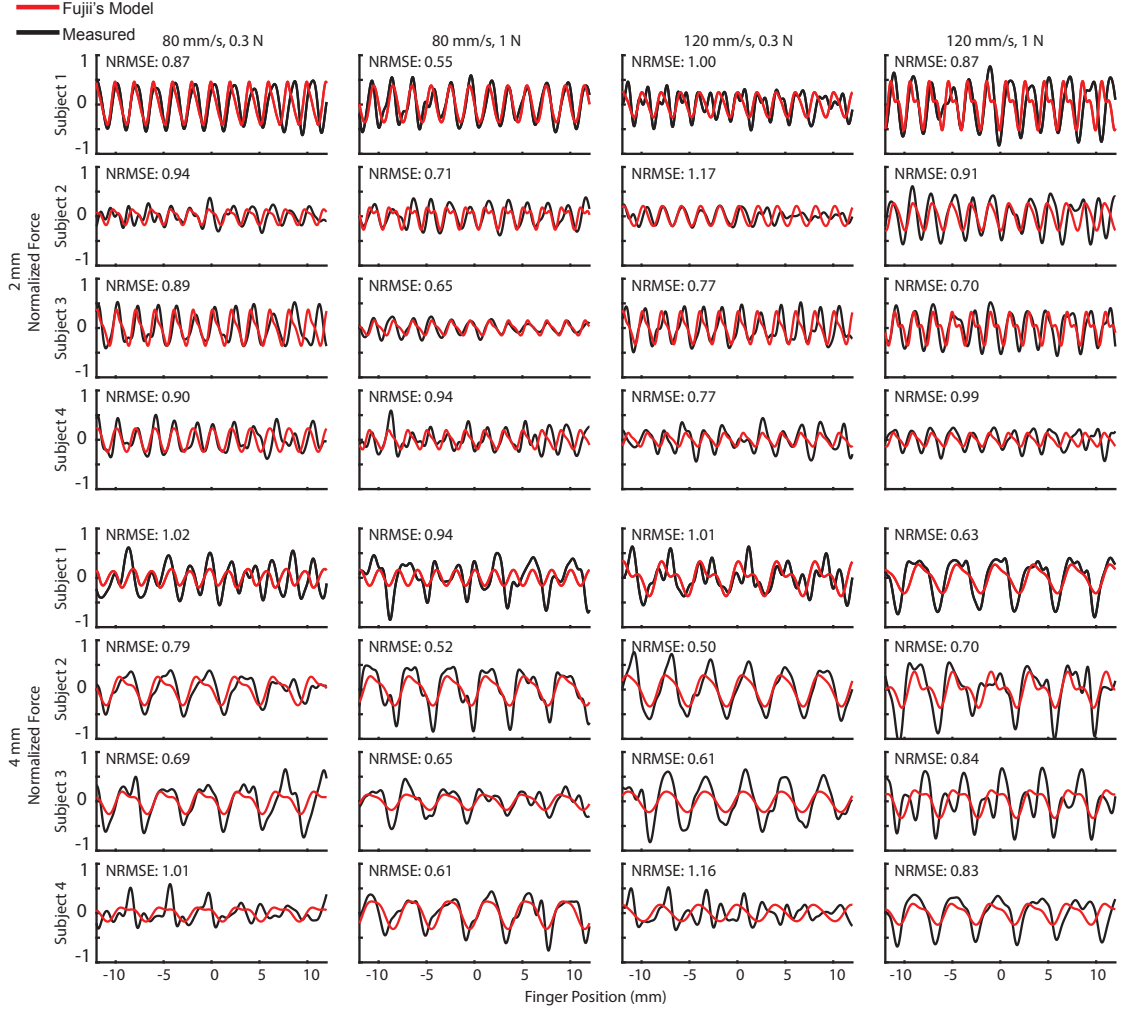
Figure 5.8: Typical F_T measurements and their corresponding force estimates using Fujii's model $\hat{F}_T$. Data displayed corresponds to frictional forces elicited by four subjects sliding their bare finger over two surfaces ($\lambda = 2$, 4 mm) under four measurement conditions (see Table 4.1). F_T measurements in black and their corresponding force estimates $\hat{F}_T$ in red. The Normalized Root Mean Squared Error (NRMSE) is indicated for each case.

and the pressure points of the model. The parameter values obtained for each trial remained in intervals consistent the scale of the surface touched by the finger, (i.e., all three parameters were less than $\lambda/2$). No particular trend was seen for any of the three parameters with respect to the four different conditions, although it was expected R_s to be larger for higher normal forces applied (See Figure 5.9).

The parameters h_{thr} obtained for each trial show a distribution over the range 0 - 0.1λ mm. In the the coarser surface, the applied normal force and the sliding speed seemed to have a noticeable effect on h_{thr}. Increasing speed resulted in an increase of h_{thr}, while increasing normal force resulted in a decrease of h_{thr}. This effect was not evident in the 2 mm surface.

The force estimate of the model $\hat{F}_T$ showed the highest sensitivity to changes in h_{thr}, meaning small changes in h_{thr} produced large changes in both amplitude and pattern of $\hat{F}_T$. On the other hand, the parameters R_s, R_f, r and μ caused smooth changes in the pattern of $\hat{F}_T$. Changes in both R_s and R_f caused almost negligible effects for given values of all the other parameters.

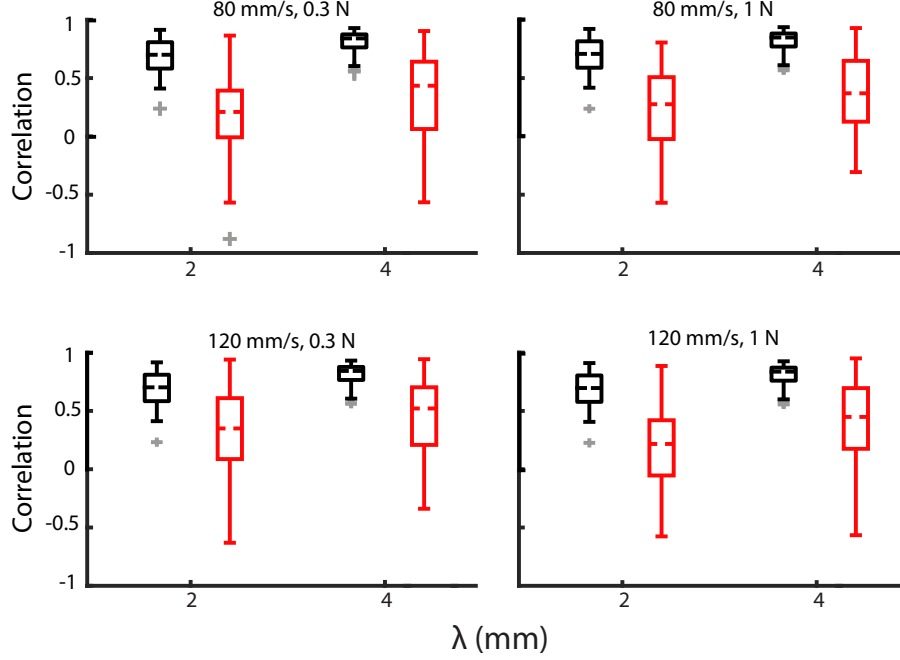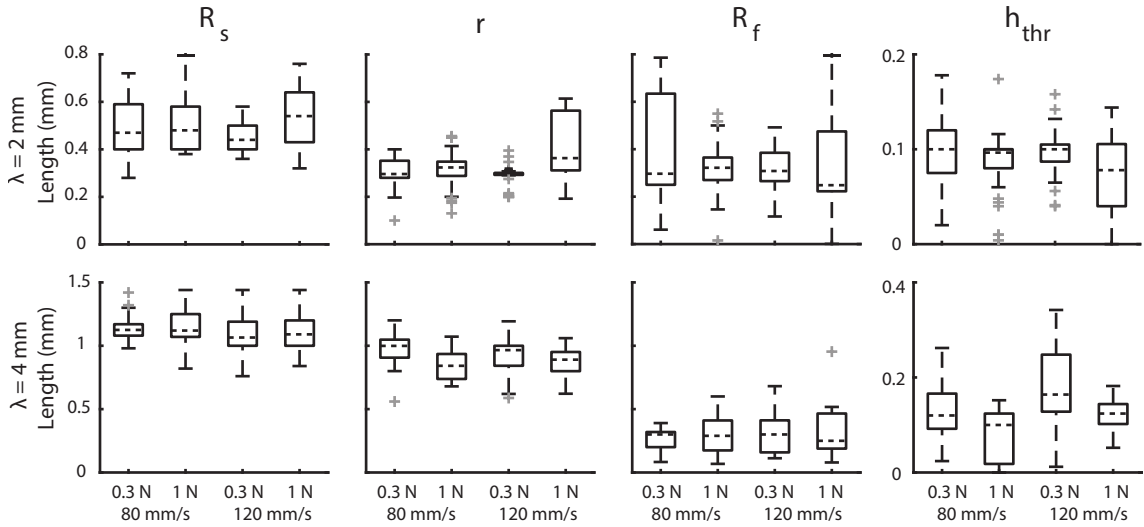**Figure 5.9:** Parameters R_s, R_f and r and h_{thr} summary of 40 trials per each wavelength and experimental conditions (λ, v_p, f_p). Each box plot delimits the region where 80 % of the samples lie, median values marked as dashed lines, outliers marked as gray crosses

5.5   Discussion

The partial contact differential pressure model proved to be effective to mimic our frictional force measurements corresponding to four different subjects sliding their fingers over two surfaces of different scale detail. The signals obtained capture the gross patterns of the measured frictional forces. The model presented here captured the frictional force patterns better on coarser surfaces. It is possible that some of the assumptions of the model, such as the assumption that a single contact area dominates the frictional force generation, become invalid at certain scales (i.e., they apply only for surfaces that are coarse enough). It is probable that the model is applicable on surfaces with high relief elements spaced 2 mm at least. We cannot issue a similar statement for surfaces with high relief elements spaced less than 2 mm apart.

The use of a explicit finger-surface contact model caused a significant improvement on the model prediction accuracy compared to that of the NLARX approach[2], yielding better qualitative and quantitative fits as illustrated in Figures 5.7 and 5.6.

We can also see the advantage of including the pre-input saturating function to the differential pressure model. Accounting for intermittent finger-surface contact this way facilitated the identification the model parameters. Moreover, the GOFs metrics were higher for the model including the saturating function, compared to the model without it (see Figures 5.5 and 5.8). Frictional forces were better modeled qualitatively and quantitatively by the inclusion of the saturating function in our approach.

The obtained parameters did not show a clear trend with respect to the normal force applied f_p or the average sliding speed v_p (Table 4.1). However, the threshold representing the minimum height of finger contact with the surface h_{thr} became smaller with higher applied normal forces, accounting for the finger making contact with lower parts of the surface. This effect indicates that the model may have captured the physical phenomenon of the fingertip tissue spreading over a larger area with increasing force.

The average sliding speed v_p had also demonstrated an effect. Higher speeds caused h_{thr} to

---

[2]This approach is described in detail in chapter 4

increase, accounting for a smaller contact region between the finger and the surface. This effect is likely to be caused by the subject attempting to reduce drag in order to achieve a higher sliding speed, resulting in a reduced contact region (i.e., higher h_{thr}). Also, when v_p is higher, the fingertip tissue has less time to "adapt" to the surface features, thus reducing the contact spread as the tissue "jumps" from one contact region to the next.

A more accurate modeling of the small scale variations effects in these surfaces, which yield complex contact conditions, would require a distributed contact model, rather than the single domain contact model applied here. Additionally, at small enough scales, the fingerprint ridges may also cause noticeable affects affecting frictional force generation. However, the partial contact differential pressure model proposed in this work proved capable of modeling the nearly regular fluctuations present in frictional force measurements of a bare finger sliding over regular undulating surfaces. While random fluctuations were present in the measurements, these were of comparative small scale for coarser surfaces.

5.6   Conclusion

A minimal mechanical model was developed to account for the biomechanical response of finger tissues and the geometry of contact with the finger. It uses a small number of parameters (R_s, R_f, r and h_{thr}) to account for the predominance of high relief features and for the elastic response of the finger tissues. The minimal model was realized from taking into account discontinuous contacts between the finger and a surface with high relief features, and a differential pressure model adapted to a single contact patch between the finger and surface. Hence, the model was obtained by scaling down the differential pressure model proposed by Fujii et al. [84], adding a pre-input saturating function, and post-output filtering.

The model parameters were tuned to obtain a model output similar to each slide trial in a subset of the data previously measured. The comparison between the minimal model outputs and the respective measurements exhibit high qualitative similarity, which was also quantified as measures of both correlation and GOF. These measures demonstrated the effectiveness of the proposed model to capture the gross pattern present in the frictional frictional forces studied.

The results obtained by this modeling showed the extent to which frictional forces are dependent on the discontinuity of the contact interface between the finger and the touched surface.

Chapter 6: Characterization of contact geometry and mechanics in frictional force production during tactile exploration of relief surfaces

The material in this chapter was submitted to Journal of The Royal Society Interface: M. Janko, M. Wiertlewski, Y. Visell, Local contact orientation predicts lateral forces felt during haptic exploration of relief surfaces

This chapter describes a numerical method to estimate the pressure changes inside the fingertip tissue under dynamic deformation. The estimate accounts for bulk frictional forces elicited upon sliding interaction with relief surfaces.

We sought to explain how geometry profile on the mesoscale of an object affects these frictional forces. This is a complex problem considering the viscoelastic nature of the finger and the variability of contact interaction parameters. For instance, a finger might be in contact with a surface at many discontinuous regions depending on both the stiffness of the finger and the profile of the surface touched. Also, these contact regions might be affected by how hard the finger presses on the surface and how fast the sliding of the finger over the surface occurs [136]. Hence, understanding how these small scale interactions occur and how they affect the resulting frictional forces is of interest to guide the development of predictive force models that may emulate frictional stimuli from surface specification.

Local surface descriptors, notably the slope of the surface at a contact point [3, 100, 137], have been proposed in order to account for the effect of surface shape on force production, but have not been applied to distributed contact with the finger pad, where the slope may vary within a single contact region, and may not be defined at locations where contact is broken.

In order to account for friction force production between the finger pad and non-flat surfaces, we measured forces and contact interfaces during frictional sliding on relief surfaces, using synchronized force measurements and a fronto-parallel high-speed video capture configuration. Using image processing methods, we tracked the geometry of contact interfaces from the high-speed video, and

used the resulting data to estimate parameters of a spatially distributed frictional model. As we show, this model, which accounts for surface shape and contact mechanical effects, could accurately predict forces that were felt during sliding on a variety of surfaces at different speeds.

6.1 Methods

We used the measurement apparatus described in Chapter 3 (using high speed video for fingertip tracking) to investigate contact interactions between a finger and an array of specified, machined relief surfaces, and analyzed the results in order to deduce the effect of interaction parameters, surface geometry, and skin mechanics on force production.

6.1.1 Measurement apparatus

The measurement apparatus described in Chapter 3 was used to collect force data and images of the fingertip of two human subjects sliding over flat surfaces with a relief feature in the middle (Figure 6.1). The sensing system using a high-speed camera for fingertip tracking was used for this experiment.
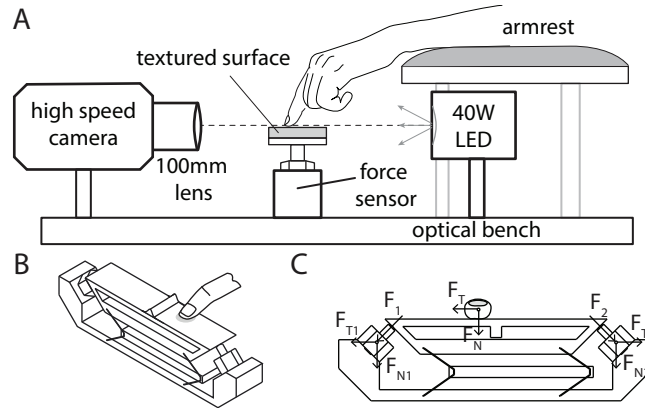
Figure 6.1: Experimental setup **A.** Side view of the measurement instruments used. The high speed camera, the force sensor and an LED light source were mounted on an optical bench ensuring they were aligned. **B.** Isometric view of the force sensor. **C.** Frontal view of the force measurement device with force decomposition.

6.1.2 Relief surfaces

We fabricated solid relief surfaces by machining rectangular (120 mm x 25 mm) aluminum plates with single, smoothed relief features. We modeled the samples parametrically and fabricated them

from 6061 aluminum alloy using Electrical Discharge Machining (EDM) yielding an artifact-free finish at the scales of interest. We included three types of relief features: bump, step up edge and step down edge, located at the center of flat surface samples, see Figure 6.2. Two widths were used, 2 mm and 4 mm, yielding a total of 6 surfaces. All shapes had a raised cosine profile, with heights A_s given by 20% of their widths W_s.
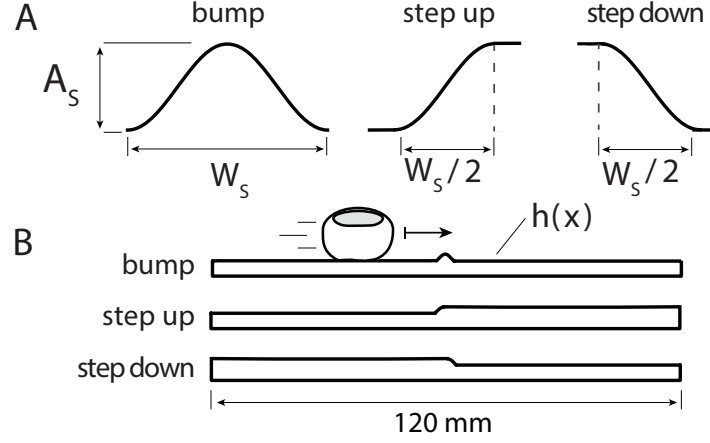
Figure 6.2: Surfaces used in the experiment. **A.** Surface center feature geometric specification. **B.** Front view of the surface used.

6.1.3 Experimental procedure

We captured video and force data as the fingertips of two participants (male, ages 29 and 35) slid their index finger on the surface samples (Figure 6.1 A and B) at one of three speeds (40 mm/s, 80 mm/s and 120 mm/s) for a total of 15 trials per surface. The normal force was prescribed to be 0.3 N. Participants were trained to produce this force level prior to the experiment, using a force sensor. An audio metronome aided them in maintaining one of three prescribed average sliding speeds in each trial. The fingers were cleaned with isopropyl alcohol before each recording trial. The surfaces were treated with small amount of talc to reduce stick-slip effects observed in pre-experimental trials.

6.1.4 Force data processing

The raw signals from the piezoelectric transducers were downsampled and filtered to match the video sampling period of 0.1 ms. The tangential force $F_T(t)$ was then computed from equation 3.1, and low-pass filtered using a zero-phase filter with 500 Hz cutoff frequency. Three zero-phase notch filters

centered around 50 Hz, 150 Hz and 300 Hz, were used to remove interference caused by the power supply. The piezoelectric sensors act as high pass filters with approximately 5 Hz cutoff frequency and therefore caused the force components to drift slightly during data collection. For each slide, lasting no more than 0.4 s, the drift could be approximated by a linear trend. We removed this artifact by computing the best linear fit to the force signal preceding the touch interaction with the middle feature, that contained only the drift, and subtracted it from the force measured during the touch interaction. Then the force signals were truncated to the time period corresponding to the finger sliding at a 26 mm window centered at the middle of the surface matching the location of the relief feature.

6.1.5   Image analysis

The high speed video data for each trial consisted of a sequence of grayscale images – video frames sampled in time. Each video frame had a resolution of 1280x720 pixels. They which were cropped after recording to the center 1260x360 pixels to remove unwanted background and then were converted to binary images by using a threshold operation. Each pixel in the resulting binary images represented either background illumination (1) or shade from the finger and/or surface profile (0).

We processed the binary images in order to extract outlines of the finger and surface profile, by using the Moore-Neighbor tracing image boundary detection algorithm modified by Jacob's stopping criteria [138], implemented in the image processing toolbox v10.0 included in Matlab R2017a (Matlab Software, The Mathworks Inc., Natick, MA). We extracted curves that delineated the contours representing the fingertip, surface, and contact interface between them.

The surface profile contour was defined as a geometric curve $\hat{h}$ which was extracted from the first frame of the video which contained only the surface profile shade. We determined the size of one pixel in the image plane from both the maximum height $\hat{h}_0$ in pixels, of the observed shape $\hat{h}$ and the known height of the surface A_s expressed in mm, leading to a precise calibration of the spatial dimensions, see Fig. 6.3A.
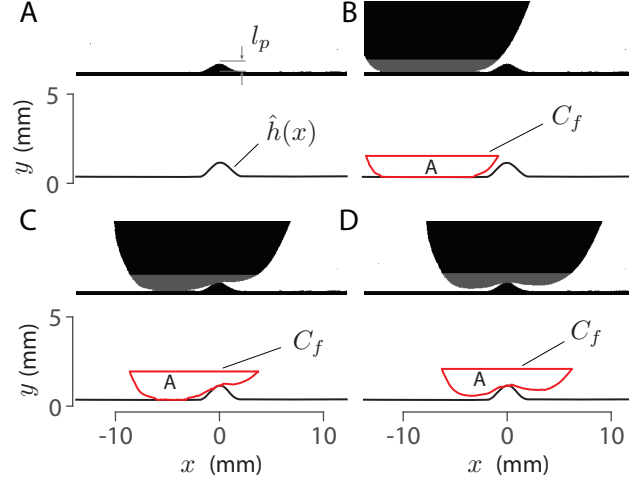
Figure 6.3: Example of image analysis (4 mm Sinusoidal Bump). **A.** First frame of the video sequence, used to adjust length scale and isolate the surface used. **B.** First frame containing the fingertip area of interest (in gray). **C & D.** Frames showing the finger in contact with the bump (deformation occurs). C_f is adjusted to enclose the area of interest A.

6.1.6 Fingertip position estimation

The first video frame in which the horizontal extension of the fingertip appears entirely in a frame (Fig. 6.3B) was used as a reference to obtain an estimate of the area enclosed by the fingertip contour. This occurred while the finger is in the flat part of the surface, and little net tissue deformation was present.

To aid the tracking of finger contours, we modeled the tissue as approximately incompressible, so that a deformation caused by the interaction with the surface profile caused the tissue to be displaced to other regions. To estimate the fingertip position we first computed the area A (Fig. 6.3 B) enclosed by the fingertip contour while the fingertip was entirely in the flat part of the surface and intersected by a horizontal line located 0.4 mm above the maximum height of the surface feature. For each subsequent frame, the region of interest from the fingertip was defined as a closed geometric curve C_f resulting from the intersection between the fingertip contour and an horizontal line ensuring the area enclosed is equal to A (Fig. 6.3 C & D). The position $x(t)$ of the fingertip was estimated as the x coordinate of the centroid of the area enclosed by C_f of every video frame.

The estimates of fingertip position $x(t)$ were used to infer spatial patterns of the temporal signals,
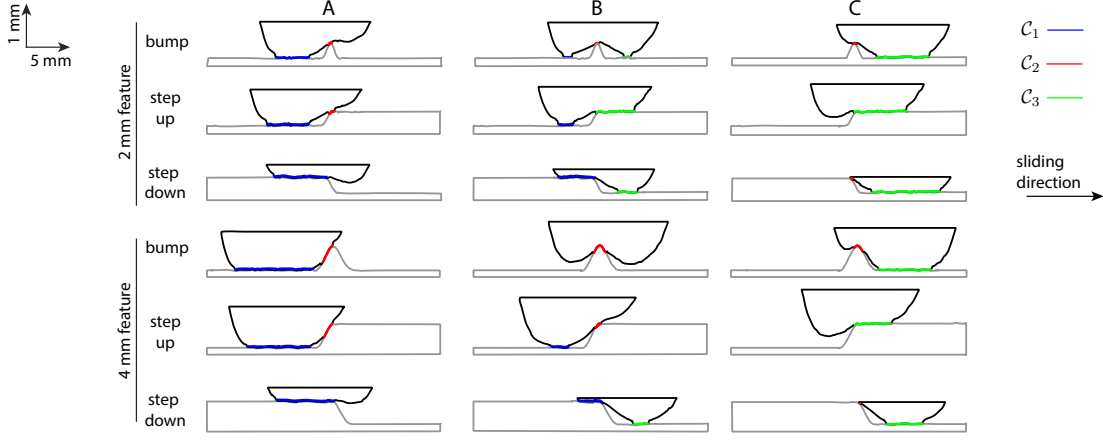
Figure 6.4: Examples of finger sliding over the six surfaces used. Contact areas between the fingertip and the surface are illustrated for 3 different contact situations. **A.** Initial finger contact with the relief feature. **B.** Finger on top of the relief feature. **C.** Finger about to leave the region of the relief feature.

using the same procedure employed in our prior work [2, 139], associating the force F_T to the position x at the corresponding time t. We sampled the spatial domain with a resolution of 0.01 mm.

6.1.7 Region of contact between the finger and the surface

Within a given frame, the region of interfacial contact $\mathcal{R}$ between the fingertip and the surface was estimated from the contours of the finger, C_f, and the surface, $\hat{h}$. For the purpose of determining the contact interface, a pair of points separated by a distance of 3 pixels or less was considered to be in close contact.

We divided the region of interfacial contact $\mathcal{R}$ into contact contours $\mathcal{C}_i$ based on three surface regions: (1) the flat (curvature zero) region before the curved region, or feature, at the middle of the surface, (2) the non-flat (curved) region at the middle of the surface, and (3) the flat region to the right of the middle feature. This analysis divided the contact interface $\mathcal{R}$ into up to three non-overlapping contact contours $\mathcal{C}_i$ within each frame.

We also computed the length L_i of each contact contour $\mathcal{C}_i$ in each frame, in order to characterize how it evolved during sliding.
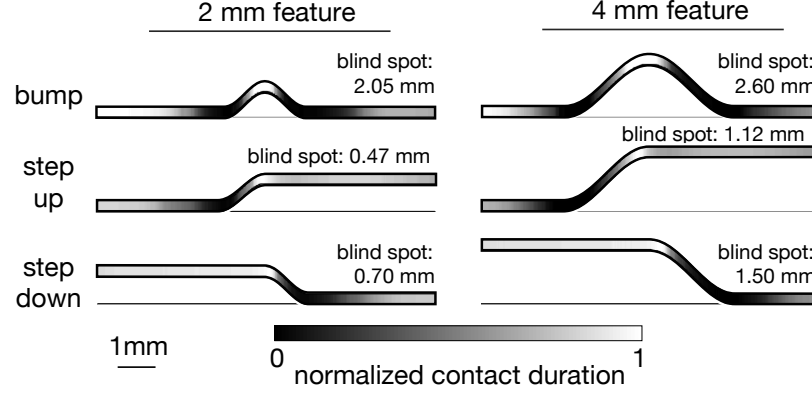
Figure 6.5: Normalized proportion of time of contact between the finger and surface locations (both subjects, all trials). At the highest level on the scale (1, white), the finger was in contact with the surface for the highest proportion of time, while at the lowest level on the scale (0, black), the surface was never contacted by the finger. In each trial, finite width regions of every surface satisfied this last condition; we refer to them as "tactile blind spots". Their widths ranged from 0.47 mm (Step Up surface, 2 mm scale) to 2.6 mm (Bump surface, 4 mm scale).

6.2   Experimental results

The evolution of the contact contours $\mathcal{C}_i$ in each slide were consistent across trials, meaning the finger starts with a single contact contour ($\mathcal{C}_1$) in the first flat region of the surface, then multiple contact contours appear (see Fig. 6.4). The number and shape of the subsequent contacts depend on the surface relief feature. In all cases, the deformation of the finger occurred with a limited curvature. Therefore, disconnection with the surface occurs and the contact is broken into multiple instances. As a consequence, the finger does not make contact at every point with the bottom part of the bumps or edges. These depressed regions remained "hidden" from touch as shown in Fig. 6.5 which represent the normalize proportion of contact of the surface with the finger. We refer these "hidden" regions as "tactile blind spots" which exist in every surface used in this study, with widths ranging from 0.47 mm (step up, 2 mm) to 2.6 mm (bump, 4mm).

In the case of the 2 mm and 4 mm bumps, the contact conditions differ significantly when the finger is on top of the bump. It can be seen that the finger makes contact with up to 3 contact regions at a given time on the 2 mm bump (Fig. 6.4 B), whereas in the 4 mm sample the finger is only in contact with at most two regions at a given time, this held true for all slides measured in

Table 6.1: Pearson's correlation coefficients (ρ) between F_T and $\hat{F}_T$ for a first order approximation of σ

| | Subject 1 | | | | | | Subject 2 | | | | | |
| | 2 mm | | | 4 mm | | | 2 mm | | | 4 mm | | |
	Bump	Step Up	Step Down	Bump	Step Up	Step Down	Bump	Step Up	Step Down	Bump	Step Up	Step Down
$\overline{\rho}$	0.81	0.81	0.41	0.80	0.91	0.60	0.93	0.89	0.66	0.81	0.89	0.50
std(ρ)	0.17	0.25	0.27	0.18	0.05	0.23	0.02	0.08	0.22	0.12	0.13	0.25

| | All Subjects | | | | | |
| | 2 mm | | | 4 mm | | |
	Bump	Step Up	Step Down	Bump	Step Up	Step Down
$\overline{\rho}$	0.87	0.85	0.53	0.81	0.90	0.55
std(ρ)	0.13	0.19	0.27	0.15	0.10	0.24

Table 6.2: Side contact length L_i metrics (refer to Fig. 6.6)

| | Subject 1 | | | | | | Subject 2 | | | | | |
| | 2 mm | | | 4 mm | | | 2 mm | | | 4 mm | | |
	Bump	Step Up	Step Down	Bump	Step Up	Step Down	Bump	Step Up	Step Down	Bump	Step Up	Step Down
Avg. L_1 decrease slope	-1.22	-1.34	-0.96	-1.84	-1.96	-0.87	-1.13	-1.50	-0.87	-1.61	-1.96	-0.84
Avg. L_2 width (mm)	11.0	9.40	9.67	12.8	9.93	10.2	12.0	9.47	9.27	13.7	10.6	10.1
Avg. L_3 increase slope	1.41	0.99	1.55	2.20	1.01	2.25	1.22	0.95	1.80	1.61	0.95	2.25

this study.

The contact contours observed were either horizontal lines (regions of the finger in contact with the flat parts of the surface) or curves approximating the shape of the relief feature of the surface. In any case, the length of the contact contours across different prescribed speeds showed similar trends, with similar decrease (or increase) rates on the flat parts of the surfaces (L_1 and L_3) for a given subject and surface. However, these rates are affected by subject and surface (See table 6.2, 1st and 3rd rows). L_1 ranges from -0.84 to -1.96 and L_3 ranges from 0.95 to 2.25. The magnitude of L_1 higher to that of L_3 in all step up surfaces, while the opposite is true for step down and bump surfaces. The width of the surface region at which L_2 is non-zero (See table 6.2, 2nd row) is consistently higher for bump surfaces, while step down and step down surfaces show similar values.

The contact contour length on the relief feature L_2 remained quasi-constant in all cases, specially in the cases of the bump surfaces (See Fig. 6.6). Although, it is clear the finger tissue in contact with these features is not the same at each instant.
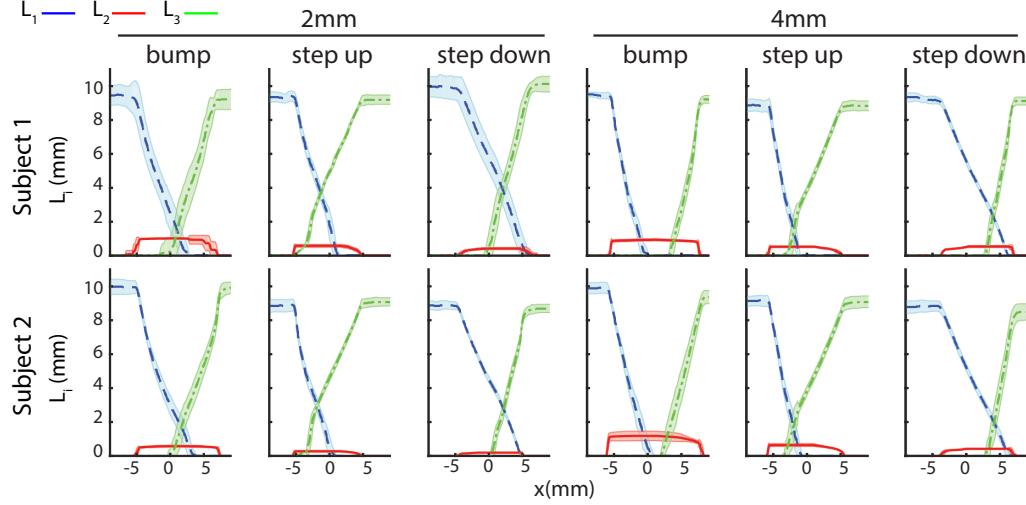
Figure 6.6: Side contact lengths as a function of the fingertip position. Mean of 15 trials L_1 in dashed green, Mean of 15 trials L_2 in dashed red and Mean of 15 trials L_1 in dashed blue. Shaded regions: 1 standard deviation.

The force patterns from both subjects showed similarities in the course over the range of sliding, with minor differences, probably attributed to the physical difference between the tissues of both subjects' fingertips and their sizes.

The forces F_T measured over bumps and step up increased sharply when the finger made contact with the relief feature (i.e. $\mathcal{C}_2$ appears), indicating a change in the contact pressure caused by the feature of the surface with slope $\alpha(x) > 0$. An opposite effect was present on forces measured over step down surfaces, but with a progressive change in force.

The spatial patterns observed in the tangential forces $F_T(x)$ when measured over surfaces of different shapes and scales showed consistent trends regardless of the sliding speed, these patterns showed mostly inter-trial amplitude variability (Fig. 6.7). Hence, data were grouped by surface and subject irrespective of the sliding speed for further analysis. The data set consisted in a total of 180 $F_T(x)$ measurements (2 subjects, 6 surfaces, 15 slides per surface per subject).

6.3   Frictional force model

We sought to model the frictional forces we measured as a function of the surface profiles. Previous modeling and rendering efforts for frictional force generation from surface profile used the slope of
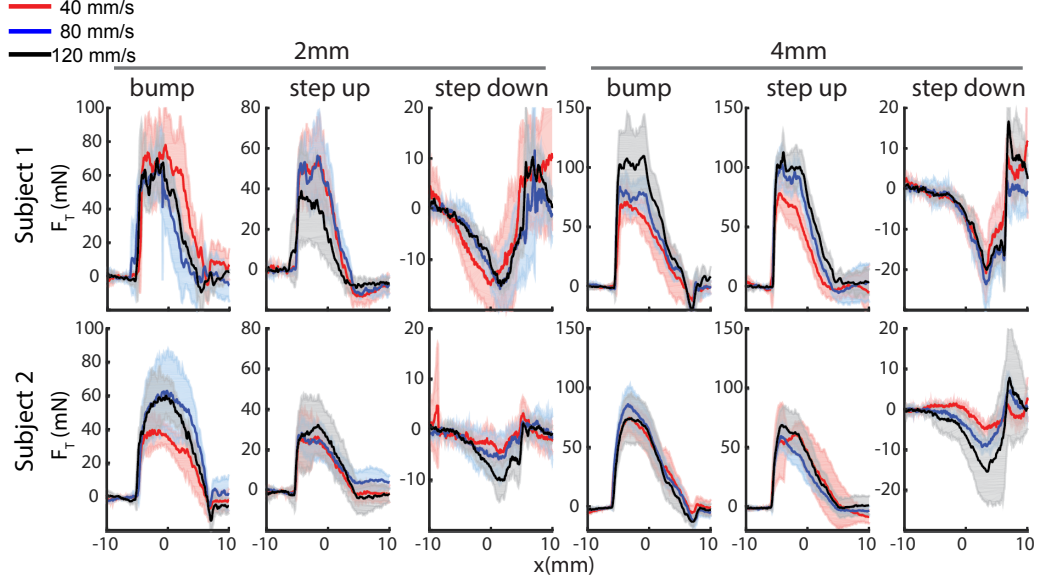
Figure 6.7: Measured forces $F_T(x)$ grouped by surface and subject (15 trials per case). Mean of 5 trials at 40 mm/s in red, mean of 5 slides at 80 mm/s in Blue and mean of 5 trials at 120 mm/s in Black. Shaded regions: 1 standard deviation.

the surface as an input [3, 84, 140, 141]. Qualitatively, the surface attribute mostly correlated to the frictional force patterns we measured was the slope $h'(x)$. Hence, we hypothesized the contact pressure is a function of the slope of the contact region between the fingertip and a solid object during sliding touch. In this case, the contact pressure causes a stress $\sigma_p(x)$ normal to the surface of the hard object. We then formulate:

$$\sigma_p(x) = f(h'(x)) \tag{6.1}$$

Where $f(\cdot)$ is an unknown function and $h'(x)$ is the slope of the surfaces used in this study defined for bump; step up; and step down (Eq. 6.2).

$$h'(x) = \begin{cases} & x < \frac{W_s}{2} & \text{Bump} \\ -0.2\pi \sin(\frac{2\pi}{W_s}x) & \frac{-W_s}{2} < x < 0 & \text{Step up} \\ & 0 < x < \frac{W_s}{2} & \text{Step down} \\ 0 & & otherwise \end{cases} \quad (6.2)$$

Since we don't know the exact form the function $f(h'(x))$ takes, we seek to estimate its value in a short interval. Hence, we sought to fit a polynomial function for $f(h'(x))$. Thus, we can re-write Eq. 6.1 as:

$$\sigma_p = f(h'(x)) \approx \sum_{n=0}^{N} p_n h'(x)^n \quad (6.3)$$

Where N is the order of the polynomial approximation and p_n are the coefficients of the polynomial which are to be determined.

If we assume a local Coulomb friction law in each point of contact, the normal stress $\sigma_p(x)$ and the tangential stress $\sigma_r(x)$ are related by:

$$\sigma_r(x) = \mu\sigma_p(x) \quad (6.4)$$

Finally, to obtain an estimate $\hat{F}_T(x)$ of the tangential force $F_T(x)$, we can integrate the projections of $\sigma_p(x)$ and $\sigma_r(x)$ onto the x axis (Refer to Fig. 6.8) over the surface area of the region of contact (Eq. 6.5).

For simplicity we assumed the contact surface between the finger pad and the surface at each region has approximately a rectangular shape. The side of the contact square can be estimated from the length L_i of the contact region $\mathcal{C}_i$ extracted from the image analysis explained in section 6.1.7 and a fixed width L_{max} which we estimated from the data as the maximum L_i measured in each
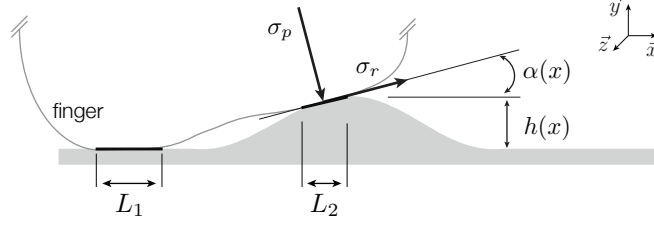
Figure 6.8: Side view of contact between finger and surface. Definition of surface stresses σ_p and σ_r and their relation to the tangential direction depending on $\alpha(x)$ at a position x and height $h(x)$.

slide.

$$
\begin{aligned}
\hat{F}_T(x) &= \int_{\mathcal{R}} [\sin(\alpha(x))\sigma_p(x) + \cos(\alpha(x))\sigma_r(x)]dxdy \\
&= L_{max} \sum_i \int_{\mathcal{C}_i} \sigma_p(x)[\sin(\alpha(x)) + \mu\cos(\alpha(x))]dx
\end{aligned}
\tag{6.5}
$$

Where $\alpha(x)$ is the slope angle at a point x over the surface.

Therefore, substituting (6.3) into (6.5) the frictional force can be computed as a function of the contact slope $h'(x)$ by:

$$
\hat{F}_T \approx \sum_{i=1}^{3} \sum_{n=0}^{N} p_n \int_{\mathcal{C}_i} h'(x)^n \left\{ \sin(\alpha(x)) + \mu\cos(\alpha(x)) \right\} dx
\tag{6.6}
$$

Finally, each signal $\hat{F}_T(x)$ was filtered using a median filter with a sliding window of 2 mm, this was necessary to mitigate an artifact present upon appearance of contact region $\mathcal{C}_2$ caused by light scattering.

We estimated the parameters p_n and computed the frictional force estimates for each fingertip slide using the contact contours $\mathcal{C}_i$ converted to spatial domain and their respective slope angles $\alpha(x)$. The friction coefficient μ was estimated from the data for each subject[1].

The parameters p_n were obtained using the simplex direct search method of Lagarias et al. [142] (fminsearch, Matlab Software, The Mathworks Inc., Natick,MA) aiming to minimize the normalized

---

[1]A grid search was conducted using values of μ between 0.4 and 0.7, the values that minimized the average normalized mean square error $\bar{\epsilon}(F_T, \hat{F}_T)$ were chosen for each subject.

mean square error $\epsilon(F_T, \hat{F}_T)$ (Eq. 6.7) between the measured force F_T and the model estimates $\hat{F}_T$ for each of the 15 $(F_T, \hat{F}_T)$ pairs obtained per subject and surface.

$$\epsilon(F_T, \hat{F}_T) = \frac{\|\hat{F}_T - F_T\|}{\|\hat{F}_T - \overline{\hat{F}_T}\|}, \qquad \overline{\hat{F}_T} = \frac{1}{L} \sum_{x=1}^{L} \hat{F}_T(x) \tag{6.7}$$

To quantify the similarity of $\hat{F}_T$ to F_T, we computed the Pearson's correlation coefficient ρ (Eq. 5.9), for every one of the 180 pairs $(F_T, \hat{F}_T)$.

6.4 Model results

The frictional forces F_T measured were compared to the tangential force estimates $\hat{F}_T$ we computed according to the proposed model. We considered five different polynomial order approximations for σ (0th to 4th) and fixed the value of μ for subject 1 and subject 2 to 0.6 and 0.5 respectively. We computed the statistics on the NRMSE (ϵ) computed for each pair $(F_T, \hat{F}_T)$ and used them to assess the goodness of each order approximation (Fig.6.10). The median NRMSE was monotone decreasing for increasing polynomial approximation order and ranged from 1.27 using the 0th order approximation to 0.46 using the 4th order approximation. Nevertheless, we chose the 1st order approximation for further analysis (with a median of 0.52) since the difference in median ϵ between the 1st and 4th order approximations was only 12%. Hence, increasing the complexity of the model did not justify the gain in fit accuracy. The first order approximation (i.e. an affine relation) minimized ϵ to a degree comparable to higher order approximations.

Using the first order polynomial approximation for σ_p, the model captured the gross patterns of frictional force production with low median ϵ. The minimum and maximum ϵ were 0.23 and 1.15 respectively (excluding outliers). The estimates $\hat{F}_T$ mimicked the measurements both qualitatively (Fig. 6.9) and quantitatively (Table 6.1). The average correlation coefficients between $\hat{F}_T$ and F_T ($\overline{\rho}$) ranged from 0.53 on the 2 mm step down surface to 0.9 on the 4 mm step up surface, considering both subjects. These metrics were comparatively low for the step down surfaces, and they were high for step up and bump surfaces, irrespective of the surface scale and subject.
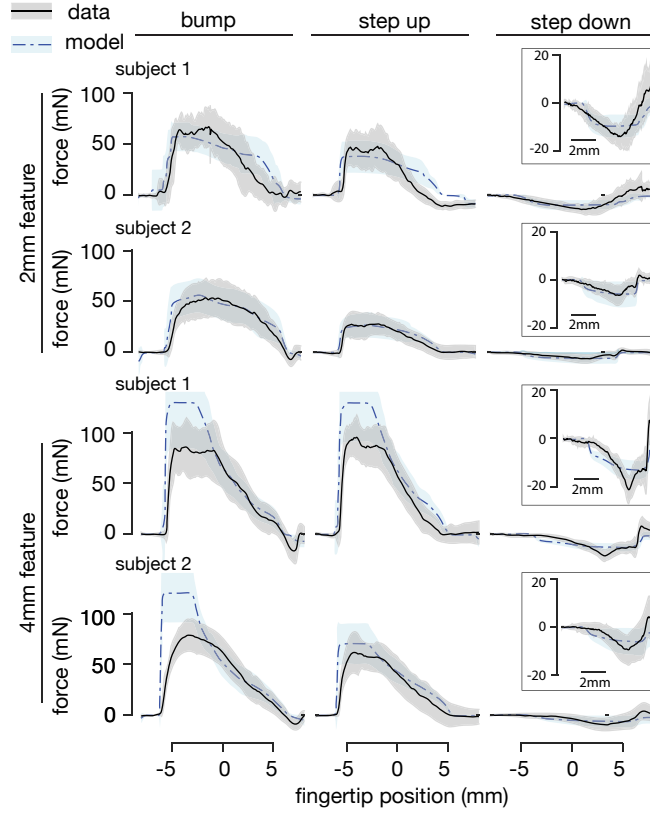
Figure 6.9: Comparing measured and modeled frictional forces. Measured forces $\hat{F}_T(x)$, mean of 15 trials in each condition (black). Model estimates $\hat{F}_T(x)$, mean of 15 trials in each condition (blue). Shaded regions: 1 standard deviation. Inset provides further detail on the step down data.
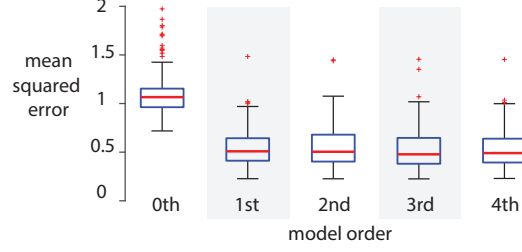
Figure 6.10: Errors $\epsilon(F_T, \hat{F}_T)$ in the model force predictions vs. model order. Each subplot represents 180 values (90 for each subject).

The offset parameters p_0 estimated in this study are very small (close to zero) since the DC component from the force measurements was eliminated. In reality these parameters should account for the DC friction between the fingertip and the flat part of the surfaces.

6.5 Discussion

As observed in this work, during the frictional sliding of a finger on non-flat relief surfaces, forces vary greatly from one sliding interaction to the next (Fig. 6.7), with patterns that do not bear an obvious relation to the surface geometry. This is consistent with previous measurements of of sliding contact forces between a fingertip and high relief features in sinusoidal gratings [60] or braille dots [126]. The spatial patterns of the forces that we observed varied systematically with the shape of the surface, and to a lesser degree with the speed of sliding.

By tracking the surface of contact between finger and surface using high speed video, we observed that multiple regions of connection between finger and surface develop near high relief features, due to the stiffness of the finger tissues. This always yielded multiple contact regions separated by local regions of disconnection (Fig. 6.4). The length of these contact surfaces evolved as the finger slid over the surface feature, and the trajectories of contact were highly stereotyped, varying little qualitatively from trial to trial (Fig. 6.6), despite large variations in speed (40 mm/s to 120 mm/s), and despite the larger qualitative, trial-to-trial variations of sliding friction forces. During contact with surface features, the maximum length spanned by the contact region was consistent from trial to trial, and during contact with high-relief bump features, the contact length was nearly constant within each trial. The scale of spatial variation was considerably larger than the surface features

themselves, due to the extended nature of the finger.

Disconnections occurred between the surface and finger as the latter spanned low relief or concave regions. Despite the modest curvature of the surfaces used in these experiments, there were regions of every surface that were never contacted by the finger of either subject (Fig. 6.5). These regions were approximately as large as the surface features themselves. We refer to these as "tactile blind spots", because they represented surface regions that were not felt by the finger.

Frictional forces also varied systematically during the experiments. The surfaces involved varied in shape and scale. The higher, 4 mm, surfaces elicited larger frictional forces than the 2 mm surfaces did. The qualitative spatial pattern of the frictional force varied greatly with the surface shape, and less prominently with the speed of exploration. The trial to trial variations were large, with standard deviations that reached 50% or more of the maximum force magnitude (Fig. 6.7). Forces produced during sliding on the step-down surfaces were small, typically only 10% to 30% as large in magnitude as the bump or the step-up surfaces, which were geometrically identical, but reversed in spatial orientation. This difference can be attributed to the increased stress on the finger as it slid across the relief features, which elicited much larger tissue deformations and contact surface areas, and commensurately higher adhesion and deformation forces. Consistent with our observations, steeper, higher slope features elicited larger deformations in the finger tissues, and gave rise to larger forces as the finger traversed these features. This force decreases slowly after most of the finger passed through the high relief feature, and returns to a nominal value after the contact was confined to the macroscopically flat region.

The tracked contact information and force data provided the information that we used in order to model the geometric and mechanical origin of these forces, using a friction model (Eq. 6.6) that depends on the distributed geometry of finger-surface contact, the mechanics of the finger tissues, in which the contact pressure was proportional to the slope $h'(x)$ of the surface, and a static (Coulomb) model of local friction. The resulting spatial patterns of forces qualitatively and quantitatively agreed with the measurements for all surfaces, conditions, and subjects examined (Fig. 6.9). Despite the large variations in forces, the correlation ρ between model predictions and

measured forces averaged 0.753 including all conditions, indicating that the main effect of surface topography on force production was captured by our model. The forces were lowest for the step down surfaces, which yielded small forces and high variations.

6.6   Conclusion

Touching a non-flat surface yields complex frictional forces that fluctuate greatly and whose patterns bear no simple relation to the surface topography or to specific features on it. It has been heretofore unclear what features of the bulk or interfacial mechanics of the finger that they may reflect, or how the perceptual system can make use of this information. To clarify the origin of forces produced during the exploration of such surfaces with a bare finger, we measured forces and contact interfaces, via synchronized force measurements and a fronto-parallel high-speed video capture system. We tracked the geometry of contact interfaces with image processing methods, and found that these contacts were consistently organized according to piecewise continuous segments of finger surface contact independent of the speed of exploration. The analysis revealed local regions of disconnection between the finger and surface that developed in concave regions near high relief surface features. The forces fluctuated greatly from trial to trial, and revealed spatial patterns of variation at length scales considerably larger than the surface features themselves.

We combined the contact geometry and force data in order to estimate the parameters of a spatially distributed frictional model that accounted for the local geometry of contact, contact stresses, and adhesion. This model – the first of its kind – proved capable of accurately predicting dynamical forces that were felt during sliding on a variety of relief surfaces at different speeds. It related the local surface geometry – orientation or slope – to the spatial pattern of forces that result. Such a model is highly relevant to the simulation of haptic experiences, especially via the emerging category of surface haptic displays that make it possible to dynamically program frictional forces [112, 113]. Existing simulation methods are based on measuring forces, or on generating arbitrary force patterns, and cannot predict forces that would be felt by the finger based on surface specifications alone.

The sliding finger obtains an incomplete sampling of the surface, in which some regions of the

object are "hidden" to the sense of touch. Nonetheless, the perceptual impression is of exploring a continuous, unbroken relief surface. Indeed, individuals have little difficulty perceptually discriminating surfaces like those investigated here [3, 143], or sinusoidal gratings with similar spatial scales [2, 53]. Evidently, the perceptual system completes the missing information for regions where the finger has lost contact, and for which no sensory information is available. In contrast, the highest, most convex, features were always contacted by the finger, and the contact lengths with such regions remained largely invariant between trials. Prior studies have reported that the tactile perception of textured surfaces are highly correlated with the dimensions [39, 40] and friction [42] of high relief features.

Chapter 7: Conclusions and future work

This dissertation addresses a gap in the current understanding of haptic interactions, and provides related information and models. These can be useful in the engineering of electronic haptic interfaces for reproducing realistic touch sensations. The study addresses the difficulty of modeling frictional forces during bare finger interactions with solid textured objects. We seek to characterize how frictional forces felt by the finger are affected by the shape and texture of a surface.

A new sensing system was developed to measure motion and forces felt by a bare finger, together with a characterization of the frictional forces produced by a bare finger sliding over both undulating and localized feature surfaces. Predictive biomechanically-inspired models for estimating frictional forces from surface geometry specification were proposed and validated using measurements obtained from bare finger interactions with various surfaces.

7.1 Engineering systems for measuring touch contact interactions

The research described in chapter 3 presented the design and development of two new sensing systems, consisting of custom force and optical sensors with high spatial and temporal precision. These sensing systems were used for capturing motion and forces felt by a finger during tactile exploration of textured surfaces. The force sensing device allows measurement of forces over a range of frequencies between 15-500 Hz, with a precision of approximately 50 μN. The optical tracking methods allow non-invasive measurement of fingertip position with resolutions and sampling period depending on the method used. The motion capture system had a resolution of 0.2 mm with a sampling period of 8.3 ms. The system used with the high-speed camera allowed measurements with a resolution of approximately 0.02 mm with an update period of 1 ms. These sensing systems allowed measurement of frictional forces, fingertip position and skin deformation of a bare finger sliding over exchangeable textured surfaces. They make it possible to collect empirical data about the mechanics of tactile exploration.

7.2 Modeling the dynamics of finger-surface interactions

Chapter 4 investigates frictional forces felt by a bare finger in sliding contact with an undulating sinusoidal surface. It studies how the spatio-temporal patterns of these forces depend on properties of the surface and contact interaction. Methods and instrumentation developed for motion capture and fingertip tracking were used to measure accurately time- and position- dependent contact forces between a finger in sliding contact with textured surfaces, which were precisely fabricated for this study. Methods for improving the spatial alignment between successive measurements and mitigating normal force modulation were presented and validated. The effects of the scale of the surfaces touched on the frictional forces measured were quantified in terms of harmonic distortion and variance to power ratio. Both measures showed an inverse proportional relation to the scale of the surface touched. In addition, an attempt was made to account for frictional force production exclusively from surface geometric specification using non-linear auto regressive exogenous models. This approach was insufficient to capture the dynamics of frictional force production, suggesting the need to include physical characteristics of the fingertip in the predictive models in order to account for the frictional forces observed.

In chapter 5, a minimal mechanical model was developed to account for the biomechanical response of fingertip tissues and the geometry of contact with the fingertip. The model uses a small number of parameters to account for the discrete and localized contact between the finger and surface, and for the elastic response of the finger tissues. The minimal model was realized from the observation that contacts between the finger and a surface with high relief features are discontinuous. This motivated the use of a saturating non-linearity in combination with the existing biomechanical model of finger contact proposed by Fujii et al. [84]. This model captured the differential response of finger tissues during contact with a surface.

The comparison between the model outputs and measurements indicated high qualitative and quantitative similarity, based on high correlation and goodness of fit values. These indicate the effectiveness of the model in capturing the main attributes of the frictional frictional forces. The

frictional forces were shown to be dependent on the discontinuity of the contact interface between the finger and the touched surface.

In chapter 6, we presented a biomechanically-inspired model for the production of frictional forces by a bare finger sliding over flat surfaces with isolated bumps and edges. Measurements of fingertip skin deformation provided additional evidence of discontinuity of the contact interface, leaving zones of the surface that were never touched by the finger. Furthermore, it was found that the relative contact orientation of the contact interface (between the fingertip and the surface) can be used to account for frictional force production of a bare finger sliding over surfaces with edge-like features. These findings revealed the dependency of fingertip skin deformation on the high relief features of a touched surface during sliding bare finger touch. The model proposed was able to mimic the most noticeable attributes of the frictional force measurements, using surface specification as input, assuming the biomechanical characteristics of the fingertip tissue are known.

7.3 Future work

This thesis presented contributions to instrumentation, measurement, analysis, and modeling of contact force production during tactile exploration. Despite the promising nature of these results, there are several areas deserving further research.

The sensing methods used in this work provided new insight into the dynamics of force production during bare finger sliding touch over customized surfaces of various shapes. Nonetheless, certain limitations in these devices prevent a full accounting of static (DC) forces exerted by the finger which could affect the frictional forces seen, as well as the patterns in skin deformation. The optical fingertip position measurement methods provided information about fingertip motion and skin deformation. However, these measurements were only performed as a 2D representation of the fingertip undergoing motion and did not capture 3D spatially distributed patterns of fingertip tissue undergoing deformation. Further studies of skin deformation dynamics and the corresponding frictional forces would benefit from measurements of the contact geometry in the region under the finger pad and measurements of spatially distributed forces (or stress) on the surface of contact.

The models presented in this dissertation depend on the skin deformation profile to account for

the resulting bulk forces. Nevertheless, the relation between the surface geometry and the observed skin deformation pattern was not explicitly accounted for and, to date, there is no available model that can produce a description of the skin deformation pattern during active sliding touch.

Mechanical characteristics of the fingertip such as mass, stiffness and viscosity were not explicitly accounted for in our models. Future work in this area would benefit from explicitly modeling fingertip skin deformation from mechanical attributes of the fingertip such as mass, stiffness, viscosity and initial shape. Obtaining this enhanced model would also enable modeling of bulk frictional forces exclusively from surface geometric specification.

The surfaces used as test input for our models were relief surfaces that consisted of one dimensional (1D) variations in height imposed upon macroscopically flat surfaces. However, most objects we touch in daily tasks have 3D shape and macro curvatures that were not accounted for in our models. Future modeling efforts should aim to fill this gap in order to understand the forces patterns felt while touching 3D objects.

The experiments presented in this dissertation constrained both the sliding speed and normal contact force applied while subjects explored object surfaces. Nevertheless, usual touch interactions with objects occur with variable sliding speeds and normal forces. More sophisticated frictional force models should account explicitly for variations in sliding speed and normal force applied to produce outputs that reflect those variations.

The research presented here has potential applications for human-machine interfaces with touch screen displays which are available in most modern electronic devices such as automotive displays, cell phones or consumer electronics. Enabling a user to feel surface characteristics presented visually in this type of displays would engage the users in more appealing interactions, facilitating interaction with the electronic devices, and in some cases reducing the need for visual input to interact with these displays.

Virtual and augmented reality technologies that include haptic rendering (often in combination with audiovisual rendering) engage the user in more realistic interactions with a virtual environment, in which texture perception plays a major role for the interaction with virtual objects. The models

presented here would enable haptic rendering techniques to present more realistic object touch sensations artificially in the future.

Bibliography

[1] Susan J. Lederman and Roberta L. Klatzky. Extracting object properties through haptic exploration. *Acta psychologica*, 84(1):29–40, 1993.

[2] Michael Wiertlewski, Jose Lozada, and Vincent Hayward. The spatial spectrum of tangential skin displacement can encode tactual texture. *IEEE Transactions on Robotics*, 27(3), 2011.

[3] Gabriel Robles-De-La-Torre and Vincent Hayward. Force can overcome object geometry in the perception of shape through active touch. *Nature*, 412(6845):445–448, 2001.

[4] Stephen E. Palmer. *Vision science: Photons to phenomenology*, volume 1. MIT press Cambridge, MA, 1999.

[5] Stanley Smith Stevens and Hallowell Davis. *Hearing: Its psychology and physiology*. American Institute of Physics for the Acoustical Society of America, 1983.

[6] Roland S. Johansson and J. Randall Flanagan. Coding and use of tactile signals from the fingertips in object manipulation tasks. *Nature Reviews Neuroscience*, 10(5):345–359, 2009.

[7] Gabriel Robles-De-La-Torre. The importance of the sense of touch in virtual and real environments. *IEEE Multimedia*, (3):24–30, 2006.

[8] M. Gail Jones, James Minogue, Tom Oppewal, Michelle P. Cook, and Bethany Broadwell. Visualizing without vision at the microscale: Students with visual impairments explore cells with touch. *Journal of Science Education and Technology*, 15(5-6):345–351, 2006. ISSN 1059-0145. doi: 10.1007/s10956-006-9022-6. URL http://dx.doi.org/10.1007/s10956-006-9022-6.

[9] Roland S. Johansson, Ronald Riso, Charlotte Hger, and Lars Bckstrm. Somatosensory control of precision grip during unpredictable pulling loads. *Experimental Brain Research*, 89(1):181–191, 1992. ISSN 0014-4819. doi: 10.1007/BF00229015. URL http://dx.doi.org/10.1007/BF00229015.

[10] James C. Craig and Gary B. Rollman. Somesthesis. *Annual Review of Psychology*, 50(1):305–331, 1999.

[11] Ronald T. Verrillo. Vibrotactile thresholds for hairy skin. *Journal of Experimental Psychology*, 72(1):47, 1966.

[12] Roland S. Johansson, U. Landstro, R. Lundstro, et al. Responses of mechanoreceptive afferent units in the glabrous skin of the human hand to sinusoidal skin displacements. *Brain Research*, 244(1):17–25, 1982.

[13] David A. Mahns, N. M. Perkins, Vineet Sahai, L. Robinson, and M. J. Rowe. Vibrotactile frequency discrimination in human hairy skin. *Journal of Neurophysiology*, 95(3):1442–1450, 2006. ISSN 0022-3077. doi: 10.1152/jn.00483.2005.

[14] Kenneth O. Johnson. The roles and functions of cutaneous mechanoreceptors. *Current Opinion in Neurobiology*, 11(4):455–461, 2001.

[15] Å. B. Vallbo and R. S. Johansson. Properties of cutaneous mechanoreceptors in the human hand related to touch sensation. *Human Neurobiol*, 3(1):3–14, 1984.

[16] Martin Grunwald. *Human haptic perception: Basics and applications*. Springer Science & Business Media, 2008.

[17] Jonathan Bell, Stanley Bolanowski, and Mark H. Holmes. The structure and function of pacinian corpuscles: A review. *Progress in Neurobiology*, 42(1):79–128, 1994.

[18] Stanley J. Bolanowski Jr, George A. Gescheider, Ronald T. Verrillo, and Christin M. Checkosky. Four channels mediate the mechanical aspects of touch. *The Journal of the Acoustical Society of America*, 84(5):1680–1694, 1988.

[19] Daniel Johnston, Samuel Miao-Sin Wu, and Richard Gray. *Foundations of cellular neurophysiology*. MIT press Cambridge, MA, 1995.

[20] Kenneth O. Johnson and Steven S. Hsiao. Neural mechanisms of tactual form and texture perception. *Annual Review of Neuroscience*, 15(1):227–250, 1992.

[21] Roland S. Johansson and Å. B. Vallbo. Tactile sensibility in the human hand: relative and absolute densities of four types of mechanoreceptive units in glabrous skin. *The Journal of Physiology*, 286(1):283–300, 1979.

[22] Robert H. LaMotte and Mandayam A. Srinivasan. Surface microgeometry: Tactile perception and neural encoding. In *WENNER GREN CENTER INTERNATIONAL SYMPOSIUM SERIES*, pages 49–49. MACMILLAN ACADEMIC AND PROFESSIONAL LTD, 1991.

[23] Sliman J. Bensmaia, Yuk-Yuen Leung, Steven S. Hsiao, and Kenneth O. Johnson. Vibratory adaptation of cutaneous mechanoreceptive afferents. *Journal of Neurophysiology*, 94(5):3023–3036, 2005.

[24] Yuk-Yuen Leung, Sliman J. Bensmaia, S. S. Hsiao, and K. O. Johnson. Time-course of vibratory adaptation and recovery in cutaneous mechanoreceptive afferents. *Journal of Neurophysiology*, 94(5):3037–3045, 2005.

[25] Ronald T Verrillo and Stanley J Bolanowski Jr. The effects of skin temperature on the psychophysical responses to vibration on glabrous and hairy skin. *The Journal of the Acoustical Society of America*, 80(2):528–532, 1986.

[26] Mark Hollins and S. Ryan Risner. Evidence for the duplex theory of tactile texture perception. *Perception & Psychophysics*, 62(4):695–705, 2000.

[27] Mark Hollins, Sliman J. Bensmaia, and Sean Washburn. Vibrotactile adaptation impairs discrimination of fine, but not coarse, textures. *Somatosensory & Motor Research*, 18(4): 253–262, 2001.

[28] David T. Blake, Steven S. Hsiao, and Kenneth O. Johnson. Neural coding mechanisms in tactile pattern recognition: the relative contributions of slowly and rapidly adapting mechanoreceptors to perceived roughness. *The Journal of Neuroscience*, 17(19):7480–7489, 1997.

[29] Kenneth O. Johnson and Steven S. Hsiao. Evaluation of the relative roles of slowly and rapidly adapting afferent fibers in roughness perception. *Canadian Journal of Physiology and Pharmacology*, 72(5):488–497, 1994.

[30] Sliman J. Bensmaia and Mark Hollins. Pacinian representations of fine surface texture. *Perception & Psychophysics*, 67(5):842, 2005.

[31] David Katz. *The world of touch*. Psychology Press, 2013.

[32] Mark Hollins and Sliman J. Bensmaia. The coding of roughness. *Canadian Journal of Experimental Psychology/Revue Canadienne de Psychologie Experimentale*, 61(3):184, 2007.

[33] Mark Hollins, Richard Faldowski, Suman Rao, and Forrest Young. Perceptual dimensions of tactile surface texture: A multidimensional scaling analysis. *Perception & Psychophysics*, 54 (6):697–705, 1993. ISSN 0031-5117. doi: 10.3758/BF03211795. URL `http://dx.doi.org/10.3758/BF03211795`.

[34] Mark Hollins, Sliman Bensmaa, Kristie Karlof, and Forrest Young. Individual differences in perceptual space for tactile textures: Evidence from multidimensional scaling. *Perception & Psychophysics*, 62(8):1534–1544, 2000. ISSN 0031-5117. doi: 10.3758/BF03212154. URL http://dx.doi.org/10.3758/BF03212154.

[35] Arthur S. Schwartz, Alan J. Perey, and Alan Azulay. Further analysis of active and passive touch in pattern discrimination. *Bulletin of the Psychonomic Society*, 6(1):7–9, 1975. ISSN 0090-5054. doi: 10.3758/BF03333128. URL http://dx.doi.org/10.3758/BF03333128.

[36] James J. Gibson. Observations on active touch. *Psychological Review*, 69(6):477, 1962.

[37] Julien van Kuilenburg, Marc A. Masen, and Emile van der Heide. A review of fingerpad contact mechanics and friction and how this affects tactile perception. *Proceedings of the Institution of Mechanical Engineers, Part J: Journal of Engineering Tribology*, 229(3):243–258, 2015.

[38] Susan J. Lederman. The perception of surface roughness by active and passive touch. *Bulletin of the Psychonomic Society*, 18(5):253–255, 1981.

[39] Susan J. Lederman and Martin M. Taylor. Fingertip force, surface geometry, and the perception of roughness by active touch. *Perception & Psychophysics*, 12(5):401–408, 1972.

[40] M. M. Taylor and Susan J. Lederman. Tactile roughness of grooved surfaces: A model and the effect of friction. *Perception & Psychophysics*, 17(1):23–36, 1975.

[41] El Mehdi Meftah, Loïc Belingard, and C. Elaine Chapman. Relative effects of the spatial and temporal characteristics of scanned surfaces on human perception of tactile roughness using passive touch. *Experimental Brain Research*, 132(3):351–361, 2000.

[42] Allan M. Smith, C. Elaine Chapman, Mélanie Deslandes, Jean-Sébastien Langlais, and Marie-Pierre Thibodeau. Role of friction and tangential force variation in the subjective scaling of tactile roughness. *Experimental Brain Research*, 144(2):211–223, 2002.

[43] Alice H. Sullivan. The cutaneous perceptions of softness and hardness. *Journal of Experimental Psychology*, 10(6):447, 1927.

[44] Lope Ben Porquis, Masashi Konyo, and Satoshi Tadokoro. Representation of softness sensation using vibrotactile stimuli under amplitude control. In *2011 IEEE International Conference on Robotics and Automation*, pages 1380–1385. IEEE, 2011.

[45] Antonio Bicchi, Enzo P. Scilingo, and Danilo De Rossi. Haptic discrimination of softness in teleoperation: the role of the contact area spread rate. *IEEE Transactions on Robotics and Automation*, 16(5):496–504, 2000.

[46] Valentin Popov. *Contact mechanics and friction: physical principles and applications*. Springer Science & Business Media, 2010.

[47] Susan J. Lederman and Roberta L. Klatzky. Hand movements: A window into haptic object recognition. *Cognitive psychology*, 19(3):342–368, 1987.

[48] T. Callier, H. P. Saal, E. C. Davis-Berg, and S. J. Bensmaia. Kinematics of unconstrained tactile texture exploration. *Journal of Neurophysiology*, 113(7), 2015. ISSN 0022-3077. doi: 10.1152/jn.00703.2014.

[49] K. Drewing, A. Lezkan, and S. Ludwig. Texture discrimination in active touch: Effects of the extension of the exploration and their exploitation. In *Proc. IEEE World Haptics Conference*, pages 215–220, June 2011. doi: 10.1109/WHC.2011.5945488.

[50] Takashi Yoshioka, James C. Craig, Graham C. Beck, and Steven S. Hsiao. Perceptual constancy of texture roughness in the tactile system. *The Journal of Neuroscience*, 31(48), 2011.

[51] Susan J. Lederman. Tactile roughness of grooved surfaces: The touching process and effects of macro-and microsurface structure. *Perception & Psychophysics*, 16(2), 1974.

[52] Susan J. Lederman. 4. the perception of texture by touch. *Tactual perception: A sourcebook*, page 130, 1982.

[53] Roberta L. Klatzky and Susan J. Lederman. Tactile roughness perception with a rigid link interposed between skin and surface. *Perception and Psychophysics*, 61(4):591–607, 1999.

[54] Roberta L. Klatzky, Susan J. Lederman, Cheryl Hamilton, Molly Grindley, and Robert H. Swendsen. Feeling textures through a probe: Effects of probe and surface geometry and exploratory factors. *Perception & Psychophysics*, 65(4):613–631, 2003.

[55] T. Yoshioka, S. J. Bensmaia, J. C. Craig, and S. S. Hsiao. Texture perception through direct and indirect touch: an analysis of perceptual space for tactile textures in two modes of exploration. *Somatosensory & motor research*, 24(1-2):53–70, 2007.

[56] Mark Hollins, Florian Lorenz, and Daniel Harper. Somatosensory coding of roughness: the effect of texture adaptation in direct and indirect touch. *The Journal of Neuroscience*, 26(20): 5582–5588, 2006.

[57] Sliman J. Bensmaia and Mark Hollins. The vibrations of texture. *Somatosensory & motor research*, 20(1):33–43, 2003.

[58] Joseph M. Romano and Katherine J. Kuchenbecker. Creating realistic virtual textures from contact acceleration data. *IEEE Transactions on Haptics*, 5(2), 2012.

[59] Heather Culbertson, Juliette Unwin, Benjamin E. Goodman, and Katherine J. Kuchenbecker. Generating haptic texture models from unconstrained tool-surface interactions. In *World Haptics Conference (WHC), 2013*, pages 295–300. IEEE, 2013.

[60] Marco Janko, Richard Primerano, and Yon Visell. Scale dependence of force patterns during the scanning of a surface by a bare finger. In *Haptics: Neuroscience, Devices, Modeling, and Applications*, pages 301–308. Springer, 2014.

[61] Michael Wiertlewski, Jose Lozada, Edwige Pissaloux, and Vincent Hayward. Causality inversion in the reproduction of roughness. In *Haptics: Generating and Perceiving Tangible Sensations*. Springer, 2010.

[62] Yohei Fujii, Shogo Okamoto, and Yoji Yamada. Interactive forces caused by scanning wavy surfaces. In *Proc. IEEE Haptics Symposium*, 2014.

[63] M. A. Srinivasan and R. H. LaMotte. Tactual discrimination of softness. *Journal of Neurophysiology*, 73(1):88–101, 1995.

[64] John Z. Wu, Ren G. Dong, S. Rakheja, A. W. Schopper, and W. P. Smutz. A structural fingertip model for simulating of the biomechanics of tactile sensation. *Medical Engineering & Physics*, 26(2):165–175, 2004.

[65] Matt B Wagner, Gregory J Gerling, and Jacob Scanlon. Validation of a 3-d finite element human fingerpad model composed of anatomically accurate tissue layers. In *2008 Symposium on Haptic Interfaces for Virtual Environment and Teleoperator Systems*, pages 101–105. IEEE, 2008.

[66] John Z. Wu, Daniel E. Welcome, Kristine Krajnak, and Ren G. Dong. Finite element analysis of the penetrations of shear and normal vibrations into the soft tissues in a fingertip. *Medical Engineering & Physics*, 29(6):718–727, 2007.

[67] Fei Shao, Tom H. C. Childs, Catherine J. Barnes, and Brian Henson. Finite element simulations of static and sliding contact between a human fingertip and textured surfaces. *Tribology International*, 43(12):2308–2316, 2010.

[68] John Z. Wu, Ren G. Dong, W. P. Smutz, and S. Rakheja. Dynamic interaction between a fingerpad and a flat surface: experiments and analysis. *Medical Engineering & Physics*, 25(5): 397–406, 2003.

[69] Siddarth Kumar, Gang Liu, David W. Schloerb, and Mandayam A. Srinivasan. Viscoelastic characterization of the primate finger pad in vivo by microstep indentation and three-dimensional finite element models for tactile sensation studies. *Journal of Biomechanical Engineering*, 137(6):061002, 2015.

[70] Amanda Sue Birch. Experimental determination of the viscoelastic properties of the human fingerpad. 1998.

[71] Dianne T. V. Pawluk and Robert D. Howe. Dynamic lumped element response of the human fingerpad. *Journal of Biomechanical Engineering*, 121(2):178–183, 1999.

[72] Todd C. Pataky, Mark L. Latash, and Vladimir M. Zatsiorsky. Viscoelastic response of the finger pad to incremental tangential displacements. *Journal of Biomechanics*, 38(7):1441–1449, 2005.

[73] Nobuaki Nakazawa, Ryojun Ikeura, and Hikaru Inooka. Characteristics of human fingertips in the shearing direction. *Biological cybernetics*, 82(3):207–214, 2000.

[74] Uri Dinnar. A note on the theory of deformation in compressed skin tissues. *Mathematical Biosciences*, 8(1):71–82, 1970.

[75] Benoit Delhaye, Philippe Lefèvre, and Jean-Louis Thonnard. Dynamics of fingertip contact during the onset of tangential slip. *Journal of The Royal Society Interface*, 11(100):20140698, 2014.

[76] Michael Wiertlewski and Vincent Hayward. Mechanical behavior of the fingertip in the range of frequencies and displacements relevant to touch. *Journal of Biomechanics*, 45(11):1869–1874, 2012.

[77] Tao Wu, Joel P Felmlee, James F Greenleaf, Stephen J Riederer, and Richard L Ehman. Assessment of thermal tissue ablation with mr elastography. *Magnetic Resonance in Medicine*, 45(1):80–87, 2001.

[78] E Sapin-de Brosses, JL Gennisson, M Pernot, M Fink, and Mickael Tanter. Temperature dependence of the shear modulus of soft tissues assessed by ultrasound. *Physics in medicine and biology*, 55(6):1701, 2010.

[79] Jason C. Cohen, James C. Makous, and Stanley J. Bolanowski. Under which conditions do the skin and probe decouple during sinusoidal vibrations? *Experimental brain research*, 129 (2):211–217, 1999.

[80] Nicholas Xydas and Imin Kao. Modeling of contact mechanics with experimental results for soft fingers. In *Proceedings. 1998 IEEE/RSJ International Conference on Intelligent Robots and Systems. Innovations in Theory, Practice and Applications (Cat. No.98CH36190)*, volume 1, pages 488–493. IEEE, 1998.

[81] H. Hertz. On the contact of rigid elastic solids and on hardness, chapter 6: Assorted papers by h. hertz, 1882.

[82] Nicholas Xydas, Milind Bhagavat, and Imin Kao. Study of soft-finger contact mechanics using finite elements analysis and experiments. In *Proceedings 2000 ICRA. Millennium Conference. IEEE International Conference on Robotics and Automation. Symposia Proceedings (Cat. No.00CH37065)*, volume 3, pages 2179–2184. IEEE, 2000.

[83] Mandayam A. Srinivasan. Surface deflection of primate fingertip under line load. *Journal of Biomechanics*, 22(4):343–349, 1989.

[84] Yohei Fujii, Shogo Okamoto, and Yoji Yamada. Friction model of fingertip sliding over wavy surface for friction-variable tactile feedback panel. *Advanced Robotics*, 30(20):1341–1353, 2016.

[85] Kiran Dandekar, Balasundar I. Raju, and Mandayam A. Srinivasan. 3-d finite-element models of human and monkey fingertips to investigate the mechanics of tactile sense. *Journal of Biomechanical Engineering*, 125(5):682–691, 2003.

[86] Teja Vodlak, Zlatko Vidrih, Dusan Fetih, Djordje Peric, and Tomaz Rodic. Development of a finite element model of a finger pad for biomechanics of human tactile sensations. In *2015 37th Annual International Conference of the IEEE Engineering in Medicine and Biology Society (EMBC)*, pages 909–912. IEEE, 2015.

[87] Behnam Khojasteh, Marco Janko, and Yon Visell. Numerical studies of sliding friction between a finger and a textured surface. In *International Conference on Biotribology*, 2016.

[88] Mitsunori Tada and Dinesh K. Pai. Finger shell: predicting finger pad deformation under line loading. In *Haptic interfaces for virtual environment and teleoperator systems, 2008. haptics 2008. symposium on*, pages 107–112. IEEE, 2008.

[89] Constantine C. Spyrakos. *Finite Element Modeling*. West Virginia Univ. Press, 1994.

[90] Allan M. Smith and Stephen H. Scott. Subjective scaling of smooth surface friction. *Journal of Neurophysiology*, 75(5):1957–1962, 1996.

[91] M. J. Adams, B. J. Briscoe, and S. A. Johnson. Friction and lubrication of human skin. *Tribology Letters*, 26(3):239–253, 2007. ISSN 1023-8883. doi: 10.1007/s11249-007-9206-0. URL http://dx.doi.org/10.1007/s11249-007-9206-0.

[92] C. P. Hendriks and S. E. Franklin. Influence of surface roughness, material and climate conditions on the friction of human skin. *Tribology Letters*, 37(2):361–373, 2010.

[93] NK Veijgen, Marc Arthur Masen, and Emile van der Heide. Relating friction on the human skin to the hydration and temperature of the skin. *Tribology letters*, 49(1):251–262, 2013.

[94] Michael Wiertlewski, Daniele Leonardis, David J. Meyer, Michael A. Peshkin, and J. Edward Colgate. A high-fidelity surface-haptic device for texture rendering on bare finger. In *Eurohaptics 2014*. Springer, 2014.

[95] Thomas H. Massie and J. Kenneth Salisbury. The phantom haptic interface: A device for probing virtual objects. In *Proceedings of the ASME winter annual meeting, symposium on haptic interfaces for virtual environment and teleoperator systems*, volume 55, pages 295–300. Chicago, IL, 1994.

[96] Margaret Minsky, Ouh-young Ming, Oliver Steele, Frederick P. Brooks Jr, and Max Behensky. Feeling and seeing: issues in force display. *ACM SIGGRAPH Computer Graphics*, 24(2): 235–241, 1990.

[97] Olivier Bau, Ivan Poupyrev, Ali Israr, and Chris Harrison. Teslatouch: electrovibration for touch surfaces. In *Proceedings of the 23nd annual ACM symposium on User interface software and technology*, pages 283–292. ACM, 2010.

[98] Vincent Hayward, Oliver R. Astley, Manuel Cruz-Hernandez, Danny Grant, and Gabriel Robles-De-La-Torre. Haptic interfaces and devices. *Sensor Review*, 24(1):16–29, 2004.

[99] Heather Culbertson, Juliette Unwin, and Katherine J. Kuchenbecker. Modeling and rendering realistic textures from unconstrained tool-surface interactions. *IEEE Transactions on Haptics*, 7(3):381–393, 2014.

[100] Margaret Diane Rezvan Minsky. *Computational haptics: the sandpaper system for synthesizing texture for a force-feedback display*. PhD thesis, Massachusetts Institute of Technology, 1995.

[101] Domenico Prattichizzo, Claudio Pacchierotti, and Giulio Rosati. Cutaneous force feedback as a sensory subtraction technique in haptics. *IEEE Transactions on Haptics*, 5(4):289–300.

[102] Christopher R. Wagner, Susan J. Lederman, and Robert D. Howe. A tactile shape display using rc servomotors. In *Haptic Interfaces for Virtual Environment and Teleoperator Systems, 2002. HAPTICS 2002. Proceedings. 10th Symposium on*, pages 354–355. IEEE, 2002.

[103] Gabriel Moy, C. Wagner, and Ronald S. Fearing. A compliant tactile display for teletaction. In *Proceedings 2000 ICRA. Millennium Conference. IEEE International Conference on Robotics and Automation*, volume 4, pages 3409–3415. IEEE, 2000.

[104] Yantao Shen, John Gregory, and Ning Xi. Stimulation current control for load-aware electrotactile haptic rendering: Modeling and simulation. *Robotics and Autonomous Systems*, 62(1): 81–89, 2014.

[105] Kurt Kaczmarek, John G. Webster, Paul Bach-y Rita, Willis J. Tompkins, et al. Electrotactile and vibrotactile displays for sensory substitution systems. *IEEE Transactions on Biomedical Engineering*, 38(1):1–16, 1991.

[106] Eric Vezzoli, Michel Amberg, Frédéric Giraud, and Betty Lemaire-Semail. Electrovibration modeling analysis. In *Haptics: Neuroscience, Devices, Modeling, and Applications*, pages 369–376. Springer, 2014.

[107] Tpad fire: Surface haptic tablet. In *HAID Haptic and Audio Interaction Design*, Daejeon, Korea, 04/2013 2013. Springer, Springer.

[108] Nils Landin, Joseph M. Romano, William McMahan, and Katherine J. Kuchenbecker. Dimensional reduction of high-frequency accelerations for haptic rendering. In *Haptics: Generating and Perceiving Tangible Sensations*, pages 79–86. Springer, 2010.

[109] Alejandro Jarillo Silva, O. Ramirez, Vicente Parra Vega, Jesus P. Ordaz Oliver, et al. Phantom omni haptic device: Kinematic and manipulability. In *Electronics, Robotics and Automotive Mechanics Conference, 2009. CERMA'09.*, pages 193–198. IEEE, 2009.

[110] Seungmoon Choi and Katherine J. Kuchenbecker. Vibrotactile display: Perception, technology, and applications. *Proceedings of the IEEE*, 101(9):2093–2104, 2013.

[111] Kurt A. Kaczmarek, Krishnakant Nammi, Abhishek K. Agarwal, Mitchell E. Tyler, Steven J Haase, and David J. Beebe. Polarity effect in electrovibration for tactile display. *IEEE Transactions on Biomedical Engineering*, 53(10):2047–2054, 2006.

[112] Laura Winfield, John Glassmire, J. Edward Colgate, and Michael Peshkin. T-pad: Tactile pattern display through variable friction reduction. In *Second Joint EuroHaptics Conference and Symposium on Haptic Interfaces for Virtual Environment and Teleoperator Systems (WHC'07)*. IEEE, 2007.

[113] Mélisande Biet, Frédéric Giraud, and Betty Lemaire-Semail. Squeeze film effect for the design of an ultrasonic tactile plate. *IEEE Transactions on Ultrasonics, Ferroelectrics, and Frequency Control*, 54(12):2678–2688, 2007.

[114] Xiaowei Dai, J. Edward Colgate, Michael Peshkin, et al. Lateralpad: A surface-haptic device that produces lateral forces on a bare finger. In *Haptics Symposium (HAPTICS), 2012 IEEE*, pages 7–14. IEEE, 2012.

[115] Ming C. Lin and Miguel Otaduy. *Haptic rendering: foundations, algorithms, and applications*. CRC Press, 2008.

[116] Juhani Siira and Dinesh K. Pai. Haptic texturing-a stochastic approach. In *Proceedings of IEEE International Conference on Robotics and Automation*, volume 1. IEEE, 1996.

[117] Jason P. Fritz and Kenneth E. Barner. Stochastic models for haptic texture. In *Photonics East'96*, pages 34–44. International Society for Optics and Photonics, 1996.

[118] A. M. Okamura, K. J. Kuchenbecker, and M. Mahvash. Measurement-based modeling for haptic display. In M. C. Lin and M. Otaduy, editors, *Haptic Rendering: Foundations, Algorithms, and Applications*, pages 443–467. AK Peters, 2008.

[119] S. E. Tomlinson, R. Lewis, and M. J. Carré. Review of the frictional properties of finger-object contact when gripping. *Proceedings of the Institution of Mechanical Engineers, Part J: Journal of Engineering Tribology*, 221(8):841–850, 2007.

[120] S. Derler and L. C. Gerhardt. Tribology of skin: review and analysis of experimental results for the friction coefficient of human skin. *Tribology Letters*, 45(1):1–27, 2012.

[121] Julien van Kuilenburg. *A Mechanistic Approach to Tactile Friction*. PhD thesis, Citeseer, 2013.

[122] Michael Wiertlewski. *Reproduction of Tactual Textures: Transducers, Mechanics, and Signal Encoding*. PhD thesis, Université de Rouen, 2012.

[123] Michael Wiertlewski, Satoshi Endo, Alan M. Wing, and Vincent Hayward. Slip-induced vibration influences the grip reflex: A pilot study. In *2013 IEEE World Haptics Conference (WHC)*, pages 627–632. IEEE, 2013.

[124] Jonathan Platkiewicz, Alessandro Mansutti, Monica Bordegoni, and Vincent Hayward. Recording device for natural haptic textures felt with the bare fingertip. In *International Conference on Human Haptic Sensing and Touch Enabled Computer Applications*, pages 521–528. Springer, 2014.

[125] Serena Bochereau, Brygida Dzidek, Mike Adams, and Vincent Hayward. Characterizing and imaging gross and real finger contacts under dynamic loading. *IEEE Transactions on Haptics*, 2017.

[126] Serena Bochereau, Stephen Sinclair, and Vincent Hayward. Looking for physical invariants in the mechanical response of a tactually scanned braille dot. In *2015 IEEE World Haptics Conference (WHC)*, pages 119–124. IEEE, 2015.

[127] Nicolae Lobontiu. *Compliant mechanisms: design of flexure hinges*. CRC press, 2002.

[128] J. A. C. Martins, J. T. Oden, and F. M. F. Simes. A study of static and kinetic friction. *Int J Engineering Science*, 28(1), 1990. ISSN 0020-7225. doi: http://dx.doi.org/10.1016/0020-7225(90)90014-A. URL `http://www.sciencedirect.com/science/article/pii/002072259090014A`.

[129] Bo N. J. Persson, O. Albohr, F. Mancosu, V. Peveri, V. N. Samoilov, and Ion Marius Sivebæk. On the nature of the static friction, kinetic friction and creep. *Wear*, 254(9), 2003.

[130] O. M. Braun. Stick-slip vs. smooth sliding in the multicontact interface. *EPL (Europhysics Letters)*, 109(4), 2015. URL `http://stacks.iop.org/0295-5075/109/i=4/a=48004`.

[131] E. G. Learned-Miller. Data driven image models through continuous joint alignment. *IEEE Transactions on Pattern Analysis and Machine Intelligence*, 28(2), Feb 2006. ISSN 0162-8828. doi: 10.1109/TPAMI.2006.34.

[132] Karl Pearson. Note on regression and inheritance in the case of two parents. *Proceedings of the Royal Society of London*, 58:240–242, 1895.

[133] Gary B. Huang, Vidit Jain, and Erik Learned-Miller. Unsupervised joint alignment of complex images. In *2007 IEEE 11th International Conference on Computer Vision*. IEEE, 2007.

[134] F. Al-Bender and J. Swevers. Characterization of friction force dynamics. *Control Systems, IEEE*, 28(6):64–81, Dec 2008. ISSN 1066-033X. doi: 10.1109/MCS.2008.929279.

[135] Gianni Campion and Vincent Hayward. Fast calibration of haptic texture synthesis algorithms. *IEEE Transactions on Haptics*, 2(2), 2009.

[136] Vincent Levesque and Vincent Hayward. Experimental evidence of lateral skin strain during tactile exploration. In *Proceedings of EUROHAPTICS*, volume 2003, 2003.

[137] Gabriel Robles-De-La-Torre and Vincent Hayward. Virtual surfaces and haptic shape perception. In *Proceedings ASME IMECE Symposium on Haptic Interfaces for Virtual Environments and Teleoperator Systems*, volume 69, page 2, 2000.

[138] R. C. Gonzalez, Richard E. Woods, and Steven L. Eddins. Processing, 1987.

[139] Marco Janko, Richard Primerano, and Yon Visell. On frictional forces between the finger and a textured surface during active touch. *IEEE Transactions on Haptics*, 9(2):221–232, April 2016. ISSN 1939-1412. doi: 10.1109/TOH.2015.2507583.

[140] Vincent Hayward and Dingrong Yi. Change of height: An approach to the haptic display of shape and texture without surface normal. *Experimental Robotics VIII*, pages 570–579, 2003.

[141] Maarten WA Wijntjes, Akihiro Sato, Vincent Hayward, and Astrid ML Kappers. Local surface orientation dominates haptic curvature discrimination. *IEEE transactions on haptics*, 2(2): 94–102, 2009.

[142] Jeffrey C. Lagarias, James A. Reeds, Margaret H. Wright, and Paul E. Wright. Convergence properties of the nelder–mead simplex method in low dimensions. *SIAM Journal on optimization*, 9(1):112–147, 1998.

[143] Graham D Lamb. Tactile discrimination of textured surfaces: psychophysical performance measurements in humans. *The Journal of Physiology*, 338(1):551–565, 1983.